



# LUND UNIVERSITY

## Continuum modeling of paperboard for the mechanical response of converting processes

Robertsson, Kristofer

2023

*Document Version:*

Publisher's PDF, also known as Version of record

[Link to publication](#)

*Citation for published version (APA):*

Robertsson, K. (2023). *Continuum modeling of paperboard for the mechanical response of converting processes*. Division of solid mechanics, Lund University.

*Total number of authors:*

1

### General rights

Unless other specific re-use rights are stated the following general rights apply:

Copyright and moral rights for the publications made accessible in the public portal are retained by the authors and/or other copyright owners and it is a condition of accessing publications that users recognise and abide by the legal requirements associated with these rights.

- Users may download and print one copy of any publication from the public portal for the purpose of private study or research.
- You may not further distribute the material or use it for any profit-making activity or commercial gain
- You may freely distribute the URL identifying the publication in the public portal

Read more about Creative commons licenses: <https://creativecommons.org/licenses/>

### Take down policy

If you believe that this document breaches copyright please contact us providing details, and we will remove access to the work immediately and investigate your claim.

LUND UNIVERSITY

PO Box 117  
221 00 Lund  
+46 46-222 00 00



**LUNDS**  
UNIVERSITET

**CONTINUUM MODELING OF  
PAPERBOARD FOR THE MECHANICAL  
RESPONSE OF CONVERTING PROCESSES**

KRISTOFER ROBERTSSON

---

Solid  
Mechanics

*Doctoral Thesis*

---



*Department of Construction Sciences*  
Solid Mechanics

ISRN LUTFD2/TFHF-23/1066-SE (1-138)  
ISBN: 978-91-8039-655-4 (print)  
ISBN: 978-91-8039-656-1 (pdf)

# Continuum modeling of paperboard for the mechanical response of converting processes

Doctoral Thesis by

Kristofer Robertsson

Copyright © 2023 by Kristofer Robertsson

Printed by Media-Tryck AB, Lund, Sweden

For information, address:

Division of Solid Mechanics, Lund University, Box 118, SE-221 00 Lund, Sweden

Homepage: <http://www.solid.lth.se>



*Till Per & Pia*



## Preface

This thesis is the result of my doctoral studies at the Division of Solid Mechanics, Lund University, financially supported by Tetra Pak and BioInnovation, a joint collaboration between Vinnova, Formas and the Swedish Energy Agency. First of all, I would like to express my gratitude to my main supervisor, Prof. Mathias Wallin, who, with his inspiring work ethic, has provided me with persistent help during my studies. I would also like to thank my co-supervisors, Prof. Matti Ristinmaa, Dr. Eric Borgqvist, and Dr. Jonas Engqvist. It has been a privilege to have such a knowledgeable and supportive team behind me. In addition, special thanks to Adj. Prof. Johan Tryding, who has been a supervisor of mine in all but name. To all my current and former colleagues at the department, thank you for providing such a pleasant and open working environment. It has been a genuine pleasure to work alongside all of you, and hopefully I will get the opportunity to collaborate with some of you in the future. Apart from work, thanks to my friends in Malmö who have provided me with much-needed distractions during my studies. Finally, I thank my lovely parents for their unconditional love and support.

Lund, March 2023

Kristofer Robertsson



## Abstract

Paperboard is a thin and lightweight material made of cellulose fibers and it is an important component in packaging material where it provides stiffness and rigidity. The scope of this work is the development of continuum models, and their numerical treatment, for simulating the processes of converting paperboard into packages. The thesis begins with a general introduction to paperboard and a review of modeling approaches are presented. Important continuum modeling concepts used in the papers are presented and key paperboard converting processes are discussed. The main part of the thesis consists of four papers denoted A, B, C and D and they are briefly outlined below.

To reduce the computational effort during large-scale paperboard forming simulations, a numerical technique which combines a state-of-the-art continuum model for paperboard with state-of-the-art finite element modeling is investigated in Paper A. The model is built up by solid-shell elements where the thickness direction is naturally included in the framework such that the out-of-plane response can be modeled. The approach is validated by numerical studies where the results are compared against fully integrated brick elements. Furthermore, a large-scale forming example for paperboard is explored.

Since the loading rate varies during industrial processes and the aim is to maximize the operational velocity, a rate-dependent continuum model for paperboard is developed in Paper B. The new rate-dependent model is based on the static material model in Paper A which is enhanced with a viscoelastic and viscoplastic framework. The developed model is calibrated using uniaxial experiments and evaluated against line-creasing and line-folding measurements.

In Paper C, the continuum model in Paper A is enhanced to include continuum damage. Damage is needed to adequately capture the mechanical response during sequential loading of creasing and folding. A scalar isotropic damage variable is introduced and the damage evolution is calibrated for a reference mesh during folding. A simple scaling strategy is introduced to reduce the mesh dependence due to damage evolution. To showcase the proposed model, an illustrative 3D example is presented where a paperboard sheet is creased and folded to mimic the corner folding process.

In Paper D, an experimental device and a protocol is developed for cyclic uniaxial out-of-plane compression and tension measurements. This load case is important since it is present during creasing and subsequent folding where the material is subject to large out-of-plane compressive stresses followed by out-of-plane tension and delamination. The soft initial load-displacement response during compression is shown to stem from the surface roughness and not a material property. In addition, the experiments show that the transition from compression to tension is smooth. Consequently, a switch function, previously used in literature that separates the elastic behavior between compression and tension, is deemed as questionable for continuum modeling.



## Populärvetenskaplig sammanfattning

Kartong är ett fiberbaserat pappersmaterial och den huvudsakliga komponenten i förpackningsmaterial som ofta används för konsumentpaketering av bland annat juice och mjölkprodukter. Den höga böjstyvheten i förhållande till materialets densitet samt dess formbarhet gör kartong till en lämplig komponent i förpackningsmaterialet. Stora mängder kartong produceras årligen då dess gynnsamma egenskaper kombineras med en låg produktionskostnad samt låg miljöpåverkan på grund av sitt naturliga ursprung.

I detta projekt har matematiska simuleringsmodeller för kartong vidareutvecklats genom att inkludera nya fysikaliska aspekter. Virtuellt modellering och simulering kan minska kostnaderna vid utvecklingen av nya produkter då färre fysikaliska tester krävs i produktionsutvecklingscykeln. Simuleringsverktyg kan även bidra med insikt i komplexa konverteringsprocesser där experimentella metoder antingen saknas eller kräver för stora resurser.

En karakteristisk kartongaspekt är den stora skillnaden i mekaniska egenskaper mellan kartongens tjockleksriktning och den riktning längst med arket som fibrerna föredrar att orienteras. Denna egenskap kallas anisotropi och är en konsekvens av tillverkningsprocessen för kartong. Den stora graden av anisotropi är en av anledningarna till att kartong är ett utmanande material att modellera.

Denna avhandling studerar primärt bigning och vikning. Bigning är en process där materialet medvetet skadas mekaniskt längst med förutbestämda vikningslinjer vilket underlättar efterföljande vikning då kartongen formas till en förpackning. Bigning och vikning involverar delaminering i tjockleksriktning då fiberbindningarna släpper vilket leder till mycket komplexa förlopp även under de mest ideala förhållande.

Avhandlingen består huvudsakligen av fyra artiklar benämnda A,B,C och D. I artikel A kombineras en avancerad kartongmodell med en numerisk simuleringsteknik för att effektivt kunna utföra storskaliga simuleringar. Kartongmodellen i artikel A vidareutvecklas i artikel B för att inkludera hastighetsberoende effekter. Detta är viktigt eftersom processhastigheten för industriell konvertering tenderar att öka samt att töjningshastigheten varierar i kartongmaterialet under dessa processer. I artikel C vidareutvecklas modellen i artikel A genom att inkludera skadmodellering vilket gör det möjligt att fånga vikningsförloppet efter bigning.

En experimentell uppställning för cyklisk belastning mellan tryck och drag i kartongens tjockleksriktning har utvecklats och analyserats i artikel D. Detta är ett relevant lastfall som uppkommer under bigning och viknings processen men har tidigare inte studerats.



## List of appended papers

This doctoral thesis is based on the following manuscripts:

### Paper A

Kristofer Robertsson, Eric Borgqvist, Mathias Wallin, Matti Ristinmaa, Johan Tryding, Andrea Giampieri and Umerto Perego  
*Efficient and accurate simulation of the packaging forming process*  
Packag Technol Sci. 31 (2018), 557-566

### Paper B

Kristofer Robertsson, Mathias Wallin, Eric Borgqvist, Matti Ristinmaa and Johan Tryding  
*A rate-dependent continuum model for rapid converting of paperboard*  
Applied Mathematical Modelling 99 (2021), 497-513

### Paper C

Kristofer Robertsson, Erik Jacobsson, Mathias Wallin, Eric Borgqvist, Matti Ristinmaa and Johan Tryding  
*A continuum damage model for creasing and folding of paperboard*  
Submitted for publication

### Paper D

Kristofer Robertsson, Jonas Engqvist, Mathias Wallin, Matti Ristinmaa, Johan Tryding and Eric Borgqvist  
*Out-of-plane uniaxial loading of paperboard: experimental procedure and evaluation*  
Submitted for publication

### Own Contribution

The author of this thesis has taken the main responsibility for the preparation and writing of all papers. The numerical implementation in Paper A has been developed in collaboration with the coauthors. The models in Paper B and C has been developed in collaboration with the coauthors and implemented by the main author. The apparatus presented in Paper D has been developed in collaboration with the second author. In Paper A, B, C and D, all simulations and analysis of data have been performed by the main author.



# Contents

<b>1</b>	<b>Introduction</b>	<b>I</b>
<b>2</b>	<b>The paperboard material</b>	<b>2</b>
<b>3</b>	<b>Modeling methods for paper-based materials</b>	<b>5</b>
<b>4</b>	<b>Continuum modeling of paperboard</b>	<b>6</b>
	4.1 Modeling background	6
	4.2 Extension to viscoelasticity	8
	4.3 Plasticity and viscoplasticity	9
	4.4 Damage model	10
	4.5 Implementation and numerical considerations	11
<b>5</b>	<b>Computational modeling of converting processes</b>	<b>14</b>
<b>6</b>	<b>Future work</b>	<b>21</b>
<b>7</b>	<b>Summary of the appended papers</b>	<b>22</b>
	References	23
	Paper A	
	Paper B	
	Paper C	
	Paper D	



# I Introduction

Fibrous materials made of natural components such as cellulose, for instance paperboard, exhibits a number of challenging characteristics. Paperboard is a thin anisotropic material where the degree of anisotropy is particularly pronounced between the stacking direction of fibers, i.e. the thin out-of-plane direction, and the preferred fiber orientation in the in-plane sheet direction. Apart from the large degree of anisotropy, paperboard is sensitive to moisture, temperature and the rate of which the material is deformed. In addition, during many converting processes, paperboard is subject to large out-of-plane deformations which eventually leads to delamination.

Computational paperboard modeling can be performed at various scales which can provide different types of insights. Models that aims to represent the physical behavior of individual fibers, often denoted network models, can be used to guide the paper-making process and provide understanding of the underlying physical behavior but has limited use when considering full packages. Another approach is to model a representative volume element (RVE) of the material which is the smallest volume where measurements will represent the response obtained from a large sample. This assumption is fundamental for continuum modeling which often is used for simulating large-scale industrial converting applications. Computational modeling with this approach offers several benefits when analyzing complex industrial processes since the alternatives, such as adopting a trial and error approach or performing sophisticated experiments, are costly and challenging.

The application of interest in this thesis is the converting of paperboard into a package. The process consists of two main procedures, creasing and folding. During creasing, permanent deformation is induced along predefined lines to reduce the bending stiffness in order to guide subsequent folding. The folding procedure is the last phase in the converting process when the sheet is transformed to a final package shape. Since both creasing and folding are performed at package level, the continuum approach is used in this thesis.

## 2 The paperboard material

One of the main applications for paperboard is as a component in packaging material which is a sandwich structure used for food and beverage packaging. The multi-layered packaging material consists of paperboard, aluminum and thin layers of polymers such as polyethylene. In this composite, paperboard has the largest volume fraction and contributes the most to its rigidity and stiffness. The aluminum layer provides light and oxygen resistance while the polymer films acts as barriers between the paperboard and the environment. Fig. 1 shows a schematic image of a packaging material.

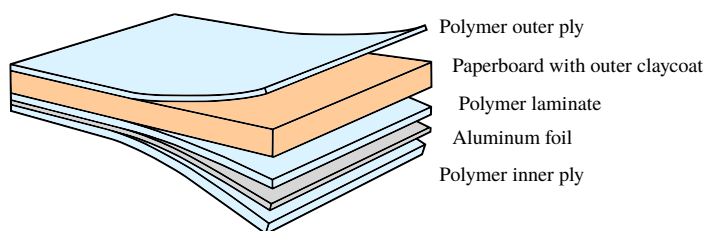


Figure 1: Paperboard as a component in packaging material.

Paperboard is a fiber-composite material with a thickness ranging between 0.2 – 0.5 mm and a density around 300 – 900 kg/m<sup>3</sup>. The main ingredient is fibers that are typically made of either softwood or hardwood with a representative length of 3.6 mm and 1.2 mm, respectively, see Rutilainen et al. (1998). To improve the bending performance, paperboard is often manufactured as a sandwiched structure with several plies where the middle ply has a low density compared to the stiff outer layers. In addition, the low density middle region is advantageous since it is prone to delamination which is beneficial during folding. Furthermore, to improve the printing quality, the outside paperboard layer is often claycoated. In the current work, a single ply paperboard is used for simplicity.

The anisotropy of paperboard stems from the manufacturing process where sheets are produced using a web-nostril that continuously applies fibers in a preferred direction on a conveyor belt. The manufacturing direction, i.e. machine direction, is abbreviated as MD and together with its perpendicular direction, denoted the cross direction CD, they span the in-plane sheet dimension. The third characteristic direction of paperboard is the thin out-of-plane stacking direction of fibers, denoted as the ZD direction. The degree of anisotropy is largest between the preferred fiber orientation MD and the weak out-of-plane ZD direction where the elastic modulus along the MD direction can be 100 times the magnitude of ZD.

The mechanical properties of paperboard are highly sensitive to water and humidity. This type of interaction is undoubtedly complex due to its rich physics. For instance, cellulose fibers are hygroscopic and readily absorb water that results in fiber swelling. In addition, the fiber network contains hydrogen bonds that are intrinsically sensitive to moisture and can break due to the interaction, see Alava and Niskanen (2006). In general, paperboard becomes weaker with increased moisture ratio. For example, the in-plane tensile strength along MD in Marin et al. (2020) approximately decreases by a factor of 2.5 when the moisture ratio is increased by a factor of 3. Although the impact of

moisture is significant, it is beyond the scope of this thesis since the developed continuum models are primarily concerned with the mechanical behavior of converting operations performed in stationary controlled environment.

Uniaxial mechanical experiments are often used to calibrate continuum models. For paperboard, the most reliable experiments are uniaxial in-plane tension measurements as shown in Fig. 2 where tension was performed for three strain rates along the MD, CD and 45° direction between the two.

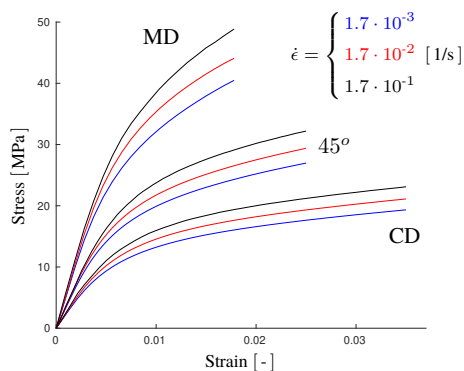


Figure 2: Uniaxial tension, different directions and strain rates. Figure is reproduced from Paper B.

In contrast to the Fig. 2 measurements, most other uniaxial experiments that aim to activate a single stress component are challenging since paperboard is thin. For example, to measure the in-plane compression response, either the long-edge or the short-span compression test can be used, see Borgqvist et al. (2016). The long-edge test consists of a 55 mm long specimen while the short-span compression test utilizes a short length of 0.7 mm to avoid buckling. In the long-edge compression test, the elastic modulus is similar to the one obtained in tension, however, the failure stress is underestimated due to buckling instability. In an attempt to lower the effect of buckling a number of stabilizing rods are often used. For the short-span compression test, the failure stress is larger compared to the long-edge compression test but the elastic modulus is not the same as in tension. This stems from the influence of the clamping boundary conditions which increases as the sample length is shortened. A schematic illustration of the short-span and long-edge compression test is shown in Fig. 3.

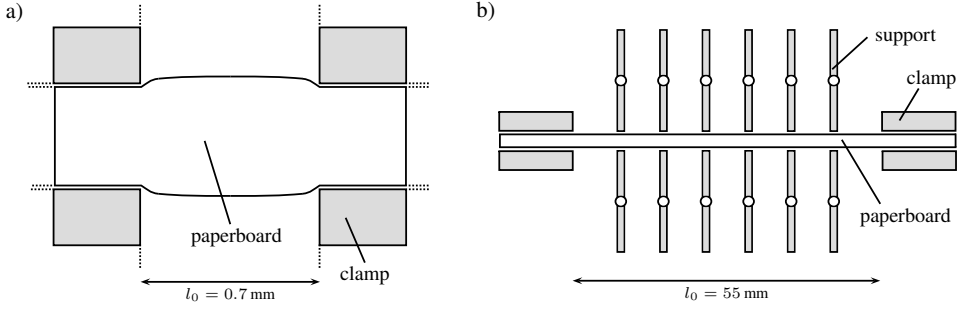


Figure 3: Schematics of the a) short-span and b) long-edge compression tests.

Uniaxial out-of-plane experiments are challenging since its not possible to grip the thin specimen and hence the paperboard sample needs to be attached to the apparatus by use of glue. The need for a precise experimental setup, and the use of glue, results in an inherent degree of uncertainty which is especially pronounced for out-of-plane shearing. Furthermore, during out-of-plane compression a precise experimental setup is also needed due to paperboard being thin. In paper D, a new experimental device and procedure is developed for cyclic loading in out-of-plane compression and tension. It is shown that the surface roughness of paperboard has a large impact on the soft initial response during out-of-plane compression.

In Paper B, a rate-dependent paperboard continuum model is developed where the viscosity is calibrated against uniaxial in-plane experiments for different strain rates together with creep and relaxation tests. The in-plane rate-dependent paperboard response is shown in Fig. 2 for different strain rates while a number of tensile CD creep tests are shown in Fig. 4.

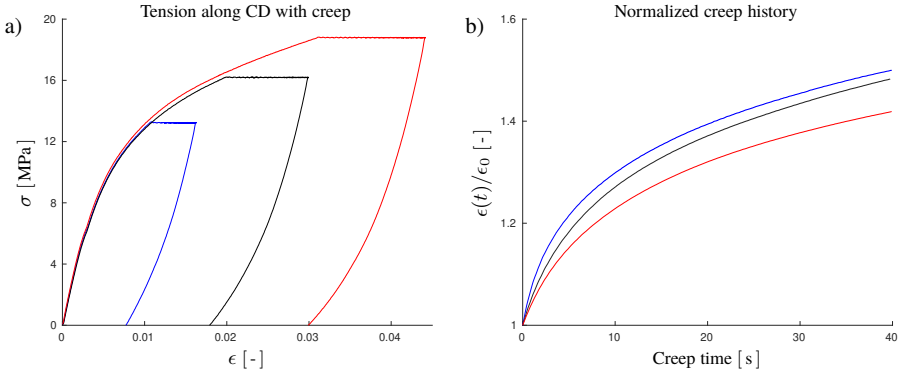


Figure 4: Creep tests for uniaxial tension along CD. Displacement controlled initial phase with strain rate  $\dot{\epsilon} = 0.0017 [1/s]$ . The strain at the start of the creep phase is  $\epsilon_0$ . Figure is reproduced from Paper B.

In Fig. 4, approximately the same creep history is recorded for different stress levels when the strain is normalized against the initial strain level,  $\epsilon_0$ , at the start of the creep phase. Similar observations

are made for uniaxial in-plane relaxation test in Paper B, hence, a single creep and relaxation test can be used to estimate the response over a range of stress and strain levels.

### 3 Modeling methods for paper-based materials

Paperboard models can be based on information at different length scales. Typically models either focus on the network scale such that individual fibers are considered or the sheet scale where the material is modeled as a continuum.

Fiber network models can be represented in different ways, for instance using beam element, cf. Heyden (2000), Kulachenko and Uesaka (2012), where plane stress is assumed. Another method is to discretize the fiber geometry using full 3D continuum elements, cf. Lavrykov et al. (2012), such that the transverse behavior of fibers are more accurately described, however, at the cost of computational efficiency. While the aforementioned models are implemented in a finite element framework, an alternative approach is to use the discrete element method where each end of the fiber and its bonding locations are discretized as particles, e.g. Persson and Isaksson (2014). Apart from the mechanical properties of a fiber, the network response depends on the fiber bonding properties and the fiber distribution in the network. The bonding between fibers can be modeled with different degrees of complexity, for instance, using elastic springs as in Heyden (2000), with use of contact formulations as in Kulachenko and Uesaka (2012) or accounting for the debonding phenomena using cohesive elements as in Borodulina et al. (2018).

A drawback of the network approach is the uncertainty of the required model parameters. While it is possible to make estimates from single fiber and fiber-cross tests, experiments at this scale are fundamentally challenging. Open questions at network level includes, how to gain information about the transversal characteristics of a fiber and how to estimate the fracture energies from fiber-cross experiments, Simon (2020). Network models can be useful for guiding the paper-making process, however, they have limited potential to model large-scale problems since the computational cost is too high. For larger scale applications, e.g. converting operations involving paperboard, another modeling strategy is needed such as continuum modeling.

To model the mechanical behavior at sheet level, the continuum modeling approach has been utilized extensively in the literature. Since the material is thin, a number of in-plane continuum paperboard models, cf. Mäkelä and Östlund (2003), Borgqvist et al. (2014), Li et al. (2016), Pfeiffer and Kolling (2019), has been developed. Although paperboard is thin, several applications, for instance converting operations, involve significant out-of-plane deformation and in those cases in-plane models will not suffice.

To model the general paperboard response, the out-of-plane material behavior is often considered to be decoupled from the in-plane response. This assumption stems from Stenberg and Fellers (2002) where the Poisson's ratio between the in-plane and out-of-plane response is initially close to zero. A small strain estimate can be assumed for the in-plane response while the out-of-plane response is often associated with large strains, especially when delamination occurs. In view of this, one way to model paperboard is to combine a simple in-plane constitutive model with a cohesive interface model which accounts for the out-of-plane behavior. This approach was adopted in, e.g. Huang and Nygård's (2010), Huang et al. (2014) and Beex and Peerlings (2009), Beex and Peerlings (2012).

While interface elements are convenient from a modeling perspective, this approach has a number of drawbacks. For instance, the number of interface elements is arbitrary and the delamination surfaces must be pre-specified. In addition, it can be hard to handle for large problems and numerically inefficient if interface elements are placed between each element in the mesh.

An alternative to the interface approach is to use a more complex constitutive framework which includes the out-of-plane behavior. Such constitutive models need to capture both the large out-of-plane strains and the large degree of anisotropy between the in-plane and out-of-plane response. Since the conventional Hill criteria does not permit such large degrees of anisotropy, cf. Ottosen and Ristinmaa (2005), a more flexible yield surface is required. Such flexible yield surface was introduced in Xia et al. (2002) wherein the anisotropy is captured by several subsurfaces which can harden independently of each other. The Xia yield surface, with different modifications, has been used extensively to model paper-based materials, cf. Borgqvist et al. (2014), Borgqvist et al. (2015), Tjahjanto et al. (2015), Li et al. (2016), Li et al. (2018), Pfeiffer and Kolling (2019). Alternatively, Bedzra et al. (2019) used a multi-surface plasticity model similar to crystal plasticity and compared it to the Xia criteria. They concluded that these models perform similar for in-plane loading. Finally, in Harrysson and Ristinmaa (2008), a Tsai-Wu based criteria was used to model the plastic behavior of corrugated board. In addition to plasticity, large deformation is often required in this approach which increases the complexity. Three-dimensional constitutive models, that are thermodynamically consistent and takes large out-of-plane strains into account, includes Borgqvist et al. (2015), Li et al. (2018), Harrysson and Ristinmaa (2008). This thesis extends the capabilities of the constitutive model developed in Borgqvist et al. (2015) and Borgqvist et al. (2016).

## 4 Continuum modeling of paperboard

In this work, the continuum assumption is used to model the general 3D mechanical response of paperboard with a single constitutive model. As a consequence, the model is based on large deformations as this is of great importance for several applications.

### 4.1 Modeling background

The paperboard model developed in Borgqvist et al. (2015) and Borgqvist et al. (2016) is used in Paper A and further developed in Paper B and C. Some key features of this model is outlined in what follows.

In large strain kinematics, the deformation gradient  $\mathbf{F}$  maps an infinitesimal line segment  $d\mathbf{X}$  from the undeformed material configuration to the spatially deformed  $d\mathbf{x}$ . Similarly to many large strain elastoplastic continuum models, the deformation gradient is separated using a multiplicative split,

$$\mathbf{F} = \mathbf{F}^e \mathbf{F}^p,$$

where  $\mathbf{F}^e$  and  $\mathbf{F}^p$  are the elastic and plastic part of the deformation gradient, respectively. The multiplicative split defines the three configurations as shown in Fig. 5.

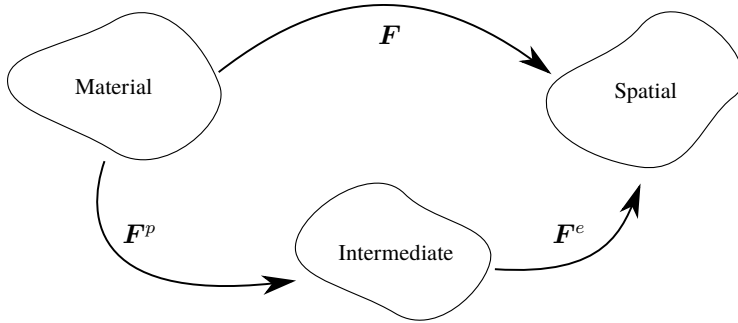


Figure 5: Configurations defined by the multiplicative split,  $\mathbf{F} = \mathbf{F}^e \mathbf{F}^p$ .

The intermediate configuration in Fig. 5 is not unique since an infinite number of equivalent states exists for an orthogonal rotation  $\mathbf{Q}$ . For simplicity, the isoclinic state  $\mathbf{Q} = \mathbf{I}$  is chosen throughout this work, cf. Mandel (1971).

To formulate the constitutive model, the dissipation inequality, which is obtained by combining the first and second law of thermodynamics, is used. The thermodynamical foundation simplifies the inclusion of several physical phenomena such as temperature and moisture dependence, cf. Askfelt (2016), Alexandersson (2020). The current work is restricted to isothermal conditions where the dissipation in the spatial configuration reads

$$\mathcal{D} = \boldsymbol{\tau} : \mathbf{d} - \dot{\Psi} \geq 0 \quad (1)$$

with  $\boldsymbol{\tau}$  being the Kirchhoff stress,  $\mathbf{d}$  is the symmetric part of the spatial velocity gradient and  $\Psi$  is the Helmholtz free energy. The mapping of the characteristic paperboard directions are defined as,

$$\mathbf{v}^{(1)} = \mathbf{F}^e \mathbf{v}_0^{(1)}, \quad \mathbf{v}^{(2)} = \mathbf{F}^e \mathbf{v}_0^{(2)} \quad \text{and} \quad \mathbf{v}^{(3)} = \mathbf{v}^{(1)} \times \mathbf{v}^{(2)} = \det(\mathbf{F}^e) \mathbf{F}^{eT} \mathbf{v}_0^{(3)} \quad (2)$$

with  $\mathbf{v}^{(1)}$ ,  $\mathbf{v}^{(2)}$  and  $\mathbf{v}^{(3)}$  being the current MD, CD and ZD direction, respectively, while  $\mathbf{v}_0^{(1)}$ ,  $\mathbf{v}_0^{(2)}$  and  $\mathbf{v}_0^{(3)}$  are the corresponding initial directions. As seen in (2), the in-plane directions are assumed to follow the elastic part of the deformation while the out-of-plane ZD direction is assumed to remain perpendicular to MD and CD. With this choice, an out-of-plane shear deformation preserves the orientation of the ZD direction which mimics the behavior of the plies in a paperboard composite, Borgqvist et al. (2015).

To derive the elastic constitutive model, the elastic part of the Helmholtz free energy needs to be postulated. Since the model should be coordinate invariant, the energy is constructed using invariants which depends on state variables that characterize the current configuration. The state variables used in the model is the elastic finger tensor  $\mathbf{b}^e = \mathbf{F}^e \mathbf{F}^{eT}$  and three structural tensors  $\mathbf{m}^{(i)}$  that accounts for anisotropy. The structural tensors are defined from the vectors in (2) as,

$$\mathbf{m}^{(1)} = \mathbf{v}^{(1)} \otimes \mathbf{v}^{(1)}, \quad \mathbf{m}^{(2)} = \mathbf{v}^{(2)} \otimes \mathbf{v}^{(2)} \quad \text{and} \quad \mathbf{m}^{(3)} = \mathbf{v}^{(3)} \otimes \mathbf{v}^{(3)}.$$

Since the initial Poisson's ratio between the in-plane and out-of-plane direction is experimentally close to zero, the elastic energy is assumed to be additively separable such that,

$$\Psi^e = \Psi_{ip}^e(\mathbf{b}^e, \mathbf{m}^{(i)}) + \Psi_{oop}^e(\mathbf{b}^e, \mathbf{m}^{(i)}) \quad (3)$$

where  $\Psi_{ip}^e$  and  $\Psi_{oop}^e$  is the elastic energy from the in-plane and out-of-plane modes of deformation, respectively. Insertion of the energy in the dissipation inequality together with thermodynamical arguments, cf. Coleman and Gurtin (1967), the Kirchhoff stress  $\boldsymbol{\tau}$  can be expressed in terms of the elastic deformation gradient  $\mathbf{F}^e$ .

## 4.2 Extension to viscoelasticity

In Paper B, the Borgqvist et al. (2016) model is extended to include viscoelasticity. For this endeavor, the dissipation inequality in the material configuration, cf. Fig 5, is used,

$$\mathcal{D} = \frac{1}{2} \mathbf{S} : \dot{\mathbf{C}} - \dot{\Psi} \geq 0,$$

with  $\mathbf{S}$  being the second Piola-Kirchhoff stress and  $\mathbf{C} = \mathbf{F}^T \mathbf{F}$  is the right Cauchy-Green deformation tensor. The elastic state variables are the elastic deformation tensor  $\mathbf{C}^e$  and the corresponding structural tensors defined as,

$$\mathbf{M}_0^{(i)} = \mathbf{v}_0^{(i)} \otimes \mathbf{v}_0^{(i)} \quad \text{with} \quad i = 1, 2, 3 \quad .$$

Viscoelasticity is modeled by the free energy

$$\Psi^e = \Psi_{oop}^e \left( \mathbf{C}^e, \mathbf{M}_0^{(i)} \right) + \Psi_{ip}^e \left( \mathbf{C}^e, \mathbf{M}_0^{(i)} \right) + \sum_{\alpha} \Upsilon_{\alpha} \left( \mathbf{C}^e, \mathbf{M}_0^{(i)}, \Gamma_{\alpha} \right)$$

where  $\sum \Upsilon_{\alpha}$  is the configurational energy in which each  $\Upsilon_{\alpha}$  is associated with a rheological network  $\alpha$  and a corresponding second order state tensor  $\Gamma_{\alpha}$ . The following configurational energy is postulated,

$$\Upsilon_{\alpha} = \frac{\eta_{\alpha}}{8 T_{\alpha}} (2 \Gamma_{\alpha} - \mathbf{C}^e) : \mathbb{C}_0^{ip} : (2 \Gamma_{\alpha} - \mathbf{C}^e) \quad \text{with} \quad \mathbb{C}_0^{ip} = 4 \left. \frac{\partial^2 \Psi_{ip}^e}{\partial \mathbf{C}^e \otimes \partial \mathbf{C}^e} \right|_{\mathbf{C}^e = \mathbf{I}}, \quad (4)$$

where  $\eta_{\alpha}$  and  $T_{\alpha}$  are the viscosity and relaxation time parameters for network  $\alpha$ . Due to lack of out-of-plane experiments, the viscoelastic framework is solely applied to the in-plane modes of deformation. As such, the fourth order tensor  $\mathbb{C}_0^{ip}$  in (4) is the initial material tangent for the in-plane elastic energy. By inserting the energy in the dissipation inequality and using arguments by Coleman and Gurtin (1967), the second Piola-Kirchhoff stress in the intermediate configuration becomes,

$$\mathbf{F}^p \mathbf{S} \mathbf{F}^{pT} = 2 \frac{\partial \Psi_{oop}^e}{\partial \mathbf{C}^e} + 2 \frac{\partial \Psi_{ip}^e}{\partial \mathbf{C}^e} + \sum_{\alpha} \mathbf{Q}_{\alpha} \quad \text{with} \quad \mathbf{Q}_{\alpha} = \frac{\eta_{\alpha}}{2 T_{\alpha}} \mathbb{C}_0^{ip} : (\mathbf{C}^e - 2 \Gamma_{\alpha})$$

where  $\sum \mathbf{Q}_{\alpha}$  is the viscoelastic stress. The internal variable  $\Gamma_{\alpha}$  is defined from the following evolution law,

$$\dot{\Gamma}_{\alpha} + \frac{1}{T_{\alpha}} \Gamma_{\alpha} = \frac{1}{2 T_{\alpha}} \mathbf{C}^e,$$

which can be shown to fulfill the dissipation inequality.

### 4.3 Plasticity and viscoplasticity

As previously mentioned, the large degree of anisotropy between the out-of-plane and in-plane response requires a flexible yield surface. In Papers A and C, the Xia et al. (2002) yield surface is used. The yield surface is stated as,

$$f = \sum_{\nu=1}^{12} \langle \Omega \rangle_{\nu}^{2k} - 1 \quad \text{with} \quad \Omega_{\nu} = \frac{\boldsymbol{\tau} : \mathbf{n}_s^{(\nu)}}{K_0^{(\nu)} + K^{(\nu)}} \quad \text{and} \quad \langle (\bullet) \rangle = \begin{cases} (\bullet) & \text{if } (\bullet) > 0 \\ 0 & \text{otherwise} \end{cases}. \quad (5)$$

The subsurfaces ( $\nu$ ) corresponds to different modes of deformations defined by the second order tensors  $\mathbf{n}_s^{(\nu)} = \sum_{i=1}^3 \sum_{j=1}^3 N_{ij}^{(\nu)} \bar{\mathbf{v}}^{(i)} \otimes \bar{\mathbf{v}}^{(j)}$  with  $\bar{\mathbf{v}}^{(i)}$  being the characteristic vectors in (2) normalized and  $N_{ij}^{(\nu)}$  are the yield normal coefficients. Selected projections of the 12 subsurfaces are shown in Fig. 6.

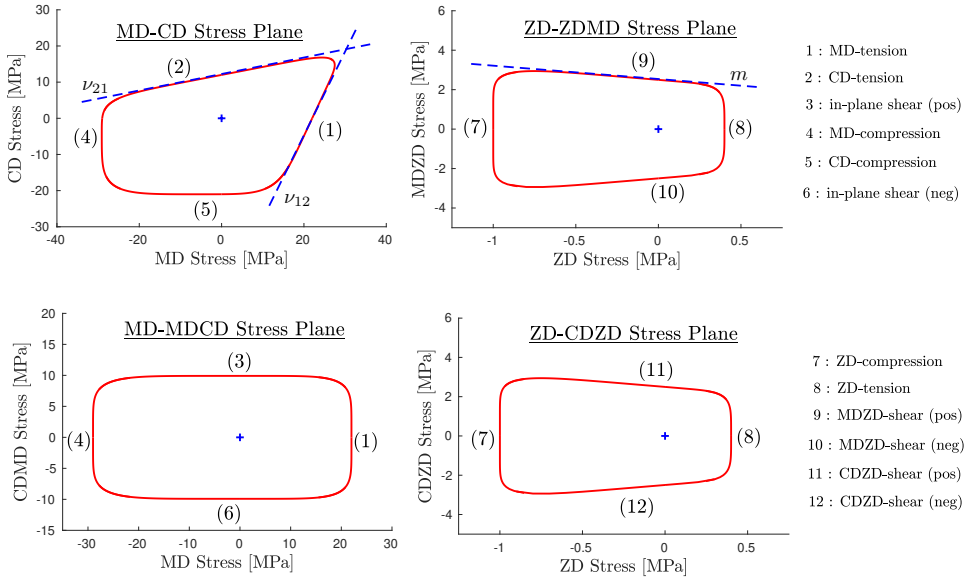


Figure 6: The yield surface  $f = 0$  projected along different planes.

The initial distance to the yield normals and the corresponding hardening are  $K_0^{(\nu)}$  and  $K^{(\nu)}(\kappa^{(\nu)})$ , respectively. The internal hardening variables associated with each subsurface are denoted  $\kappa^{(\nu)}$  and the parameter  $k$  in (5) determines the smoothness of the transition between the subsurfaces. In the rate-independent models, associated plasticity is adopted,

$$\mathbf{d}^p = \dot{\lambda} \frac{\partial f}{\partial \boldsymbol{\tau}} \quad \text{and} \quad \dot{\kappa}^{(\nu)} = -\dot{\lambda} \frac{\partial f}{\partial K^{(\nu)}}, \quad (6)$$

where  $\mathbf{d}^p$  is the plastic part of the spatial velocity gradient and  $\dot{\lambda}$  is the plastic multiplier which can be obtained using the yield criteria  $f = 0$  during plastic loading. To close the system of equations,

the plastic spin is postulated as

$$\boldsymbol{\omega}^p = \sum_{\nu=1}^{12} \dot{\lambda} H_\nu \text{skew}(\mathbf{n}_s^{(\nu)}) \quad \text{with} \quad H_\nu = \frac{2k \langle \Omega_\nu \rangle^{2k-1}}{K_0^{(\nu)} + K^{(\nu)}}$$

which is the skew-symmetric counterpart to  $\mathbf{d}^p = \sum_{\nu=1}^{12} \dot{\lambda} H_\nu \text{sym}(\mathbf{n}_s^{(\nu)})$  obtained from combining (5) and (6).

In Paper B, the rate-independent plasticity framework is extended to include viscoplasticity. Hence, the yield criteria and the plastic multiplier are replaced with viscoplastic multipliers. In contrast to the plastic multiplier, the viscoplastic multipliers are postulated via constitutive equations. Since no experimental evidence for rate-dependency during in-plane compression yet exists and the viscous effects for out-of-plane compression is low, two different viscoplastic multipliers are postulated,

$$\dot{\gamma}_1 = \alpha_1 \Phi_1^{p_1} \quad \text{and} \quad \dot{\gamma}_2 = \alpha_2 \langle \Phi_2 - 1 \rangle^{p_2}, \quad (7)$$

where  $\alpha_i$  and  $p_i$  are viscoplastic material parameters. The potential functions,  $\Phi_1$  and  $\Phi_2$ , in (7) are defined as,

$$\Phi_1 = \sum_{\nu=1, \nu \neq 4, 5, 7}^{12} \langle \Omega_\nu \rangle^{2k} \quad \text{and} \quad \Phi_2 = \sum_{\nu=4, 5, 7} \langle \Omega_\nu \rangle^{2k}.$$

The viscoplastic flow-rule for the symmetric velocity gradient  $\mathbf{d}^{vp}$  and the internal hardening variable  $\kappa^{(\nu)}$  are similar to the rate-independent model, i.e.

$$\mathbf{d}^{vp} = \dot{\gamma}_1 \frac{\partial \Phi_1}{\partial \boldsymbol{\tau}} + \dot{\gamma}_2 \frac{\partial \Phi_2}{\partial \boldsymbol{\tau}} \quad \text{and} \quad \dot{\kappa}^{(\nu)} = -\dot{\gamma}^{(\nu)} \frac{\partial \Phi^{(\nu)}}{\partial K^{(\nu)}},$$

where,

$$[\dot{\gamma}^{(\nu)}, \Phi^{(\nu)}] = \begin{cases} [\dot{\gamma}_2, \Phi_2] & \text{when } \nu = \{4, 5, 7\} \\ [\dot{\gamma}_1, \Phi_1] & \text{otherwise} \end{cases}.$$

#### 4.4 Damage model

The damage model in Paper C is used to capture the softening due to delamination generated during creasing and folding. The framework for the damage evolution is inspired by the work in Larsson et al. (2016). Since the material is assumed to weaken uniformly during delamination, a scalar damage variable  $\alpha$  is used to degrade the Helmholtz free energy  $\Psi = (1-\alpha) \Psi_0$  with  $\Psi_0$  being the undamaged energy in (1). The evolution of damage depends on the undamaged plastic dissipation  $\hat{D}$  obtained as,

$$\hat{D} = \sum_{\nu=1}^{12} \hat{D}_\nu \quad \text{with} \quad \hat{D}_\nu = K_0^{(\nu)} \dot{\kappa}^{(\nu)}. \quad (8)$$

The damage initiation criteria is

$$1 = \sum_{n \in P} \beta_n A_c^{(n)} \quad \text{with} \quad A_c^{(n)} = \int_0^{t_c} \hat{D}_n dt \quad (9)$$

where  $\beta_n$  are the damage initiation parameters and  $t_c$  is the critical damage initiation time. In (9),  $P$  is a subset of the 12 plastic dissipation modes. Since out-of-plane shear is assumed to drive the delamination during creasing and folding,  $P = \{9, 10, 11, 12\}$  is chosen in Paper C, i.e. the deformation modes associated with out-of-plane shearing. With the proposed framework the damage evolution becomes,

$$\alpha = \frac{\sum_{n \in P} (A_T^{(n)} - A_c^{(n)})}{\sum_{n \in P} c_n A_c^{(n)}}$$

where  $c_n$  are damage parameters and  $A_T^{(n)}$  are the accumulated plastic dissipation due to the subsurfaces, i.e.

$$A_T^{(n)} = \int_0^t \hat{D}_n dt \quad .$$

#### 4.5 Implementation and numerical considerations

Since many details related to the integration of the constitutive equations are omitted in the appended papers, this section provides the reader with additional implementation details. The mechanical behavior of a system is governed by the principle of virtual work which for quasistatic conditions requires

$$\frac{1}{2} \int_{V_0} \delta \mathbf{C} : \mathbf{S} dV - \int_{S_0^t} \delta \mathbf{u} \cdot \mathbf{t}_0 dS - \int_{V_0} \delta \mathbf{u} \cdot \mathbf{p}_0 dV = 0 \quad (10)$$

to be fulfilled for all admissible virtual displacements  $\delta \mathbf{u}$ . The traction forces  $\mathbf{t}_0$  acts on the undeformed surface  $S_0^t$  while  $\mathbf{p}_0$  are the body forces acting on the undeformed volume  $V_0$ . The first integral in (10) corresponds to the internal virtual work  $\delta W_{int}$  while the two last integrals are the external virtual work  $\delta W_{ext}$ . Assuming dead loading, the stiffness matrix is obtained from discretizing the linearization of the internal virtual work,

$$d(\delta W_{int}) = \int_{V_0} (\delta \mathbf{F}^t d\mathbf{F}) : \mathbf{S} dV + \frac{1}{4} \int_{V_0} \delta \mathbf{C}^t : \mathbb{D} : d\mathbf{C} dV \quad (11)$$

where  $\mathbb{D}$  is the algorithmic material tangent matrix. The implicit Abaqus standard solver is used to solve the balance of linear momentum with the paperboard model implemented as a user defined material routine UMAT, cf. Abaqus User's Manual (2013). The format for the tangent used as input to Abaqus reads,

$$\mathbb{D}^{aba} = J^{-1} \frac{\partial \boldsymbol{\tau}}{\partial \mathbf{F}} \cdot \mathbf{F}^t \quad (12)$$

with  $J = \det(\mathbf{F})$ . Based on the state variables in (3) the material tangent becomes,

$$\begin{aligned} J \cdot \mathbb{D}^{aba} = & \frac{d\boldsymbol{\tau}}{db^e} : \left( \frac{\partial \mathbf{b}^e}{\partial \mathbf{F}} \cdot \mathbf{F}^t + \frac{\partial b^e}{\partial \mathbf{F}^p} : \left( \frac{\partial \mathbf{F}^p}{\partial \mathbf{F}} \cdot \mathbf{F}^t \right) \right) \\ & + \frac{d\boldsymbol{\tau}}{d\mathbf{m}^{(\alpha)}} : \left( \frac{\partial \mathbf{m}^{(\alpha)}}{\partial \mathbf{F}} \cdot \mathbf{F}^t + \frac{\partial \mathbf{m}^{(\alpha)}}{\partial \mathbf{F}^p} : \left( \frac{\partial \mathbf{F}^p}{\partial \mathbf{F}} \cdot \mathbf{F}^t \right) \right) \end{aligned} \quad (13)$$

where the chain rule was used. To compute (13), the partial derivative  $\frac{\partial \mathbf{F}^p}{\partial \mathbf{F}}$  needs to be calculated. Based on the backward Euler discretization of the flow rule (6) and the yield criteria  $f = 0$ , the discrete constitutive equations becomes,

$$\begin{cases} \mathbf{R}_{F_p} = \mathbf{F}_{pre}^p - \mathbf{F}^p + \Delta\lambda \mathbf{F}^p \mathbf{F}^{-1} \mathbf{N}_s \mathbf{F} \\ R_{\kappa}^{(\nu)} = \kappa_{pre}^{(\nu)} - \kappa^{(\nu)} + \Delta\lambda H_{\nu} \Omega_{\nu} \\ R_f = \sum_{\nu=1}^{12} \langle \Omega_{\nu} \rangle^{2k} - 1 \end{cases} \quad \text{with} \quad \mathbf{N}_s = \sum_{\nu=1}^{12} H_{\nu} \mathbf{n}_s^{(\nu)} \quad (14)$$

where  $(\bullet)_{pre}$  refers to the previous equilibrium state and  $\mathbf{R}_{F_p}, R_{\kappa}^{(\nu)}, R_f$  is the set of residual equations. The system of discrete constitutive equations can, with Voigt notation ( $\hat{\bullet}$ ), be expressed as,

$$\mathbf{R}(\mathbf{Y}) = \mathbf{0} \quad \text{with} \quad \mathbf{R} = \begin{bmatrix} \hat{\mathbf{R}}_{F_p} \\ \mathbf{R}_{\kappa} \\ R_f \end{bmatrix} \quad \text{and} \quad \mathbf{Y} = \begin{bmatrix} \hat{\mathbf{F}}^p \\ \boldsymbol{\kappa} \\ \Delta\lambda \end{bmatrix} \quad (15)$$

where the column vectors  $\boldsymbol{\kappa}$  and  $\mathbf{R}_{\kappa}$  contain the twelve scalars  $\kappa^{(\nu)}$  and corresponding  $R_{\kappa}^{(\nu)}$ . The non-linear residual equation in (15) is solved in each integration point using Newton-Raphson updates,

$$\mathbf{R}^{(i+1)} \approx \mathbf{R}^{(i)} + \frac{\partial \mathbf{R}^{(i)}}{\partial \mathbf{Y}} d\mathbf{Y}^{(i+1)} = \mathbf{0} \quad \implies \quad \mathbf{Y}^{(i+1)} = \mathbf{Y}^{(i)} - \left[ \frac{\partial \mathbf{R}^{(i)}}{\partial \mathbf{Y}} \right]^{-1} \mathbf{R}^{(i)} \quad (16)$$

As the residual  $\mathbf{R}(\mathbf{Y}(\hat{\mathbf{F}}), \hat{\mathbf{F}}) = \mathbf{0}$  holds for all  $\hat{\mathbf{F}}$ , use is made of,

$$\frac{d\mathbf{R}}{d\hat{\mathbf{F}}} = \frac{\partial \mathbf{R}}{\partial \hat{\mathbf{F}}} + \frac{\partial \mathbf{R}}{\partial \mathbf{Y}} \frac{\partial \mathbf{Y}}{\partial \hat{\mathbf{F}}} = \mathbf{0}, \quad \implies \quad \frac{\partial \mathbf{Y}}{\partial \hat{\mathbf{F}}} = - \left[ \frac{\partial \mathbf{R}}{\partial \mathbf{Y}} \right]^{-1} \frac{\partial \mathbf{R}}{\partial \hat{\mathbf{F}}} \quad (17)$$

such that  $\frac{\partial \mathbf{F}^p}{\partial \mathbf{F}}$ , needed in (13), is obtained from  $\frac{\partial \mathbf{Y}}{\partial \hat{\mathbf{F}}}$ . The Jacobian,

$$\frac{\partial \mathbf{R}}{\partial \mathbf{Y}} = \begin{bmatrix} \frac{\partial \mathbf{R}_1}{\partial \mathbf{Y}_1} & \cdots & \frac{\partial \mathbf{R}_1}{\partial \mathbf{Y}_{22}} \\ \vdots & & \vdots \\ \frac{\partial \mathbf{R}_{22}}{\partial \mathbf{Y}_1} & \cdots & \frac{\partial \mathbf{R}_{22}}{\partial \mathbf{Y}_{22}} \end{bmatrix} = \begin{bmatrix} \frac{\partial \hat{\mathbf{R}}_{F_p}}{\partial \hat{\mathbf{F}}_p} & \frac{\partial \hat{\mathbf{R}}_{F_p}}{\partial \boldsymbol{\kappa}} & \frac{\partial \hat{\mathbf{R}}_{F_p}}{\partial \Delta\lambda} \\ \frac{\partial \mathbf{R}_{\kappa}}{\partial \hat{\mathbf{F}}_p} & \frac{\partial \mathbf{R}_{\kappa}}{\partial \boldsymbol{\kappa}} & \frac{\partial \mathbf{R}_{\kappa}}{\partial \Delta\lambda} \\ \frac{\partial R_f}{\partial \hat{\mathbf{F}}_p} & \frac{\partial R_f}{\partial \boldsymbol{\kappa}} & \frac{\partial R_f}{\partial \Delta\lambda} \end{bmatrix}$$

in (16) is cumbersome but straightforward to compute. Some of the key derivatives are provided in Fig. 7.

$$\left\{ \begin{array}{l}
\frac{\partial R_{F^p}}{\partial \mathbf{F}^p} = -\mathbf{I} \bar{\otimes} \mathbf{I} + \Delta \lambda \mathbf{I} \bar{\otimes} (\mathbf{F}^{-1} \mathbf{N}_s \mathbf{F})^t + \Delta \lambda \mathbf{F}^p \cdot \mathbf{F}^{-1} \cdot \left[ \left( \frac{\partial \mathbf{N}_s}{\partial \mathbf{F}^p} \right)^T \cdot \mathbf{F} \right]^T \\
\frac{\partial R_{K^{(\nu)}}}{\partial \mathbf{F}^p} = \Delta \lambda \frac{2k H_\nu}{K_0^{(\nu)} + K^{(\nu)}} \left( \text{sym}(\mathbf{n}_s^{(\nu)}) : \frac{\partial \boldsymbol{\tau}}{\partial \mathbf{F}^p} + \boldsymbol{\tau} : \frac{\partial \mathbf{n}_s^{(\nu)}}{\partial \mathbf{F}^p} \right) \\
\frac{\partial R_f}{\partial \mathbf{F}^p} = \sum_{\nu=1}^{12} H_\nu \left( \text{sym}(\mathbf{n}_s^{(\nu)}) : \frac{\partial \boldsymbol{\tau}}{\partial \mathbf{F}^p} + \boldsymbol{\tau} : \frac{\partial \mathbf{n}_s^{(\nu)}}{\partial \mathbf{F}^p} \right) \\
\frac{\partial \mathbf{N}_s}{\partial \mathbf{F}^p} = \sum_{\nu=1}^{12} H_\nu \left[ \frac{(2k-1)\Omega_\nu^{-1}}{K_0^{(\nu)} + K^{(\nu)}} \mathbf{n}_s^{(\nu)} \otimes \left( \text{sym}(\mathbf{n}_s^{(\nu)}) : \frac{\partial \boldsymbol{\tau}}{\partial \mathbf{F}^p} + \boldsymbol{\tau} : \frac{\partial \mathbf{n}_s^{(\nu)}}{\partial \mathbf{F}^p} \right) + \frac{\partial \mathbf{n}_s^{(\nu)}}{\partial \mathbf{F}^p} \right] \\
\frac{\partial \boldsymbol{\tau}}{\partial \mathbf{F}^p} = \frac{\partial \boldsymbol{\tau}}{\partial \mathbf{b}^e} : \frac{\partial \mathbf{b}^e}{\partial \mathbf{F}^p} + \frac{\partial \boldsymbol{\tau}}{\partial \mathbf{m}^{(\alpha)}} : \frac{\partial \mathbf{m}^{(\alpha)}}{\partial \mathbf{F}^p} \\
\frac{\partial \mathbf{n}_s^{(\nu)}}{\partial \mathbf{F}^p} = \left( \sum_{\beta=1}^2 \frac{\partial \mathbf{n}_s^{(\nu)}}{\partial \bar{\mathbf{v}}^{(\beta)}} \cdot \frac{\partial \bar{\mathbf{v}}^{(\beta)}}{\partial \mathbf{v}^{(\beta)}} \cdot \frac{\partial \mathbf{v}^{(\beta)}}{\partial \mathbf{F}^p} \right) + \frac{\partial \mathbf{n}_s^{(3)}}{\partial \bar{\mathbf{v}}^{(3)}} \cdot \frac{\partial \bar{\mathbf{v}}^{(3)}}{\partial \mathbf{v}^{(3)}} \cdot \frac{\partial \mathbf{v}^{(3)}}{\partial \mathbf{F}^p} \\
\frac{\partial \mathbf{b}^e}{\partial \mathbf{F}^p} = -\mathbf{F}^e \bar{\otimes} \mathbf{b}^e \mathbf{F}^{-t} - \mathbf{b}^e \mathbf{F}^{-t} \bar{\otimes} \mathbf{F}^e \\
\frac{\partial \mathbf{m}^{(\beta)}}{\partial \mathbf{F}^p} = -\mathbf{F}^e \bar{\otimes} (\mathbf{m}^{(\beta)} \mathbf{F}^{-t}) - (\mathbf{m}^{(\beta)} \mathbf{F}^{-t}) \bar{\otimes} \mathbf{F}^e, \quad \beta = 1, 2 \\
\frac{\partial \mathbf{m}^{(3)}}{\partial \mathbf{F}^p} = \mathbf{F}^{-t} \bar{\otimes} (\mathbf{m}^{(3)} \mathbf{F}^e) + (\mathbf{m}^{(3)} \mathbf{F}^e) \bar{\otimes} \mathbf{F}^{-t} - 2 \mathbf{m}^{(3)} \otimes (\mathbf{F}^p)^{-t} \\
\frac{\partial \mathbf{n}_s^{(\nu)}}{\partial \bar{\mathbf{v}}^{(\alpha)}} = \sum_{j=1}^3 N_{\alpha j}^{(\nu)} \mathbf{I} \bar{\otimes} \bar{\mathbf{v}}^{(j)} + \sum_{i=1}^3 N_{i\alpha}^{(\nu)} \bar{\mathbf{v}}^{(i)} \otimes \mathbf{I}, \quad \alpha = 1, 2, 3 \\
\frac{\partial \bar{\mathbf{v}}^{(\alpha)}}{\partial \mathbf{v}^{(\alpha)}} = \frac{1}{|\mathbf{v}^{(\alpha)}|} \left( \mathbf{I} - \frac{1}{|\mathbf{v}^{(\alpha)}|^2} \mathbf{m}^{(\alpha)} \right), \quad \alpha = 1, 2, 3 \\
\frac{\partial \mathbf{v}^{(\beta)}}{\partial \mathbf{F}^p} = -\mathbf{F}^e \otimes \mathbf{F}^{-p} \mathbf{v}_0^{(\beta)}, \quad \beta = 1, 2 \\
\frac{\partial \mathbf{v}^{(3)}}{\partial \mathbf{F}^p} = \mathbf{F}^{-t} \bar{\otimes} (\mathbf{F}^e)^t \mathbf{v}^{(3)} - \mathbf{v}^{(3)} \otimes (\mathbf{F}^p)^{-t}
\end{array} \right.$$

Figure 7: Subset of partial derivatives in the Jacobian.

## 5 Computational modeling of converting processes

Converting a paperboard sheet into a package involves creasing and folding. During creasing, damage is initiated along predefined lines that guides the upcoming folding operation. A proper converting process is crucial to ensure the structural integrity of the package. In this process, package corners are particularly sensitive, cf. Beldie et al. (2001), since the creased lines intersect. In addition, a quality crease is instrumental in creating sharp folding lines without cracks, cf. Bota et al. (2022), a matter that is of great importance for pleasing the consumers.

To evaluate the performance of a paperboard, laboratory line-creasing and line-folding setups are often used since they provide consistent experimental results. The line-creasing and line-folding setup are schematically illustrated in Fig. 8.

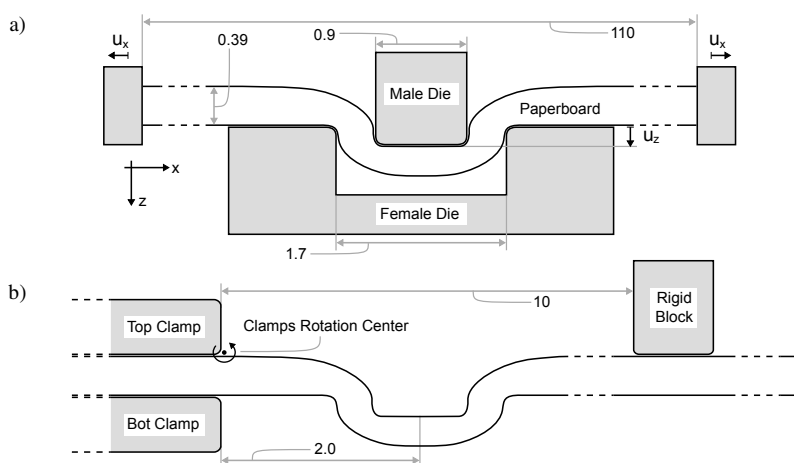


Figure 8: a) Schematics of the line-creasing setup and b) subsequent line-folding procedure, dimensions in mm. Image is reproduced from Paper C.

As seen in Fig. 8, the line-creasing setup consists of a paperboard strip placed between a male die and a female cavity. Initially, the paperboard strip is clamped along the edges and pre-strained to mimic the effect of webtension. During creasing, the male die is displaced towards the female cavity while the reaction force and the displacement of the male die is recorded along with the evolving webtension. After the male die and webtension is removed, a localized highly deformed region that acts like a hinge during folding is formed, see Fig. 8b. The folding setup is depicted in Fig. 8b where the creased paperboard strip is clamped close to the creased region. During folding, the motion of the paperboard, induced by the rotation of the clamps, is restricted by a rigid block such that bending occurs. In this process, the rotation angle is recorded together with the reaction force at the rigid block. Creasing and folding, based on the schematics in Fig. 8, has been simulated with the developed models. In Fig. 9, two numerical simulations are compared against experimental images of the creasing and folding process.

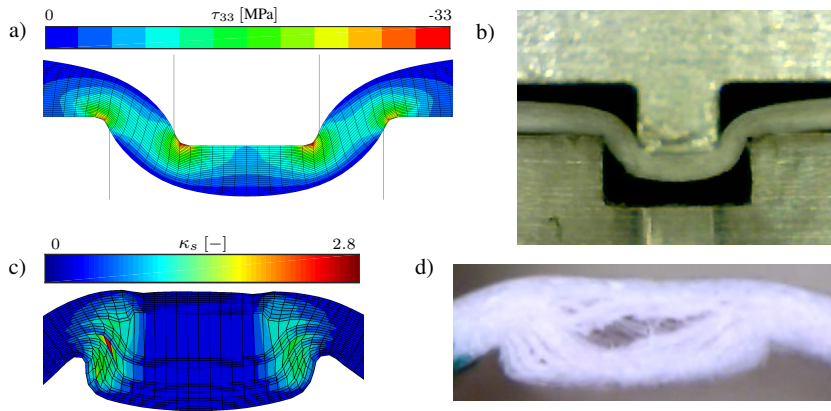


Figure 9: Comparing simulations and experimental images for line-creasing and line-folding. Figures reproduced from Papers B, C and D.

A creasing simulation at maximum male die displacement and the corresponding experiment is shown in Fig. 9a-b. The simulation in Fig. 9a shows that the out-of-plane stress distribution is highly inhomogeneous and localized to the corner of the male die. In Fig. 9c-d, a sample folded to  $90^\circ$  and thereafter unloaded is shown. Again, the plastic shear strains are very inhomogeneous. The viscous behavior during line-creasing has been studied in Paper B and a selection of the results are presented in Fig. 10.

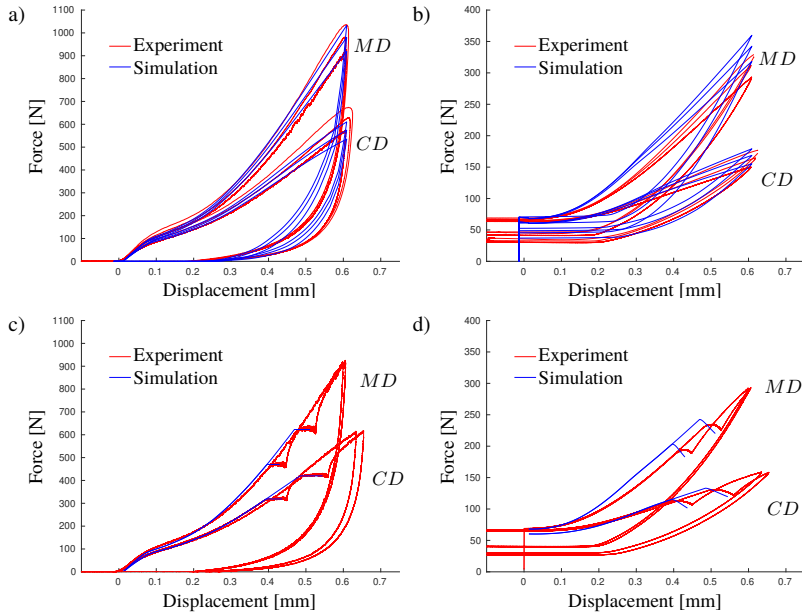


Figure 10: Line-creasing measurements compared to simulations. Figure is reproduced from Paper B.

The response for three different operating speeds are shown in Fig. 10a-b where the model is in overall agreement with the experimental results. This rate-dependency is important since the operating speed is prone to fluctuate in industrial converting processes. In Fig. 10c-d, the creep behavior of paperboard is investigated for line-creasing where the male die reaction force is kept constant for 30 seconds while the male die displacement and webtension is recorded. Accurate creep modeling of the creased region is important for box compression applications where packages are stacked such that the creased corners are subject to static loads for long durations. The line-creasing and subsequent line-folding results from Paper C is shown in Fig. 11.

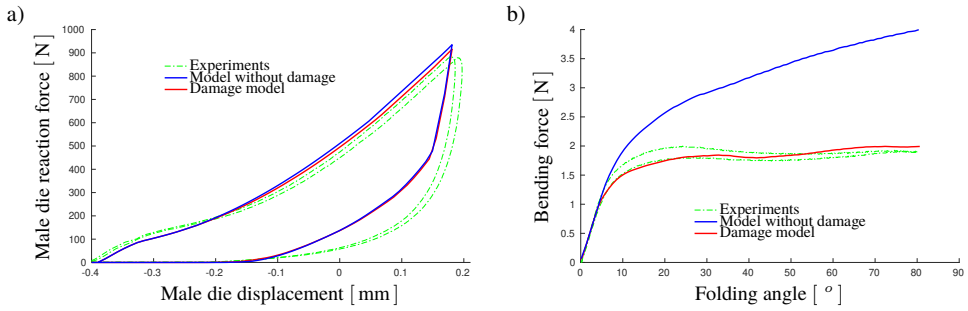


Figure 11: Force response during creasing and subsequent folding. Figure is reproduced from Paper C.

The simulated response with and without damage using a setup aligned with the MD direction, is compared to experimental tests. As seen in Fig. 11b, the damage model is instrumental to accurately capture the mechanical response during folding. In addition, the damage framework is not degrading the quality of the model response during creasing as seen in Fig. 11a. Apart from improving the model capacity, accurate modeling of folding is crucial since it is used to calculate the relative crease strength, RCS, which is an index used in industry to assess paperboard quality. The RCS is defined as the ratio between the maximum force obtained from folding a creased sample and folding an uncreased sample.

Industrial creasing and folding is evidently more complex than line-creasing and folding, however, the deformation modes present during loading remains similar. In an industrial setting, creasing is often performed in a continuous manner by a rotational setup where the male and female patterns are imprinted on cylindrical tools, cf. Borgqvist et al. (2015). To create packages, the creased material is used in an aseptic filling machine in which packages are formed and sealed in tandem with packaging the liquid food product. A schematic of an aseptic filling machine is shown in Fig. 12.

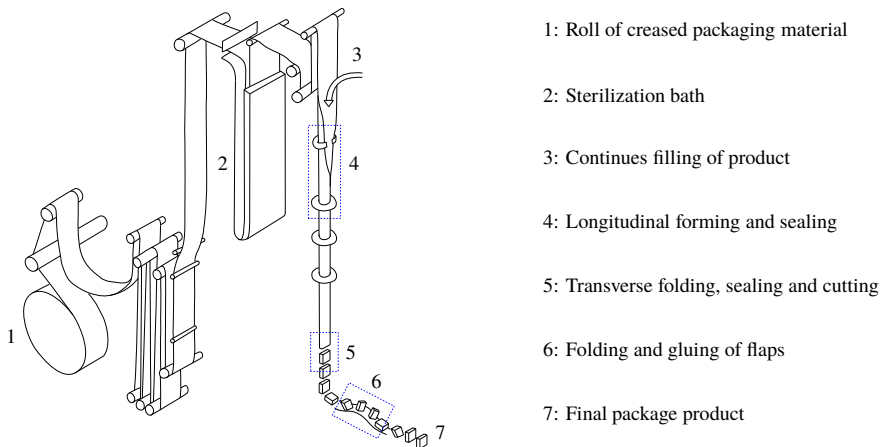


Figure 12: Schematics of an aseptic filling machine

As shown in Fig. 12, the forming process can be divided into three main steps. In the stage prior to forming, the package material travels through a number of flexible rollers, to stabilize the web tension, followed by an aseptic bath for sterilization. The resulting flat package material is longitudinally formed and sealed into a cylindrical shape by a set of consecutive rings. During this process, the liquid product is pumped into the package at constant flow provided by a valve system. The longitudinal forming is followed by a transverse forming stage where a set of forming jaws transversely folds, seals and cut the cylindrical tube into a semi-finished package. In the final stage, the flaps are folded and glued such that a rectangular shape is obtained.

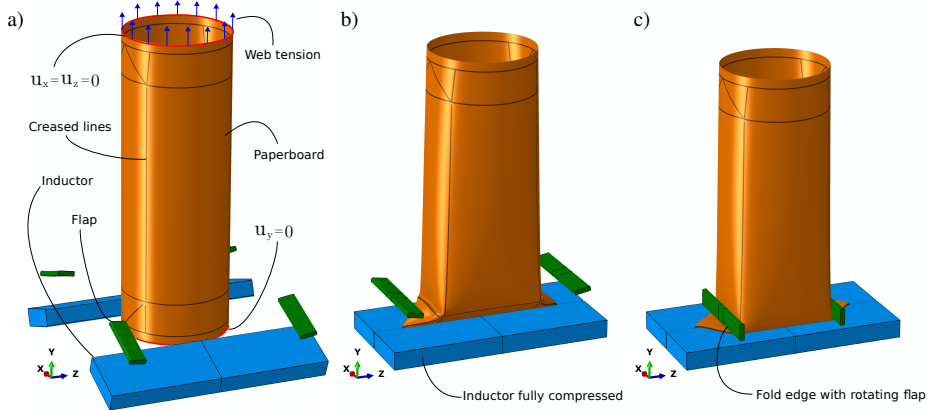


Figure 13: Tube forming simulation. Figure is reproduced from Paper A.

As an illustrative example in Paper A, a simplified transverse folding sequence was simulated. The process consists of two folding steps and it is illustrated in Fig. 13 together with the boundary conditions. In the simulation, the rate-independent paperboard model was combined with special solid-shell elements such that the finite element mesh could be discretized with a single element in the paperboard thickness. An internal pressure was applied to simulate the liquid interaction while the creased lines were modeled by degrading the material parameters to match the creased line-folding experiments.

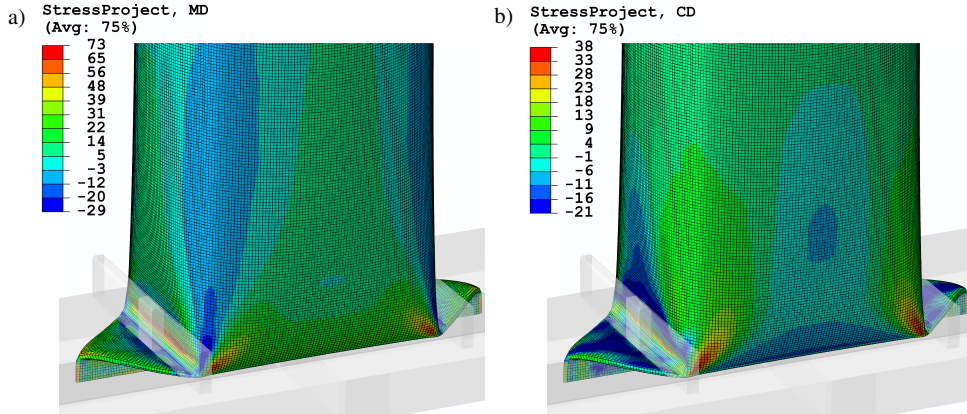


Figure 14: Final stage of tube forming with the Kirchhoff stress projected along the a) MD and b) CD direction, respectively. Figure is reproduced from Paper A.

The solid-shell and material model was implemented in Abaqus explicit with the user element routine VUEL and the problem was solved using explicit time integration. The permanent deformation after the transverse folding simulation is shown in Fig. 14a-b together with the projected Kirchhoff stress along the MD and CD direction, respectively. As expected, the in-plane stress is concentrated along the crease lines which is notably pronounced around the corner of the package where both compressive and tensile stresses are present.

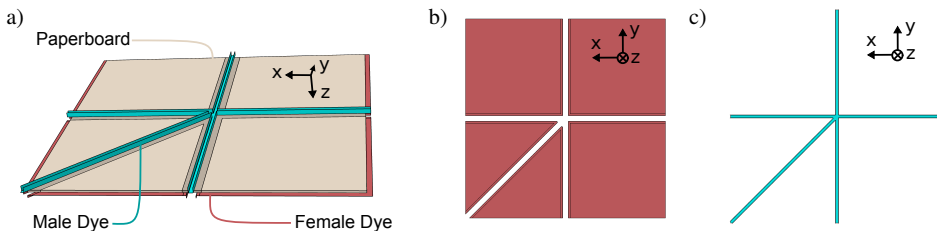


Figure 15: Plate creasing simulation. Figure is reproduced from Paper C.

While the simulation in Fig. 14 can be used as an indication for in-plane crack formation, a more accurate prediction is obtained by also simulating the creasing step. The deformation history during creasing and folding of a package corner is studied in Paper C since it is critical to the performance of the final package. Fig. 15 shows the creasing setup where the imprinted patterns of the male and female tools are chosen such that vertical, horizontal and diagonal creases are obtained after one creasing step. As opposed to the tube forming simulation in Fig. 13, the creased cross sections are discretized using several elements through the thickness and the developed damage model is used. Implicit time integration is adopted for both the creasing and folding simulations.

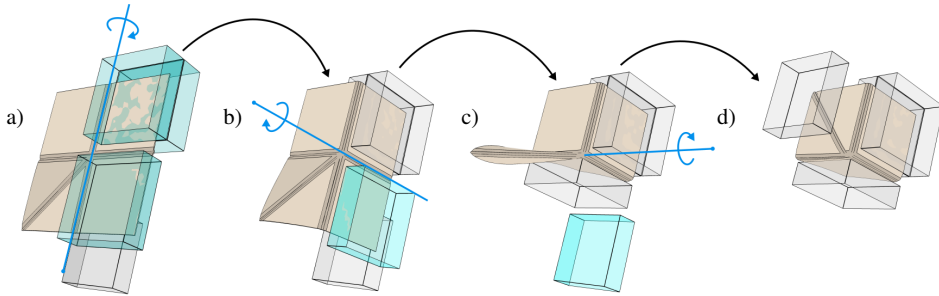


Figure 16: Simulation of the folding sequence to produce a corner of a package. Figure is reproduced from Paper C.

After creasing, three folding steps as illustrated in Fig. 16 follows. These steps are conceptually similar to the three forming steps in the filling machine. In the initial sequence, Fig. 16a→b, rigid blocks are used to fold the vertical creased line similar to the longitudinal forming step in Fig. 12. In Fig. 16b→c, the horizontal crease is folded, mimicking the horizontal forming in Fig. 12. This step creates a flap from the diagonally creased line. In the final sequence, Fig. 16c→d, the flap is folded similar to the last folding stage depicted in Fig. 12.

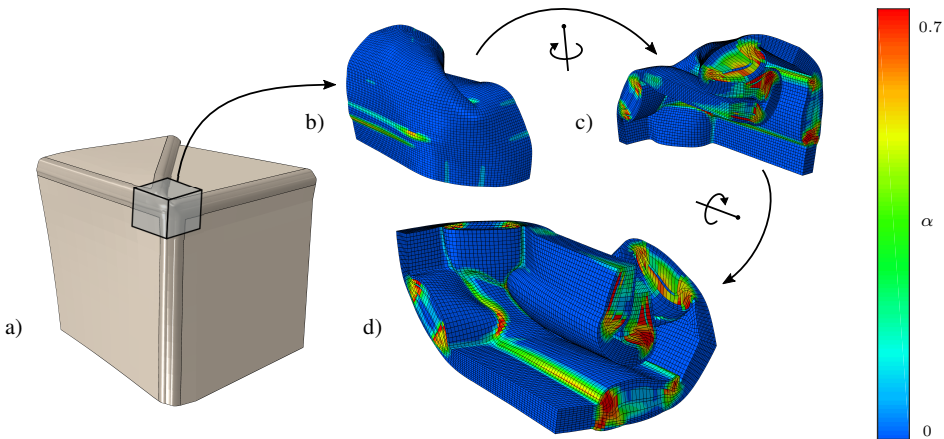


Figure 17: A slice of the package corner after the converting process. Figure is reproduced from Paper C.

The advantage of the simulation in Paper C, compared to the tube simulation in Paper A, is the capability to more accurately study the complex deformation patterns inside the corner of the package. Such analysis is shown in Fig. 17 where a slice of the package corner is studied with regards to the deformation and the accumulated damage. An analysis of this kind is key for evaluating the converting process since it is difficult to perform similar experimental measurements inside the package.

## 6 Future work

Continuum paperboard models, and their numerical treatments, has been developed and evaluated for converting processes involving creasing and folding. For simplicity, paperboard was modeled as a single ply structure which is an assumption that is valid for a number of commercial boards. Future works include efficient ways to model the heterogeneity that arise in multi-layered paperboard. Furthermore, to model packaging material, the inclusion of the polymer films and aluminum layers is needed. An important aspect in this pursuit, that requires further research, is how to model and measure the adhesion between the interfaces of the composite layers. Measuring the interface response is a fundamental issue since it is challenging to separate the material and interface response in any experimental test.

The models presented in this work ignores temperature and moisture dependency which in many cases are significant. This approach is reasonable when paperboard is a part of packaging material since the outer-layers, i.e. polymer and aluminum, acts as barriers against the environment. However, to fully model paperboard, the temperature and moisture dependency should be included. It would also be interesting to investigate the possibility to calibrate the models based on DIC data, and possibly x-ray tomography, in combination with cleverly designed experiments that activates different deformation modes, i.e. inverse calibration. With this approach, it might be possible to calibrate a large number of material parameters with a single experimental test.

While current models can predict critical stress regions that are susceptible to in-plane cracks, the models do not include in-plane fracture such that crack propagation can be simulated. In view of this, a potential avenue for further research is to include in-plane fracture into the modeling frameworks.

## 7 Summary of the appended papers

**Paper A:** A state-of-the-art solid-shell element is combined with a state-of-the-art continuum model for paperboard to allow for efficient simulations of large-scale forming applications. The element technique is based on reduced integration with hourglass stabilization and naturally includes the thickness direction without imposing the plane stress constraint. Numerical examples are considered where the new approach is shown to be more efficient than conventional fully integrated brick elements. The stability of the method is illustrated with a large-scale tube forming example.

**Paper B:** The elasto-plastic continuum paperboard framework in Paper A is extended to model the observed rate-dependent response for paperboard. To include viscoelasticity connected to the in-plane material response, a thermodynamically consistent generalization is made of the rheological Maxwell framework. In addition, viscoplasticity is introduced by two potential functions that separates compression from shear and tension. The model is calibrated with good agreement to uniaxial experiments where different loading rates are considered together with creep and relaxation tests. The model is evaluated against line-creasing and line-folding measurements.

**Paper C:** The large-strain continuum model for paperboard in Paper A is combined with a ductile damage framework to enhance the capacity to predict the delamination process. The framework for the evolution of damage is postulated similar to plasticity theory with the driving force being part of the accumulated plastic dissipation. The non-proportional loadcase of line-creasing and subsequent line-folding is used to calibrate the damage framework. To adequately capture the response, a single isotropic damage variable is needed that evolves with the dissipation associated with out-of-plane shear. An empirical approach is suggested to mitigate the inherent mesh dependency. The model is illustrated with a simulation where a paperboard sheet is creased and folded to mimic a package corner.

**Paper D:** During converting operations, paperboard is subject to large out-of-plane compressive stresses followed by tension and delamination. To study this loadcase, an experimental device and protocol is developed for cyclic, uniaxial, out-of-plane loading. A compliant initial response is observed during compression which is shown to originate from the paperboard surface roughness, hence not a material behavior. The gluing procedure that permits cyclic loading is shown to mitigate the initial compliant response. Novel cyclic loading experiments are performed. The material response is shown to be smooth when loading between compression and tension. Hence a switch function, introduced in previous works, that separates the elastic response in compression and tension is deemed as questionable.

## References

- Alava, M., Niskanen, K., 2006. The physics of paper. *Reports on Progress in Physics* 69, 669–723.
- Alexandersson, M., 2020. Macroscopic modelling of coupled multiphysics in swelling cellulose based materials. Ph.D. thesis, Lund Institute of Technology.
- Askfelt, H., 2016. Continuum modeling of the coupled transport of mass, energy, and momentum in paperboard. Ph.D. thesis, Lund Institute of Technology.
- Bedzra, R., Li, Y., Reese, S., Simon, J., 2019. A comparative study of a multi-surface and a non-quadratic plasticity model with application to the in-plane anisotropic elastoplastic modelling of paper and paperboard. *Journal of Composite Materials* 53, 753–767.
- Beex, L., Peerlings, R., 2009. An experimental and computational study of laminated paperboard creasing and folding. *International Journal of Solids and Structures* 46, 4192–4207.
- Beex, L., Peerlings, R., 2012. On the influence of delamination on laminated paperboard creasing and folding. *Phil. Trans. R. Soc.* 370, 1912–1924.
- Beldie, L., Sandberg, G., Sandberg, L., 2001. Paperboard packages exposed to static loads - finite element modelling and experiments. *Packaging Technology and Science* 14, 171–178.
- Borgqvist, E., Lindström, T., Wallin, M., Tryding, J., Ristinmaa, M., 2014. Distortional hardening plasticity model for paperboard. *International Journal of Solids and Structures* 51, 2411–2423.
- Borgqvist, E., Wallin, M., Ristinmaa, M., Tryding, J., 2015. An anisotropic in-plane and out-of-plane elasto-plastic continuum model for paperboard. *Composite Structures* 126, 184–195.
- Borgqvist, E., Wallin, M., Tryding, J., Ristinmaa, M., Tudisco, E., 2016. Localized deformation in compression and folding of paperboard. *Packaging Technology and Science* 29, 397–414.
- Borodulina, S., Motamedian, H., Kulachenko, A., 2018. Effect of fiber and bond strength variations on the tensile stiffness and strength of fiber networks. *International Journal of Solids and Structures* 154, 19–32.
- Bota, J., Pibernik, J., Kovacevic, D., Brozovic, M., 2022. The effects of flatbed creasing tool on printed paperboard. Conference: 11th International Symposium on Graphic Engineering and Design.
- Coleman, B., Gurtin, M., 1967. Thermodynamics with internal state variables. *Journal of Chemical Physics* 47, 597–613.
- Harrysson, A., Ristinmaa, M., 2008. Large strain elasto-plastic model of paper and corrugated board. *International Journal of Solids and Structures* 45, 3334–3352.
- Heyden, S., 2000. Network modelling for the evaluation of mechanical properties of cellulose fibre fluff. PhD Thesis, Department of Mechanics and Materials, Lund University.

- Huang, H., Hagman, A., Nygård, M., 2014. Quasi static analysis of creasing and folding for three paperboards. *Mechanics of Materials journal* 69, 11–34.
- Huang, H., Nygård, M., 2010. A simplified material model for finite element analysis of paperboard creasing. *Nordic Pulp and Paper Research Journal* 25, 505–512.
- Kulachenko, A., Uesaka, T., 2012. Direct simulations of fiber network deformation and failure. *Mechanics of Materials* 51, 1–14.
- Larsson, R., Razanica, S., Josefson, B., 2016. Mesh objective continuum damage models for ductile fracture. *International journal for numerical methods in engineering* 106, 840–860.
- Lavrykov, S., Lindström, S. B., Singh, K., Ramarao, B., 2012. 3d network simulations of paper structure. *Nordic Pulp and Paper Research Journal*, 256–263.
- Li, Y., Stapleton, S., Reese, S., Simon, J., 2016. Anisotropic elastic-plastic deformation of paper: In-plane model. *International Journal of Solids and Structures* 100-101, 286–296.
- Li, Y., Stapleton, S., Reese, S., Simon, J., 2018. Anisotropic elastic-plastic deformation of paper: Out-of-plane model. *International Journal of Solids and Structures* 130-131, 172–182.
- Mäkelä, P., Östlund, S., 2003. Orthotropic elastic–plastic material model for paper materials. *International Journal of Solids and Structures* 40, 5599–5620.
- Mandel, J., 1971. *Plasticité classique et viscoplasticité. Courses and Lectures, No. 97, ICMS, Udine, Springer, Wien-New York.*
- Manual, A. U., 2013. *Dassault Systemes Simulia, 6th Edition.*
- Marin, G., Nygård, M., Östlund, S., 2020. Stiffness and strength properties of five paperboards and their moisture dependency. *Tappi Journal* 19, 71–85.
- Ottosen, N., Ristinmaa, M., 2005. *The mechanics of constitutive modeling, first edition Edition. Elsevier.*
- Persson, J., Isaksson, P., 2014. A mechanical particle model for analyzing rapid deformations and fracture in 3d fiber materials with ability to handle length effects. *International Journal of Solids and Structures* 51, 2244–2251.
- Pfeiffer, M., Kolling, S., 2019. A non-associative orthotropic plasticity model for paperboard under in-plane loading. *International Journal of Solids and Structures* 166, 112–123.
- Retulainen, E., Niskanen, K., Nilsen, N., 1998. *Fibers and bonds, 2nd Edition. Vol. 16. Finnish Paper Engineers Association.*
- Simon, J., 2020. A review of recent trends and challenges in computational modeling of paper and paperboard at different scales. *Archives of Computational Methods in Engineering.*

- Stenberg, N., Fellers, C., 2002. Out-of-plane poisson's ratios of paper and paperboard. *Nordic Pulp and Paper Research Journal* 17, 387–394.
- Tjahjanto, D., Girlanda, O., Östlund, S., 2015. Anisotropic viscoelastic-viscoplastic continuum model for high-density cellulose-based materials. *Journal of the Mechanics and Physics of Solids* 84, 1–20.
- Xia, Q., Boyce, M., Parks, D., 2002. A constitutive model for the anisotropic elastic-plastic deformation of paper and paperboard. *International Journal of Solids and Structures* 39, 4053–4071.



# Paper A

Kristofer Robertsson, Eric Borgqvist, Mathias Wallin, Matti Ristinmaa,  
Johan Tryding, Andrea Giampieri and Umberto Perego

*Efficient and accurate simulation of the packaging forming process*

Packaging Technology and Science 31 (2018), 557-566



# Efficient and accurate simulation of the packaging forming process

Kristofer Robertsson<sup>1</sup>, Eric Borgqvist<sup>2</sup>, Mathias Wallin<sup>1</sup>, Matti Ristinmaa<sup>1</sup>,  
Johan Tryding<sup>1,2</sup>, Andrea Giampieri<sup>3</sup> and Umberto Perego<sup>4</sup>

<sup>1</sup>Division of Solid Mechanics, Lund University, P.O Box 118, 221 00, Sweden

<sup>2</sup>Tetra Pak Packaging Solutions, Lund, 221 86, Sweden

<sup>3</sup>Tetra Pak Packaging Solutions S.p.A., Modena, 411 00, Italy

<sup>4</sup>Department of Civil and Environmental Engineering, Politecnico di Milano, Milan, 201 33, Italy

## Abstract

To allow for large-scale forming applications, such as converting paperboard into package containers, efficient and reliable numerical tools are needed. In finite element simulations of thin structures, elements including structural features are required to reduce the computational cost. Solid-shell elements based on reduced integration with hourglass stabilization is an attractive choice. One advantage of this choice is the natural inclusion of the thickness, not present in standard degenerated shells, which is especially important for many problems involving contact. Furthermore, no restrictions are imposed on the constitutive models since the solid-shell element does not require the plane stress condition to be enforced. In this work, a recently proposed efficient solid-shell element is implemented together with a state of the art continuum model for paperboard. This approach is validated by comparing the obtained numerical results with experimental results for paperboard as well as with those found by using 3D continuum elements. To show the potential of this approach, a large-scale forming simulation of paperboard is used as a proof of concept.

# 1 Introduction

Paperboard is a light-weight cellulose-based fibrous material where the large degree of anisotropy, together with the high bending stiffness, makes it suitable for converting into packaging containers. The large degree of anisotropy stems from the manufacturing process where fibers are continuously sprayed along a single direction, denoted the Machine Direction MD. The transverse direction to MD and the stacking direction for the fibers are denoted CD and ZD, respectively. The failure stress in ZD is typically two orders of magnitude lower than CD, which in turn is approximately 2-3 times lower than MD. One approach to model fibrous materials is to consider the micro structure and try to mimic the characteristics of the cellulose fiber network. In Kulachenko et al. [16], beam elements were used to represent individual fibers together with a model for the dynamic bonding between the fibers. Other micro-mechanical models for the fibrous network includes Wilbrink et al. [30], Sliseris et al. [27], Beex et al. [3] and Bosco et al. [8]. The aforementioned network models are useful to gain insight of governing mechanisms at the micro-scale but for large-scale problems the computational cost of network models is too demanding and continuum based models are therefore necessary. Several attempts to model paperboard within a continuum framework have been proposed in the literature over the last decades. For modeling of the creasing and folding process, Beex et al. [2] used an in-plane elasto-plastic model with Hill's anisotropic yield surface together with cohesive elements to model the out-of-plane delamination zones. In Harrysson et al. [13], a large strain orthotropic elasto-plastic model based on the Tsai-Wu yield criteria was established for paperboard. More recently, models based on the complex anisotropic yield surface introduced by Xia et al. [32] have gained popularity. Such models include the in-plane paperboard models established in Borgqvist et al. [5], Li et al. [17] and Tjahjanto et al. [28]. The latter model is a viscoelastic-viscoplastic small strain approach developed to capture creep and relaxation for transient uniaxial loading.

The paperboard model considered in this work is the continuum model recently developed by Borgqvist et al. [6] using the modified Helmholtz free energy proposed in [7]. The model is formulated for large-deformations in the spatial configuration using a thermodynamically consistent framework. Onset of plasticity is modeled with a modified version of the anisotropic yield surface proposed in Xia et al. [32] where several subsurfaces are introduced in order to capture the complex yield behavior of paperboard. The paperboard model has previously been utilized to study a number of industrial applications. In Borgqvist et al. [6], a numerical study of the creasing process was considered using a simplified line-creasing operation as well as a more realistic, 3D-rotational setup. Furthermore, it was shown in Borgqvist et al. [7] that the paperboard model was able to capture the formation of wrinkles for both the line-folding process of un-creased paperboard and for the short-span compression test. These simulations were based on the finite element formulation using solid brick elements. Several layers of elements through the paperboard thickness were necessary to capture the bending behavior, resulting in a large number of degrees of freedom, which makes the approach unfeasible for large-scale applications. A more computationally efficient implementation is discussed in this paper, based on the use of solid-shell finite elements.

Thin structures, coupled with dominating bending-modes, motivate the use of shell elements. When simulating forming processes of paperboard, the large areas of contact motivate the use of an explicit dynamic finite element solver. For explicit dynamic finite element simulations of thin geometries subject to bending, the classical shell element developed by Belytschko et al. [4] is often

used due to its simplicity and speed. In classical shell theory, kinematic assumptions for the cross sections are imposed on the governing equilibrium equations and the generated elements are two-dimensional with displacements and rotations as nodal degrees of freedom. The imposed constraints on the finite element formulation have to be accounted for in the constitutive law, usually in terms of a plane stress condition, i.e. a 3D continuum based material model needs to be expressed in the state of plane stress.

Solid-shell elements are three-dimensional elements where the nodal degrees of freedoms are represented by displacements. Geometrically they are similar to conventional continuum elements, the difference appears in the element formulation where the solid-shell element has a distinct thickness direction in order to improve the elements accuracy for thin shell problems. The thickness stretch is naturally incorporated in the formulation of solid-shell elements, which allows for the use of the full 3D material model without modifying the constitutive model. An accurate description of the thickness stretch is especially important for applications involving double-sided contact, which is the case when considering forming processes of paperboard in large scale applications. Potential disadvantage for solid-shell elements is the stable time-step length in explicit simulations which is based on the smallest dimension of the element, i.e. the thickness dimension of the solid-shell determines the time-step. The influence of the thickness on the stable time step can however be almost completely compensated by the selective mass scaling method, cf. Cocchetti et al. [9].

The solid-shell element proposed by Schwarze et al. [23] and [22] is utilized in this work. The element is developed for large deformations and the formulation is based on reduced in-plane integration together with hourglass stabilization. The number of integration points in the thickness direction is allowed to vary in order to capture highly non-linear variations in the thickness direction. Key features in the element formulation includes methods to relieve element locking, i.e. the enhanced assumed strain (EAS) method and the assumed natural strain (ANS) method, together with a Taylor expansion of the stress state along the thickness direction in order to improve accuracy for shell problems. Only one EAS degree of freedom is needed in the element formulation which, together with reduced in-plane integration, results in a computationally efficient element formulation suitable for explicit dynamics simulations as demonstrated in Pagani et al. [21]. The solid-shell element has been previously utilized together with cohesive elements in Pagani et al. [20] to model the industrial application of dynamic blade cutting with promising results. In Vladmirov et al. [29] and Schwarze et al. [24], forming of sheet metal was modeled with the solid-shell element using both isotropic and anisotropic constitutive laws together with finite strain plasticity.

In the forming process of paperboard creased lines are introduced where the mechanical properties are reduced such that high quality packages are obtained. The influence on mechanical properties due to line-creasing of different creasing depths followed by subsequent line-folding was experimentally investigated by Nagasawa et al. [18]. Attempts have been made in the literature to numerically model this process using cohesive interface models, accounting for the delamination and damage during creasing, cf. Xia [31], Huang et al. [14] and Beex et al. [1]. The aforementioned models are developed with the aim to study the creasing operation locally and they are therefore not suitable for large-scale forming applications. Another modeling approach aimed towards large-scale forming was proposed by Giampieri et al. [12] where an interface element was developed to represent the crease. The crease element was connected to two classical shell elements of Mindlin-Reissner type and a constitutive model for the interface was developed accounting for elasto-plasticity and damage. In the present

paper, as damage is not included in the model the creased lines have been modeled by a reduction of the material parameters, these have been estimated using experimental data from line-creasing followed by subsequent line-folding.

The present paper is organized as follows. In section 2, key aspects of the solid-shell formulation are summarized while section 3 is devoted to introduce the material model for paperboard. In section 4, the solid-shell element using the paperboard model is validated by means of implicit finite element simulations, the results are compared with experimental measurements and solutions obtained from fully integrated continuum elements. In section 5, a large-scale, explicit, forming simulation of paperboard is considered to demonstrate the potential application of the approach.

## 2 Solid-shell Formulation based on the ANS and the EAS Concepts

In this work, the eight-node hexahedral solid-shell element proposed by Schwarze and Reese in [23] is implemented and below, some key aspects of the element formulation are outlined.

The starting point is the weak formulation of the balance of linear momentum defined as the following two field functional,

$$g_1 = \int_{V_0} \delta \mathbf{E}_c : \mathbf{S}(\mathbf{E}) dV + \int_{V_0} \rho_0 \delta \mathbf{u} \cdot \ddot{\mathbf{u}} dV + g_{ext} \quad (1)$$

$$g_2 = \int_{V_0} \delta \mathbf{E}_e : \mathbf{S}(\mathbf{E}) dV = 0 \quad (2)$$

which is obtained from the enhanced assumed strain (EAS) method where the Green-Lagrange strain  $\mathbf{E}$  is additively separated into two parts,  $\mathbf{E} = \mathbf{E}_c + \mathbf{E}_e$ . The compatible part  $\mathbf{E}_c$  is a sole function of the displacements  $\mathbf{u}$  while the enhanced part  $\mathbf{E}_e$  is a sole function of the enhanced degrees of freedoms  $\mathbf{W}$  which are introduced in order to remove element locking. The EAS method dates back to the work by Simo and Armero in [25]. In the weak formulation,  $\delta$  denotes a variation,  $g_{ext}$  is the virtual work from the external loading,  $\mathbf{S}$  is the second Piola-Kirchhoff stress while  $V_0$  and  $\rho_0$  are the volume and mass density defined in the material configuration. The material coordinates  $\mathbf{X}$  and the displacement vector  $\mathbf{u}$  are approximated via

$$\mathbf{X} = \sum_{I=1}^8 N_I \mathbf{X}_I \quad \text{and} \quad \mathbf{u} = \sum_{I=1}^8 N_I \mathbf{u}_I \quad \text{with} \quad N_I = \frac{1}{8}(1 + \xi_I \xi)(1 + \eta_I \eta)(1 + \zeta_I \zeta) \quad (3)$$

where index  $I$  refers to the node value while  $N_I$  are the corresponding tri-linear shape functions of isoparametric coordinates  $\xi_1 = \xi$ ,  $\xi_2 = \eta$  and  $\xi_3 = \zeta$ . To further modify the Green-Lagrange strain, the relationship between the components in the isoparametric domain  $\bar{E}_{\xi_i \xi_j}$  and the material domain  $E_{ij}$  is needed. The coordinate transformation is defined by  $E_{ij} = \hat{j}_{ki} \hat{j}_{lj} \bar{E}_{\xi_k \xi_l}$  with  $\hat{j}_{ij} = \partial \xi_i / \partial X_j$  being the components of the inverse Jacobian. Using Voigt matrix notation  $\hat{\mathbf{E}} = [E_{11}, E_{22}, E_{33}, E_{12}, E_{23}, E_{13}]^T$ , the compact format  $\hat{\mathbf{E}} = \mathbf{T} \bar{\hat{\mathbf{E}}}$  is obtained and by performing a Taylor expansion of the inverse Jacobian, the transformation matrix is approximated as a linear polynomial expression  $\mathbf{T} \approx \mathbf{T}^0 + \xi \mathbf{T}^\xi + \eta \mathbf{T}^\eta + \zeta \mathbf{T}^\zeta$  with  $\mathbf{T}^{(\bullet)}$  being constant matrices.

The Assumed Natural Strain (ANS) method, proposed by Hughes and Tezduyar [15], is adopted for the compatible strain,  $\hat{\bar{\mathbf{E}}}_c$ , where components responsible for locking are replaced by interpolations between sampling points along the element boundary in which no locking will occur. To remove curvature thickness locking and element shear locking, the ANS interpolation is applied to the transverse normal strain  $(\hat{\bar{\mathbf{E}}}_c)_{33}$  and the transverse shear components,  $(\hat{\bar{\mathbf{E}}}_c)_{13}$  and  $(\hat{\bar{\mathbf{E}}}_c)_{23}$ . From the ANS interpolation, the transverse normal strain  $(\bar{\mathbf{E}}_c)_{33}$  is constant in the out-of-plane direction  $\zeta$  while the in-plane normal strains,  $(\bar{\mathbf{E}}_c)_{11}$  and  $(\bar{\mathbf{E}}_c)_{22}$ , are linear with respect to its corresponding natural coordinate,  $\xi$  and  $\eta$ . To overcome Poisson thickness locking and volumetric locking, the transverse normal strain  $(\bar{\mathbf{E}}_c)_{33}$  is also required to be linear with respect to  $\zeta$ . The EAS contribution  $\hat{\bar{\mathbf{E}}}_e$  is therefore modeled with only one enhanced degree of freedom  $W_e$  according to the following simple expression,

$$\hat{\bar{\mathbf{E}}}_e = \mathbf{T}^0 \hat{\bar{\mathbf{B}}}_e W_e = \hat{\mathbf{B}}_e W_e \quad \text{with} \quad \hat{\bar{\mathbf{B}}}_e = \{0, 0, \zeta, 0, 0, 0\}^T \quad (4)$$

where the transformation matrix  $\mathbf{T}^0$  is evaluated at the center of the element in order to fulfill the patch test. Further modification to the compatible Green-Lagrange strain is conducted with a Taylor expansion, of quadratic order, at the center of the element,

$$\hat{\bar{\mathbf{E}}}_c \approx \underbrace{\hat{\mathbf{E}}_c^0 + \zeta \hat{\mathbf{E}}_c^\zeta + \zeta^2 \hat{\mathbf{E}}_c^{\zeta\zeta}}_{\hat{\mathbf{E}}_c^*} + \underbrace{\xi \hat{\mathbf{E}}_c^\xi + \eta \hat{\mathbf{E}}_c^\eta + \xi \eta \hat{\mathbf{E}}_c^{\xi\eta} + \eta \zeta \hat{\mathbf{E}}_c^{\eta\zeta} + \xi \zeta \hat{\mathbf{E}}_c^{\xi\zeta}}_{\hat{\mathbf{E}}_c^{hg}} \quad (5)$$

where  $\hat{\mathbf{E}}_c^{(\bullet)}$  are constant matrices. The compatible strain  $\hat{\bar{\mathbf{E}}}_c$  is separated into one part  $\hat{\mathbf{E}}_c^*$ , related to the out-of-plane integration, and one part  $\hat{\mathbf{E}}_c^{hg}$ , not effected by the numerical integration but instead related to the hourglass stabilization associated with reduced integration.

One key feature of the shell formulation is the Taylor expansion of the second Piola Kirchhoff stress along the out-of-plane direction  $\boldsymbol{\xi}^* = (0, 0, \zeta)^T$  which reads,

$$\hat{\mathbf{S}} = \underbrace{\hat{\mathbf{S}}(\hat{\mathbf{E}}_c^*)}_{\hat{\mathbf{S}}^*} + \underbrace{\frac{\partial \hat{\mathbf{S}}}{\partial \hat{\mathbf{E}}}}_{\mathbf{C}^*} \bigg|_{\boldsymbol{\xi}=\boldsymbol{\xi}^*} \left( \xi \hat{\mathbf{E}}_c^\xi + \eta \hat{\mathbf{E}}_c^\eta + \eta \zeta \hat{\mathbf{E}}_c^{\eta\zeta} + \xi \zeta \hat{\mathbf{E}}_c^{\xi\zeta} \right) = \hat{\mathbf{S}}^* + \hat{\mathbf{S}}^{hg} \quad (6)$$

where the same separation between the parts related to the out-of-plane integration  $\hat{\mathbf{S}}^*$  and the hourglass stabilization  $\hat{\mathbf{S}}^{hg}$  is introduced together with the Voigt notation. To reduce complexity for the hourglass stabilization part, the material tangent  $\mathbf{C}^*$  is replaced by a constant deviatoric matrix  $\mathbf{C}^{hg} = \mu_{eff}^{hg} \hat{\mathbf{I}}^{dev}$  where  $\hat{\mathbf{I}}^{dev}$  is the Voigt notation of the fourth-order tensor  $\mathcal{I}^{dev} = \mathcal{I} - (1/3) \mathbf{I} \otimes \mathbf{I}$  with  $\mathbf{I}$  and  $\mathcal{I}$  being the second and fourth order identity tensors. For elastic deformations, the effective shear modulus  $\mu_{eff}^{hg}$  is defined as the initial in-plane shear modulus while for plastic deformation it is modeled by the following adaptive expression

$$\mu_{eff}^{hg} = \left( \sum_{i=1}^{n_{gp}} \omega_i \mu_i^{hg} \right) / \left( \sum_{i=1}^{n_{gp}} \omega_i \right) \quad \text{with} \quad \mu_i^{hg} = \frac{1}{2} \left( \frac{\mathbf{S}^{* dev} : \mathbf{S}^{* dev}}{\mathbf{E}^{* dev} : \mathbf{E}^{* dev}} \right)_i^{1/2} \quad (7)$$

where  $n_{gp}$  is the number of Gauss integration points and  $\omega_i$  are the corresponding weights.

Before integrating the two field functionals (1) and (2), the approximation  $dV = j^0 d\xi d\eta d\zeta$  is made for the volume element where  $j^0$  denotes the determinant of the Jacobian matrix  $J_{ij} = \partial X_i / \partial \xi_j$  evaluated at the center of the element. The discretized weak element formulations, corresponding to (1) and (2), are expressed as,

$$\mathbf{G}_1 = \mathbf{R}_u^{hg} + \mathbf{R}_u^* + \mathbf{M} \ddot{\mathbf{u}} - \mathbf{G}_{ext} \quad \text{and} \quad G_2 = 0 \quad (8)$$

with  $\mathbf{M}$  being the element mass matrix and  $\mathbf{G}_{ext}$  is the external element force vector. The residuals related to the hourglass stabilization  $\mathbf{R}_u^{hg}$ , the out-of-plane integration  $\mathbf{R}_u^*$  and the enhanced part of the weak formulation  $G_2$ , are derived as

$$\mathbf{R}_u^{hg} = \frac{8}{3} \left( \hat{\mathbf{B}}_c^{\xi T} \mathbf{C}^{hg} \hat{\mathbf{E}}_c^\xi + \hat{\mathbf{B}}_c^{\eta T} \mathbf{C}^{hg} \hat{\mathbf{E}}_c^\eta \right) j^0 + \frac{8}{9} \left( \hat{\mathbf{B}}_c^{\eta \zeta T} \mathbf{C}^{hg} \hat{\mathbf{E}}_c^{\eta \zeta} + \hat{\mathbf{B}}_c^{\xi \zeta T} \mathbf{C}^{hg} \hat{\mathbf{E}}_c^{\xi \zeta} \right) j^0 \quad (9)$$

$$\mathbf{R}_u^* = \int_{-1}^1 \left( \hat{\mathbf{B}}_c^0 + \zeta \hat{\mathbf{B}}_c^\zeta + \zeta^2 \hat{\mathbf{B}}_c^{\zeta \zeta} \right)^T \hat{\mathbf{S}}^* d\zeta 4 j^0 \quad (10)$$

$$G_2 = \int_{-1}^1 \hat{\mathbf{B}}_c^T \hat{\mathbf{S}}^* d\zeta 4 j^0 \quad (11)$$

where  $\hat{\mathbf{B}}_c$  are matrices relating the compatible strains to the displacements  $\hat{\mathbf{E}}_c = \hat{\mathbf{B}}_c \mathbf{u}$ , as such, they have the same polynomial format as the Green-Lagrange strain in (5).

From the discretized weak element formulations in (8), static condensation is utilized in order to update the enhanced degree of freedom  $W_e$  at the element level as established in Simo et al. [26]. For the explicit dynamic finite element formulation, the explicit estimate proposed in Pagani et al. [21] is utilized which requires only one iteration in the updating procedure of the enhanced degree of freedom. The tangent in this updating procedure is calculated numerically to avoid the computation of the algorithmic material stiffness which is a computationally demanding task for complex constitutive models.

### 3 Material Model for Paperboard

The constitutive relation, used to model the paperboard material, is the anisotropic elasto-plastic continuum model developed by Borgqvist et al. [6] with the modified version of the Helmholtz free energy as proposed in Borgqvist et al. [7]. Some of the key features of the material model are outlined below.

The model is developed in the spatial configuration in terms of the Kirchhoff stress tensor,  $\boldsymbol{\tau}$ . A multiplicative split of the deformation gradient  $\mathbf{F} = \mathbf{F}^e \mathbf{F}^p$  is assumed where  $\mathbf{F}^e$  corresponds to the elastic deformation while  $\mathbf{F}^p$  represents the permanent, plastic, deformation.

The in-plane anisotropy is modeled by two director vectors,  $\mathbf{v}_0^{(1)}$  and  $\mathbf{v}_0^{(2)}$ , defined in the material configuration and aligned with the MD and the CD direction, respectively. The out-of-plane material behavior in the thickness direction, ZD, is described by a director vector  $\mathbf{n}_0^{(3)}$  which is defined to be orthogonal to MD and CD, i.e.  $\mathbf{n}_0^{(3)} = \mathbf{v}_0^{(1)} \times \mathbf{v}_0^{(2)}$ . This choice for the out-of-plane director vector follows from the assumption that paperboard can be considered as an idealized layered structure, details regarding this assumption are presented in [6]. The in-plane director vectors are assumed to

follow the elastic part of the deformation gradient while the out-of-plane director vector is constructed to be orthogonal to the updated in-plane directors, i.e.

$$\mathbf{v}^{(1)} = \mathbf{F}^e \mathbf{v}_0^{(1)}, \quad \mathbf{v}^{(2)} = \mathbf{F}^e \mathbf{v}_0^{(2)} \quad \text{and} \quad \mathbf{n}^{(3)} = J^e \mathbf{F}^{e-T} \mathbf{n}_0^{(3)} \quad (12)$$

with  $J^e$  being the determinant of the elastic deformation gradient. The Helmholtz free energy is assumed to be a function of the elastic Finger tensor  $\mathbf{b}^e = \mathbf{F}^e (\mathbf{F}^e)^T$  and the structural tensors  $\mathbf{m}^{(1)} = \mathbf{v}^{(1)} \otimes \mathbf{v}^{(1)}$ ,  $\mathbf{m}^{(2)} = \mathbf{v}^{(2)} \otimes \mathbf{v}^{(2)}$ ,  $\mathbf{m}^{(3)} = \mathbf{n}^{(3)} \otimes \mathbf{n}^{(3)}$  using the following invariants,

$$I_{11} = \sqrt{\mathbf{m}^{(1)} : \mathbf{I}}, \quad I_{12} = \sqrt{\mathbf{m}^{(2)} : \mathbf{I}}, \quad I_{13} = \frac{1}{J^e} \sqrt{\mathbf{m}^{(3)} : \mathbf{b}^e \mathbf{b}^e}, \quad I_{23} = \sqrt{\mathbf{m}^{(3)} : \mathbf{I}} \quad (13)$$

where  $I_{11}$ ,  $I_{12}$  and  $I_{13}$  represents the magnitude of stretch in MD, CD and ZD respectively. The last invariant,  $I_{23}$  corresponds to deformation of a surface element where the normal vector of the surface area is aligned with the ZD direction.

Thermodynamical consistency is enforced via fulfillment of the dissipation inequality under thermostatic conditions. The elastic and plastic contribution of the Helmholtz free energy are assumed to be additively separable and furthermore, the elastic part of the energy is split into  $\rho_0 \Psi^e = \rho_0 \Psi_{ip}^e + \rho_0 \Psi_{op}^e$  where the in-plane behavior,  $\rho_0 \Psi_{ip}^e$ , is separated from the out-plane-plane part,  $\rho_0 \Psi_{op}^e$ . The two parts of the elastic contribution to Helmholtz free energy are defined as,

$$\begin{aligned} \rho_0 \Psi_{ip}^e &= A_1 \left( I_{11} + \frac{1}{I_{11}} - 2 \right) + A_2 \left( I_{12} + \frac{1}{I_{12}} - 2 \right) + A_4 \left( I_{11} + I_{12} + \frac{1}{I_{23}} - 3 \right) \\ \rho_0 \Psi_{op}^e &= H A_3 \left( I_{13} + \frac{1}{I_{13}} - 2 \right) + (1 - H) A_6 \left( (I_{13})^2 + \frac{1}{A_7} e^{-A_7((I_{13})^2 - 1)} - 2 \right) \\ &\quad + A_5 (I_{11} I_{12} I_{13} - J^e) \end{aligned} \quad (14)$$

with  $A_i$  being a set of elastic material parameters and  $H$ , a switch function with the properties of being  $H = 1$  when the out-of-plane direction is undergoing tension,  $I_{13} \geq 1$ , and zero in the case of compression,  $I_{13} < 1$ .

From the dissipation inequality and the arguments by Coleman and Noll [10] it follows that the Kirchhoff stress tensor is given as,

$$\boldsymbol{\tau} = 2\rho_0 \left( \frac{\partial \Psi}{\partial \mathbf{b}^e} \mathbf{b}^e + \frac{\partial \Psi}{\partial \mathbf{m}^{(1)}} \mathbf{m}^{(1)} + \frac{\partial \Psi}{\partial \mathbf{m}^{(2)}} \mathbf{m}^{(2)} + \frac{\partial \Psi}{\partial \mathbf{m}^{(3)}} \mathbf{m}^{(3)} + \left( \frac{\partial \Psi}{\partial \mathbf{m}^{(3)}} : \mathbf{m}^{(3)} \right) \mathbf{I} \right). \quad (15)$$

The onset of plastic deformation is modeled by a yield surface,  $f$ , in which the elastic domain is defined by  $f \leq 0$ . The yield surface used herein was proposed in Xia et al. [32] and it consists of several subsurfaces in order to capture anisotropic plasticity. Six subsurfaces are utilized for the in-plane directions together with six additional subsurfaces for the out-of-plane direction. The explicit expression for the yield-surface reads,

$$f(\boldsymbol{\tau}, \mathbf{n}_s^{(\beta)}, K^{(\beta)}) = \sum_{\nu=1}^{12} \mathcal{X}^{(\nu)} \left( \frac{\boldsymbol{\tau} : \mathbf{n}_s^{(\nu)}}{K_0^{(\nu)} + K^{(\nu)}} \right)^{2k} - 1 \quad (16)$$

where the second order tensors  $\mathbf{n}_s^{(\nu)}$  are defining the normal to the subsurface  $\nu$  according to,

$$\mathbf{n}_s^{(\nu)} = \sum_{i=1}^3 \sum_{j=1}^3 N_{ij}^{(\nu)} \bar{\mathbf{v}}^{(i)} \otimes \bar{\mathbf{v}}^{(j)}, \quad \bar{\mathbf{v}}^{(1)} = \frac{\mathbf{v}^{(1)}}{|\mathbf{v}^{(1)}|}, \quad \bar{\mathbf{v}}^{(2)} = \frac{\mathbf{v}^{(2)}}{|\mathbf{v}^{(2)}|}, \quad \bar{\mathbf{v}}^{(3)} = \frac{\mathbf{n}^{(3)}}{|\mathbf{n}^{(3)}|} \quad (17)$$

with  $N_{ij}^{(\nu)}$  being the coefficients defining the yield normal. The exponent  $k$  is a material parameter while  $\mathcal{X}^{(\nu)}$  are switch functions which determines if the subsurfaces are active  $\mathcal{X}^{(\nu)} = 1$  or inactive  $\mathcal{X}^{(\nu)} = 0$ . A subsurface is active if the inequality  $\boldsymbol{\tau} : \mathbf{n}_s^{(\nu)} > 0$  holds. The material parameters  $K_0^{(\nu)}$  represents the distance from the origin to the initial subsurface while  $K^{(\nu)}$  are the corresponding hardening variables associated with the internal variables  $\kappa^{(\nu)}$ . All subsurfaces are modeled as being ideal plastic, except for the following subsurfaces,

$$\begin{aligned} K^{(\nu)} &= a_\nu \ln(b_\nu \kappa^{(\nu)} + 1) & \nu &= \{1, 2, 3, 6\} \\ K^{(\nu)} &= a_\nu \kappa^{(\nu)} & \nu &= 7 \end{aligned} \quad (18)$$

where  $a_\nu$  and  $b_\nu$  are hardening parameters. In (18), the subsurfaces  $\nu = \{1, 2, 3, 6\}$  corresponds to in-plane tension and in-plane shear, while  $\nu = 7$  is the subsurface for out-of-plane compression, cf. Appendix A. Assuming associated plasticity, the evolution for the plastic deformation gradient, together with the internal variables, can be expressed as,

$$\begin{aligned} \dot{\mathbf{F}}^p &= \mathbf{F}^{e-1} \left( \sum_{\gamma=1}^{12} \dot{\lambda} H_\gamma \mathbf{n}_s^{(\gamma)} \right) \mathbf{F} \\ \dot{\kappa}^{(\nu)} &= \dot{\lambda} H_\nu \left( \frac{\boldsymbol{\tau} : \mathbf{n}_s^{(\nu)}}{K_0^{(\nu)} + K^{(\nu)}} \right) \end{aligned} \quad (19)$$

where the plastic multiplier  $\dot{\lambda}$  was introduced together with the following function,

$$H_\nu = \frac{2k \mathcal{X}^{(\nu)}}{K_0^{(\nu)} + K^{(\nu)}} \left( \frac{\boldsymbol{\tau} : \mathbf{n}_s^{(\nu)}}{K_0^{(\nu)} + K^{(\nu)}} \right)^{2k-1}. \quad (20)$$

When using the implicit finite element method, the evolution equations in (19) are discretized with the implicit backward Euler method and the resulting residuals, together with the yield criteria  $f = 0$ , are solved with a Newton Raphson iterative scheme. For explicit dynamics using the finite element method, the explicit Euler forward method is utilized when integrating the constitutive laws which is motivated by the small time-steps used in the explicit finite element code, cf. [19].

## 4 Numerical Examples

The aim of this section is to validate the performance of the solid-shell element, denoted Q1STs, when combined with the material model for paperboard previously outlined. For this endeavor, a number of static problems are considered using the implicit, static, finite element method. The numerical results are compared to experimental data, when such data exists, otherwise, they are compared to solutions obtained from the fully integrated bilinear continuum element, denoted C3D8 elements, which are available in the commercial software Abaqus [11]. The implicit Q1STs solid-shell element is implemented in the Abaqus framework by means of the user-element UEL subroutine and the material model is embedded into the element code with the user-material UMAT subroutine. The material parameters adopted for the paperboard model are the same as in Borgqvist et al. [7] and they are tabulated in appendix A for the sake of completeness.

## 4.1 Homogeneous deformation with one element

As the first step in the validation process, the paperboard material is subject to homogeneous deformation, and as such, only a single element is considered in the element mesh. Furthermore, only two integration points are used through the thickness of the board. The geometric ratio between the in-plane length,  $l$ , and the thickness,  $t$ , of the specimen is,  $l/t = 10$ .

Experimental data for in-plane uniaxial tension is provided in Borgqvist et al. [6] where tension is applied along three different directions MD, CD and  $45^\circ$  between MD and CD. Reliable data for out-of-plane uniaxial compression is also provided in [6]. The measured experimental data and the numerical results are compared in Fig. 1 where the resulting force-displacement curves are normalized with respect to the initial area  $A_0$  and the initial length  $l_0$ .

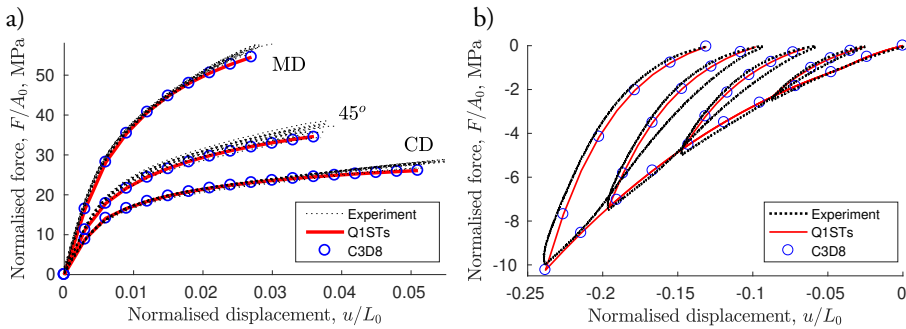


Figure 1: Comparing experimental response (black) to numerical results (red) for uniaxial deformation. a) Uniaxial in-plane tension. b) Uniaxial out-of-plane compression.

Simple-shear, where the sheared boundary of the specimen is constrained to be parallel to the fixed boundary during deformation, is also considered. Both in- and out-of-plane shear as well as uniaxial out-of-plane tension are considered. No reliable experimental data are available for the aforementioned deformation modes and as such the numerical response from the Q1STs solid-shell element, in Fig. 2, is compared to numerical results obtained by the C3D8 continuum element. The same time step is used for both elements and, for the sake of completeness, the numerical results obtained from the C3D8 element are also presented for the case of uniaxial tension in Fig. 1.

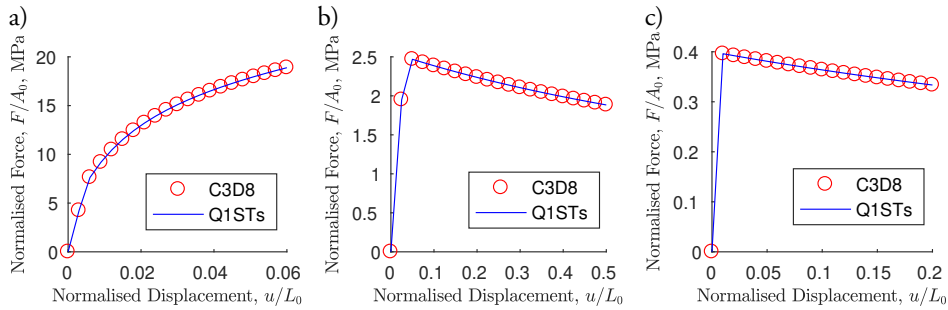


Figure 2: Response for the C3D8 continuum element and the Q1STs solid-shell element. a) In-plane simple shear. b) Out-of-plane simple shear. c) Uniaxial out-of-plane tension.

In summary, the numerical results in Fig. 1 follow the overall patterns of the measured data. Furthermore, the material response for the Q1STs solid-shell element in Fig. 2 match the response of the fully integrated C3D8 continuum element. From the above statements, it is concluded that the Q1STs solid-shell element is able to reproduce the mechanical response for a homogeneous deformation gradient when combined with the highly anisotropic paperboard model.

## 4.2 Paperboard cylinder subject to compressing motion

The second example in the verification process consists of a tube made of paperboard subject to a compressive motion from two rigid clamps, illustrated in Fig. 3a, where a vertical displacement is imposed on the clamps in direction towards each other. The clamps are modeled as analytically rigid surfaces and contact between the rigid clamps and the paperboard is assumed to be frictionless. Symmetry allows for the model to be reduced to one eighth of the original problem, as shown in Fig. 3b. The machine direction MD for the paperboard is oriented along the cylinder, i.e. in the direction of the  $z$ -axis in Fig. 3b.

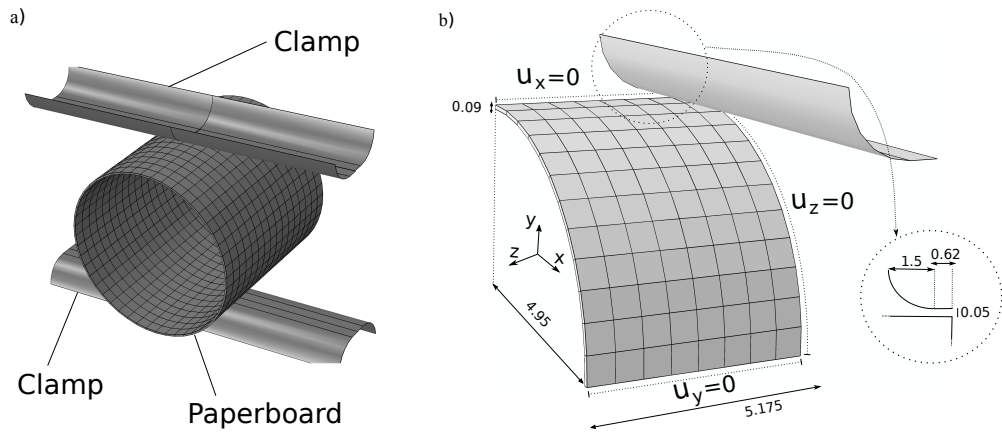


Figure 3: Paperboard compressed by two clamps. a) Original setup. b) Imposed symmetry together with initial in-plane mesh, geometry provided in *mm*.

No experimental measurements exist for the aforementioned problem and, as such, a mesh consisting of Q1STs elements is compared to a mesh consisting of C3D8 continuum elements. Five elements through the thickness are used in the C3D8 continuum mesh while for the Q1STs solid-shell, a single element is used in the thickness direction along with eight integration points. The number of elements and integration points are enough to guarantee that sufficient resolution is obtained with respect to the thickness direction of the paperboard, i.e. more integration points will only influence the results to a modest extent as is shown in Fig. 4.

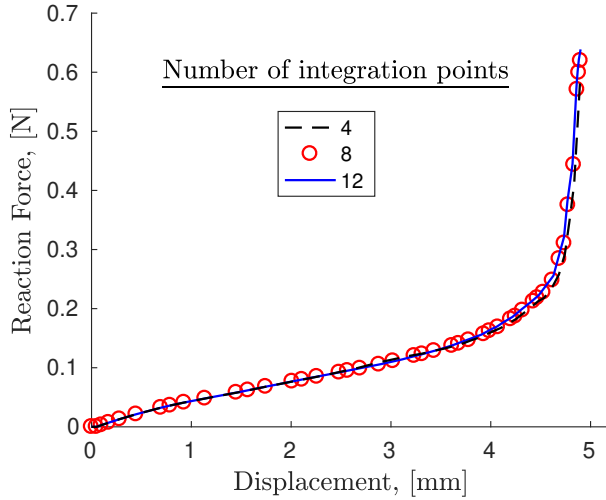


Figure 4: Influence of the number of integration points through the thickness with 384 elements in the in-plane mesh.

With the out-of-plane refinement being kept fixed, the mesh density for the in-plane directions of the paperboard is gradually increased to study the convergence between the C3D8 continuum element and the Q1STs shell-element. The initial finite element mesh is illustrated in Fig. 3b and it consists of eight elements along the cylinder axis combined with twelve elements around the curvature. A reference solution is obtained with a highly dense mesh of C3D8 continuum elements where the in-plane mesh is 4096 times the original mesh (roughly two million elements). When analyzing a simulation, the reaction force at the clamp is plotted against its vertical displacement and the result is compared to the reference solution as illustrated in Fig. 5. The difference in displacement  $\Delta u$  is recorded at four different load levels together with the difference in force magnitude  $\Delta F_{max}$  at the final state of deformation. The results from the in-plane mesh study, for both element types, are presented in Table 1. It clearly shows that the Q1STs solid-shell element performs better than the C3D8 continuum element in this particular case. For instance, the Q1STs element with 16 times the original mesh density will produce a more accurate solution than the C3D8 element with 256 times the original in-plane mesh. The difference in accuracy between the elements is also observed in Figs. 5 and 6 where the same in-plane mesh density, 16-times the initial mesh, is used and compared to the reference solution.

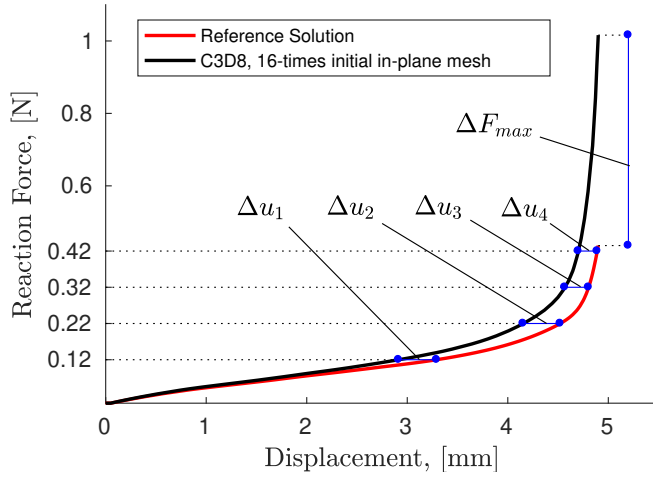


Figure 5: Force displacement curve using C3D8 continuum elements with 16-times the initial mesh. The difference in displacement between the simulation (Black) and the reference solution (Red) is recorded at four different load levels,  $\Delta u_1$ ,  $\Delta u_2$ ,  $\Delta u_3$  and  $\Delta u_4$ . The difference in force  $\Delta F_{max}$  at the final state of deformation is also recorded.

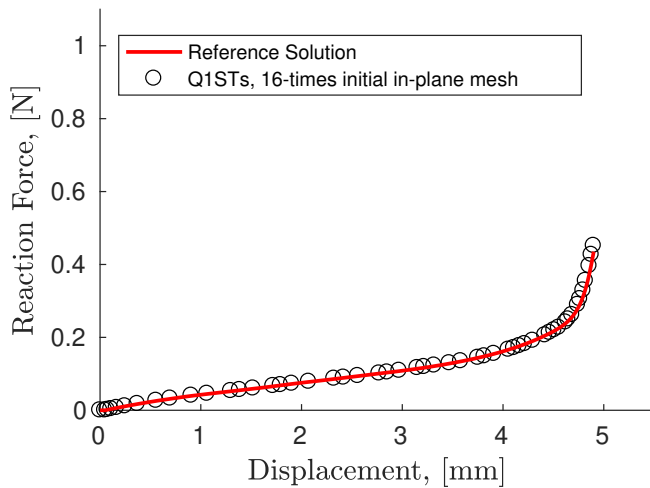


Figure 6: Force displacement results using the Q1STs solid-shell element with 16-times the original mesh. The simulation (Black) is compared with the reference solution (Red).

Element	multiple of initial in-plane mesh	$\Delta u_1$ Rel error [%]	$\Delta u_2$ Rel error [%]	$\Delta u_3$ Rel error [%]	$\Delta u_4$ Rel error [%]	$\Delta F_{max}$ Rel error [%]
Q1STs	1	2.79	3.65	4.72	5.62	33.4
	4	1.93	0.951	1.28	1.57	42.4
	16	1.57	0.276	0.408	0.329	3.72
	64	1.28	0.124	0.016	0.190	3.32
	256	1.17	0.019	0.021	0.039	1.67
C3D8	1	58.1	36.9	23.9	17.5	2055
	4	28.4	16.2	9.55	7.37	841
	16	11.5	8.16	4.91	3.84	134
	64	3.82	4.20	2.62	2.19	57
	256	1.02	1.76	1.20	1.07	24

Table 1: Refining the in-plane mesh density for the C3D8 continuum and Q1STs solid-shell element. Measurements are compared with the reference solution as shown in Fig. 5 and the relative (Rel) error is presented.

## 5 Large-Scale Forming of Paperboard

To illustrate the potential of the approach we consider a complex, industrial, large-scale forming example in which paperboard is converted into a package. The procedure is outlined in Fig. 7 where the bottom side of the cylindrical boundary of the paperboard is constrained to move along the horizontal direction while the top boundary is subjected to web-tension which is modeled as a surface pressure equal to 0.5 MPa together with a constrained radial displacement. The paperboard cylinder is formed while containing water and, for this purpose, an internal surface pressure due to the water is introduced, having the magnitude equal to 0.01 MPa. The machine direction MD for the paperboard is aligned with the length direction of the cylinder. The forming is initiated by compressing the paperboard with two rigid inductors, resulting in the deformed state illustrated in Fig. 7b. The compression step is followed by a rotating motion of two rigid flaps which will fold the edges of the compressed paperboard as shown in Figs. 7b and 7c.

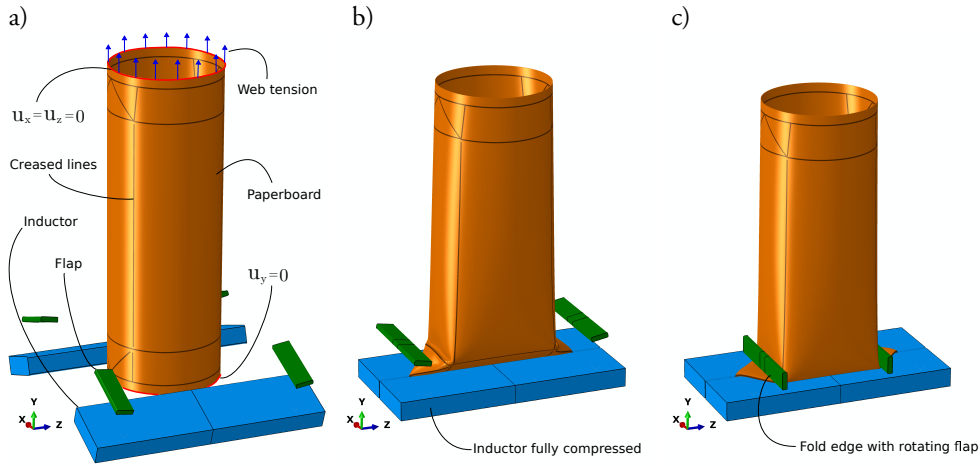


Figure 7: Large-scale forming example of paperboard. a) Undeformed configuration with all components. b) Compressed state from the displacements of the inductors. The flaps are starting to rotate around the x-axis. c) Final state of deformation caused by the rotation of the flaps.

Due to symmetry of the problem, only one fourth of the geometry is considered, as illustrated in Fig. 8, where the corresponding boundary conditions are introduced and the paperboard dimensions are presented. Creased lines, where the bending stiffness has been mechanically reduced by compression, are introduced along the paperboard in order to improve performance during folding. The creases, shown in Fig. 8, have a width equal to  $1\text{ mm}$  and are modeled by a reduction of the material parameters associated with the plasticity. The reduction of the material parameters are estimated using experimental data from line-creasing followed by subsequent line-folding. From this procedure, the creased elements are modeled by a 40% reduction of the initial yield limits for compression and tension along the MD direction, while the corresponding limits in CD direction is reduced by 10% for both compression and tension. Furthermore, ideal plasticity is adopted for both in-plane tension and compression. The problem is solved by means of the explicit dynamic finite element method in which the paperboard is discretized into 20560 elements with a representative, in-plane, element size of  $1\text{ mm}$ . The paperboard is  $0.4\text{ mm}$  thick and a single Q1STs element is used throughout the thickness of the model together with eight integration points. The solid tools are discretized using brick elements with reduced integration; 6050 elements were used for the flap and 10400 elements for the clamp. The solid tools are modeled to be isotropic with a module of elasticity  $E = 120\text{ GPa}$  and a Poissons ratio  $\nu = 0.3$ . Frictionless contact is enforced for the entire model using the penalty method with normal contact and pressure overclosure. To model self contact along the symmetry plane, the rigid plane in Fig. 8 is introduced in the model. The density of the paperboard is  $\rho = 788\text{ kg/m}^3$  which, together with mass-scaling, results in a stable time-step estimate of  $\Delta t = 407\text{ ns}$ . The time duration for the entire process is modeled to be  $0.2\text{ s}$  where the initial  $0.1\text{ s}$  is the time duration for the compression of the inductors while the final  $0.1\text{ s}$  is the time duration for the rotation of the flaps.

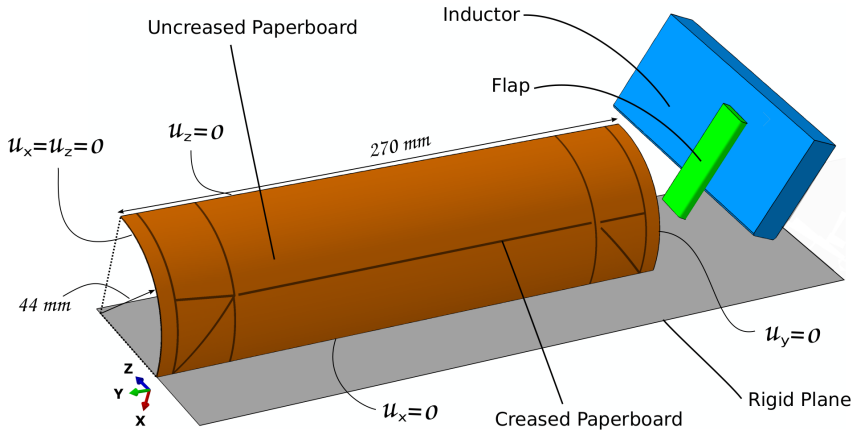


Figure 8: Schematics of the symmetric configuration corresponding to Fig. 7.

In Fig. 9, the deformation is captured at three snapshots in order to illustrate the deformation history. For the first snapshot in Fig. 9a, the displacements of the inductors results in an induced buckling close to the creased lines. The buckling will continue to propagate until the clamps are fully displaced, resulting in the deformed state shown in Fig. 9b, where the corners of the package are ready to be folded by the rotating motions of the flaps. The final deformation, from the rotational folding of the flaps, is demonstrated in Fig. 9c.

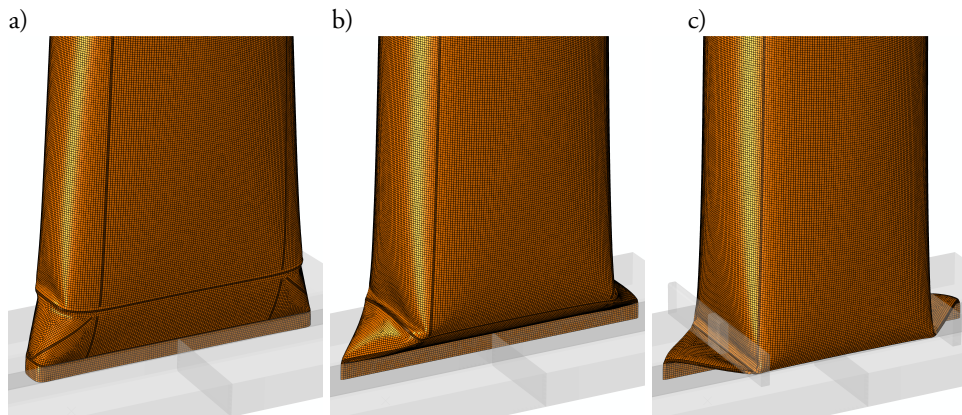


Figure 9: Snapshots of the deformation history. a) Initial state of buckling produced by the compression. b) The paperboard cylinder is fully compressed by the inductors. c) Final state of deformation after the rotation of the flaps.

The stress distribution at the final state of deformation is illustrated in Fig. 10 where the Kirchhoff stress tensor is projected along the current MD and CD directions, respectively. The magnitude of

the stress along the MD direction is higher than the corresponding CD projection. Furthermore, the magnitude of the MD and CD tensile stresses is in general higher than the compressive stress. Finally, both the MD and CD projected stress have a region of high stresses at the corner of the folded paperboard.

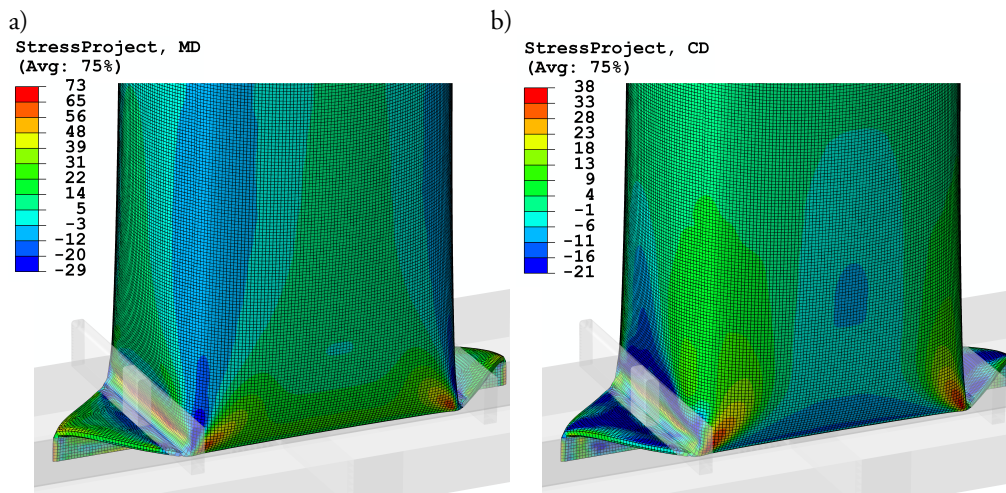


Figure 10: Distribution of the Kirchhoff stress tensor projected on to the material directions for the final state of deformation. a) MD projected stress in MPa. b) CD projected stress in MPa.

The stress distributions are of significant interest since it can be utilized to identify critical regions during the forming process. For instance, the occurrence of buckling is correlated to the distribution of compressive stresses in the material while the formations of wrinkles in the package can be predicted by studying regions in which the compressive stresses are highly localized. Furthermore, regions with high magnitudes of localized stress can be potential risk zones for crack nucleation to occur during the converting process.

## 6 Conclusions

An approach for modeling the forming process of paperboard at large-scales has been presented where an advanced 3D continuum model for paperboard has been utilized together with a solid-shell finite element concept. It has previously been observed that an advanced 3D continuum model is needed to fully capture the behavior of paperboard while use of a finite shell element is required to make large-scale forming simulations feasible with respect to computational time. The implementation was based on a solid-shell finite element formulation where the advantage of the full 3D material model was taken into account.

Numerical examples have been utilized to investigate the performance of the new approach where results using the solid-shell elements were compared with results obtained for fully integrated continuum elements. The conclusion is that the new approach, for the examples herein, is both stable and

more efficient compared to the fully integrated continuum element. A large-scale forming process was modeled, as a proof of concept, to highlight the potential application of the new approach. Future work includes detailed modeling of the creases and to include damage in the continuum framework such that failure during folding of paperboard can be captured. Furthermore, significant time savings are expected with the method of selective mass scaling which is to be considered in the future.

## Appendix A Material Parameters

The material parameters for the paperboard model are outlined in the following section. The elastic parameters  $A_i$ , defined in Eq. (14) for Helmholtz free energy, is presented in Tab. 2. The coefficients defining the yield normals  $N_{ij}^{(\nu)}$ , corresponding to Eq. (17), are tabulated in Tab. 3 along with the physical interpretation of each subsurface  $\nu$ . Presented in Tab. 4 is the initial distance to each subsurface,  $K_0^{(\nu)}$ , together with the hardening parameters,  $a_\nu$  and  $b_\nu$ .

Elastic parameters	Value
$A_1$	1690 (Mpa)
$A_2$	292 (Mpa)
$A_3$	28.4 (Mpa)
$A_4$	1333 (Mpa)
$A_5$	78.0 (Mpa)
$A_6$	0.365 (Mpa)
$A_7$	11.5 (-)

Table 2: Elastic parameters.

Stress state	Subsurface, $\nu$	Subsurface components $N_{ij}^{(\nu)}$ (-)
MD tension	1	$N_{11}^{(1)} = 0.925, N_{22}^{(1)} = -0.379$
CD tension	2	$N_{11}^{(2)} = -0.215, N_{22}^{(2)} = 0.977$
MD-CD shear	3	$N_{12}^{(3)} = 0.7071, N_{21}^{(3)} = 0.7071$
MD compression	4	$N_{11}^{(4)} = -1$
CD compression	5	$N_{22}^{(5)} = -1$
MD-CD shear	6	$N_{12}^{(6)} = -0.7071, N_{21}^{(6)} = -0.7071$
ZD compression	7	$N_{33}^{(7)} = -1$
ZD tension	8	$N_{33}^{(8)} = 1$
MD-ZD shear	9	$N_{33}^{(9)} = 0.704, N_{13}^{(9)} = 0.503$
MD-ZD shear	10	$N_{33}^{(10)} = 0.704, N_{13}^{(10)} = -0.503$
CD-ZD shear	11	$N_{33}^{(11)} = 0.704, N_{23}^{(11)} = 0.503$
CD-ZD shear	12	$N_{33}^{(12)} = 0.704, N_{23}^{(12)} = -0.503$

Table 3: Components  $N_{ij}^{(\nu)}$  defining the normals of each subsurface.

Subsurface	Initial yield	Hardening	Hardening
$\nu$	$K_0^{(\nu)}$ (MPa)	$a_\nu$ (MPa)	$b_\nu$ (-)
1	20.4	12.2	690
2	11.7	5.10	435
3	9.91	6.63	334
4	29.1	–	–
5	21.0	–	–
6	9.91	6.63	435
7	1.00	49	–
8	0.40	–	–
9	2.51	–	–
10	2.51	–	–
11	2.51	–	–
12	2.51	–	–

Table 4: Hardening parameters  $a_\nu$ ,  $b_\nu$  and the initial distance to each subsurface  $K_0^{(\nu)}$ .

## References

- [1] A. Beex and J. Peerlings. On the influence of delamination on laminated paperboard creasing and folding. *Philosophical Transactions of the Royal Society*, 370:1912–1924, 2011.
- [2] L. Beex and R. Peerlings. An experimental and computational study of laminated paperboard creasing and folding. *International Journal of Solids and Structures*, 46:4192–4207, 2009.
- [3] L. Beex, R. Peerlings, and M. Geers. A multiscale quasicontinuum method for dissipative lattice models and discrete networks. *Journal of the Mechanics and Physics of Solids*, 64:154–169, 2014.
- [4] T. Belytschko and J. Lin. Explicit algorithms for the nonlinear dynamics of shells. *Computer Methods in Applied Mechanics and Engineering*, 42:225–251, 1984.
- [5] E. Borgqvist, T. Lindström, J. Tryding, M. Wallin, and M. Ristinmaa. Distortional hardening plasticity model for paperboard. *International Journal of Solids and Structures*, 51:2411–2423, 2014.
- [6] E. Borgqvist, M. Wallin, M. Ristinmaa, and J. Tryding. An anisotropic in-plane and out-of-plane elasto-plastic continuum model for paperboard. *Composite Structures*, 126:184–195, 2015.
- [7] E. Borgqvist, M. Wallin, J. Tryding, M. Ristinmaa, and E. Tudisco. Localized deformation in compression and folding of paperboard. *Packaging Technology and Science*, 29:397–414, 2016.
- [8] E. Bosco, R. Peerlings, and M. Geers. Predicting hygro-elastic properties of paper sheets based on idealized model of the underlying fibrous network. *International Journal of Solids and Structures*, 56-57:43–52, 2015.
- [9] G. Cocchetti, M. Pagani, and U. Perego. Selective mass scaling and critical time-step estimate for explicit dynamics analyses with solid-shell elements. *Computers and Structures*, 127:39–52, 2013.

- [10] B. Coleman and W. Noll. The thermodynamics of elastic materials with heat conduction and viscosity. *Archive for Rational Mechanics and Analysis*, 13:167–178, 1963.
- [11] Dassault Systems. *Abaqus 6.13 analysis user's manual*.
- [12] A. Giampieri, U. Perego, and R. Borsari. A constitutive model for the mechanical response of the folding of creased paperboard. *International Journal of Solids and Structures*, 48:2275–2287, 2011.
- [13] A. Harrysson and M. Ristinmaa. Large strain elasto-plastic model of paper and corrugated board. *International Journal of Solids and Structures*, 45:3334–3352, 2008.
- [14] H. Huang, A. Hagman, and M. Nygård. Quasi static analysis of creasing and folding for three paperboards. *Mechanics of Materials*, 69:11–34, 2014.
- [15] T.J.R. Hughes and T. Tezduyar. Finite elements based upon mindlin plate theory with particular reference to the four-node bilinear isoparametric element. *Journal of Applied Mechanics*, 48:587–596, 1981.
- [16] A. Kulachenko and T. Uesaka. Direct simulations of fiber network deformation and failure. *Mechanics of Materials*, 51:1–14, 2012.
- [17] Y. Li, S. Stapleton, S. Reese, and J. Simon. Anisotropic elastic-plastic deformation of paper: In-plane model. *International Journal of Solids and Structures*, 100-101:286–296, 2016.
- [18] S. Nagasawa, Y. Fukuzawa, T. Yamaguchi, S. Tsukatani, and I. Katayama. Effect of crease depth and crease deviation on folding deformation characteristics of coated paperboard. *Journal of Materials Processing Technology*, 140:157–162, 2003.
- [19] M. Ortiz and P. Popov. Accuracy and stability of integration algorithms for elastoplastic constitutive relations. *International Journal for Numerical Methods in Engineering*, 21:1551–1576, 1985.
- [20] M. Pagani and U. Perego. Explicit dynamics simulation of blade cutting of thin elastoplastic shells using ”directional” cohesive elements in solid-shell finite element models. *Computer Methods in Applied Mechanics and Engineering*, 285:515–541, 2015.
- [21] M. Pagani, S. Reese, and U. Perego. Computationally efficient explicit nonlinear analyses using reduced integration-based solid-shell finite elements. *Computer Methods in Applied Mechanics and Engineering*, 268:141–159, 2013.
- [22] M. Schwarze and S. Reese. A reduced integration solid-shell element based on the EAS and the ANS concept – Geometrically linear problems. *International Journal for Numerical Methods in Engineering*, 80:1322–1355, 2009.
- [23] M. Schwarze and S. Reese. A reduced integration solid-shell finite element based on the EAS and the ANS concept – Large deformation problems. *International Journal for Numerical Methods in Engineering*, 85:289–329, 2010.

- [24] M. Schwarze, I. Vladimirov, and S. Reese. Sheet metal forming and springback simulation by means of a new reduced integration solid-shell finite element technology. *Computer Methods in Applied Mechanics and Engineering*, 200:454–476, 2011.
- [25] J. Simo, F. Armero, and R. Taylor. Geometrically non-linear enhanced strain mixed methods and the method of incompatible modes. *Computer Methods in Applied Mechanics and Engineering*, 33:1413–1449, 1992.
- [26] J. Simo, F. Armero, and R. Taylor. Improved version of assumed enhanced strain tri-linear elements for 3d finite deformation problems. *Computer Methods in Applied Mechanics and Engineering*, 110:359–386, 1993.
- [27] J. Sliseris, H. Andrä, M. Kabel, B. Dix, B. Plinke, O. Wirjadi, and G. Frolovs. Numerical prediction of the stiffness and strength of medium density fiberboards. *Mechanics of Materials*, 79:73–84, 2014.
- [28] D. Tjahjanto, O. Girlanda, and S. Östlund. Anisotropic viscoelastic-viscoplastic continuum model for high-density cellulose-based materials. *Journal of Mechanics and Physics of Solids*, 84:1–20, 2015.
- [29] I. Vladimirov, M. Pietryga, and S. Reese. On the influence of kinematic hardening on plastic anisotropy in the context of finite strain plasticity. *International Journal of Material Forming*, 4:255–267, 2011.
- [30] D. Wilbrink, L. Beex, and R. Peerlings. A discrete network model for bond failure and frictional sliding in fibrous materials. *International Journal of Solids and Structures*, 50:1354–1363, 2013.
- [31] Q. Xia. *Mechanics of inelastic deformation and delamination in paperboard*. PhD thesis, Massachusetts Institute of Technology, 2002.
- [32] Q. Xia, M. Boyce, and D. Parks. A constitutive model for the anisotropic elastic-plastic deformation of paper and paperboard. *International Journal of Solids and Structures*, 39:4053–4071, 2004.



## Paper B

Kristofer Robertsson, Mathias Wallin, Eric Borgqvist,  
Matti Ristinmaa and Johan Tryding

*A rate-dependent continuum model for rapid  
converting of paperboard*

Applied Mathematical Modelling 99 (2021), 497-513



# A rate-dependent continuum model for rapid converting of paperboard

Kristofer Robertsson<sup>1</sup>, Mathias Wallin<sup>1</sup>, Eric Borgqvist<sup>2</sup>,  
Matti Ristinmaa<sup>1</sup> and Johan Tryding<sup>1,2</sup>

<sup>1</sup>Division of Solid Mechanics, Lund University, P.O Box 118, 221 00, Sweden

<sup>2</sup>Tetra Pak Packaging Solutions, Lund, 221 86, Sweden

## Abstract

A rate-dependent continuum model for paperboard is developed within a framework for finite strains and finite deformations. A multiplicative split of the deformation gradient into an elastic and an inelastic part is assumed. For the in-plane modes of deformation, viscoelasticity is introduced via a thermodynamically consistent generalization of the Maxwell formulation. The elastic transition between out-of-plane compression and out-of-plane tension is smooth, excluding the need for a switch function which is present in a number of existing paperboard models. The evolution of the inelastic part is modeled using two potential functions separating compression from shear and tension. To calibrate the material model, a set of experiments at different loading rates have been performed on single ply paperboard together with creep and relaxation tests for in-plane uniaxial tension. The model is validated by simulating two loading cases related to package forming, line-folding followed by subsequent force-relaxation and line-creasing during different operating velocities in conjunction with a creep study.

# 1 Introduction

Cellulose-based paperboard is a thin lightweight material with a large degree of anisotropy between the in-plane and out-of-plane properties while high bending stiffness makes it a suitable material for packaging containers. The anisotropy stems from the manufacturing process where fibers are continuously sprayed along the manufacturing direction, i.e. the Machine Direction MD. The transverse direction to MD is denoted CD and together they are considered the in-plane dimension of the board. Perpendicular to the in-plane dimension is the out-of-plane stacking direction for the fibers, denoted ZD. The elastic modulus in MD is typically 2-3 orders of magnitude higher than CD and approximately 100 times the magnitude of ZD.

Modeling of paperboard is an active research field and there exists a number of different modeling strategies, cf. the overview in Simon [1]. To tailor the manufacturing process of paperboard, micro-scale models are useful tools, cf. e.g. Kulachenko and Uesaka [2] where beam elements were used to represent individual fibers together with a model for dynamic bonding between the fibers. Similar micromechanical models can be found in Wilbrink et al. [3], Beex et al. [4] and Sliseris et al. [5]. For large scale industrial simulations of e.g. package forming, other computationally efficient macro-scale modeling strategies are needed. Broadly speaking two types of macro-scale strategies exist. The first strategy is based on combining cohesive elements with a simplified continuum model. In this approach the critical delamination zones are predefined by the user and models within this category includes Huang et al. [6], [7], Beex et al. [8] and Nygård et al. [9]. However, the simplified material description in such models limits the possibility to accurately capture the material response during out-of-plane compression. In the second macro-scale approach, the description of the continuum is more advanced, taking into account the non-linear kinematics and large strains associated with the out-of-plane direction. Examples of such models, which are also thermodynamically consistent, includes the work by Harrysson et al. [10], Li et al. [11], [12] and Borgqvist et al. [13].

The models listed above are rate-independent, i.e. they will therefore predict the same material response regardless of how fast they are loaded. Experiments, cf. Nagasawa et al. [14], Gunderson et al. [15] and Alftan [16] show, however, that paperboard is a rate-dependent, viscous, material in which both creep and relaxation is present. The rate-dependent behavior of paperboard is of importance for many industrial processes where the operating speed, due to efficiency, is maximized. In addition, the viscous creep and relaxation behavior is of importance in order to predict the material response over longer periods of time. Rate-dependent models for cellulose based fibrous materials with the aim to capture specific aspects do exist. Lif et al. [17] developed a constitutive hydro-viscoelastic model specifically designed for rate-dependent moisture and creep interactions. Strömbro et al. [18] and Bosco et al. [19] proposed a network and meso-scale model, respectively, with similar aims. However, to the authors knowledge, no comprehensive model taking into account the full characteristics of paperboard together with rate-effects exist. The closest related work is the model by Tjahjanto et al. [20] which is developed for pressboard, a comparably thick fibrous structure.

In this article, a rate-dependent paperboard model, suitable for large scale industrial applications, is developed by taking advantage of the rate-independent framework of Borgqvist et al. [13]. The thermodynamically consistent model by Borgqvist is derived for large strains using the yield surface proposed by Xia et al. [21] which is able to model the complex anisotropic hardening behavior observed in paperboard, a feature that a conventional Hill model is too restrictive to fully capture,

cf. Borgqvist et al. [22]. The model by Borgqvist was utilized in [13] to simulate the creasing process using a simplified line-creasing operation as well as a more realistic, 3D rotational setup. In addition, as shown in Borgqvist et al. [23], the model is able to capture the formation of wrinkles during the line-folding process of uncreased paperboard and predict the instability that exists in the short-span compression test. Recently, in Robertsson et al. [24], the Borgqvist model was used in a large-scale forming simulation of paperboard where the model was combined with an efficient solid-shell element by Schwarze et al. [25].

Apart from the inclusion of viscous effects, the model in this work removes the unphysical discontinuity in transition between out-of-plane compression and tension that is present in several of its predecessors, cf. Borgqvist et al. [13], [23], Harrysson et al. [26] and Nygård et al. [9]. In the aforementioned models, the out-of-plane elastic compression and tension are separated by a switch function which is in contradiction with the observations in Persson [27] where a smooth transition between out-of-plane compression and tension was observed.

The present paper is structured as follows. In section 2, the modeling framework is presented while section 3 is dedicated to numerical considerations. In section 4, uniaxial modes of deformations are considered, and the viscosity parameters are calibrated using relaxation and creep tests for uniaxial tension. In addition, the rate-dependency related to inelastic deformation is also taken into account and the model behavior during out-of-plane compression is highlighted. In section 5 and 6, the model is validated against measurement from two typical loading cases related to package forming, the line-creasing procedure, during different operating velocities along with a creep study, and the line-folding sequence followed by subsequent force-relaxation.

## 2 Constitutive framework

The viscous characteristics observed for paperboard during out-of-plane compression are very low compared to the behavior during in-plane uniaxial tension. The experimentally observed behavior can be linked to the different in-plane and out-of-plane deformation mechanisms in which the in-plane deformation is governed by longitudinal deformation of fibers and fiber slipping, whereas the out-of-plane deformation is governed by the deformation of fiber cross sections. As such, it is natural to additively separate the elastic energy into one in-plane part and one out-of-plane part. To accordingly capture the complex rate-dependent behavior, the in-plane part of the stress tensor is enhanced with a viscous contribution which is based on a, thermodynamically consistent, large strains and anisotropic generalization of the viscoelastic Maxwell model.

There is evidence for the inelastic features of paperboard being mainly governed by the deformation of the fibers and not the bonding strength, cf. Bordulina et al. [28]. To model the inelastic behavior, a multiplicative split of the deformation gradient is assumed. Experimental evidence reveals that the rate-dependent effects are minor during out-of-plane compression, whereas the rate-dependency is significant during tension and out-of-plane shear. For this purpose, two potential functions, which separate compression from tension and shear, are postulated. With the proposed separation of the potential functions, the rate dependency during out-of-plane compression can be controlled and modeled in accordance with experiments while being able to capture the rate-dependent behavior during tension and shear.

Apart from the viscous effects, the framework is based on the previously successful model by Borgqvist et al. [13] which excludes damage, temperature and moisture effects. In the kinematic description, we assume the in-plane directions, MD and CD, to follow the elastic part of the deformation gradient while the out-of-plane direction, ZD, is always perpendicular to MD and CD.

## 2.1 Modeling base

To separate elasticity from inelastic deformation, a multiplicative split of the deformation gradient is assumed,  $\mathbf{F} = \mathbf{F}^e \mathbf{F}^{ie}$  where  $\mathbf{F}^e$  is the reversible elastic part and  $\mathbf{F}^{ie}$  the permanent inelastic contribution, cf. Kröner [29]. The intermediate configuration is not unique, e.g. Dafalias [30], and taken to be isoclinic as introduced in Mandel [31]. To include viscoelasticity, we consider the dissipation inequality under isothermal conditions which in the material configuration is stated as, see for instance Truesdell and Noll [32],

$$D = \frac{1}{2} \mathbf{S} : \dot{\mathbf{C}} - \rho_0 \dot{\Psi} \geq 0, \quad (1)$$

where  $\mathbf{S}$  is the second Piola-Kirchhoff stress tensor and  $\mathbf{C} = \mathbf{F}^t \mathbf{F}$  is the right Cauchy-Green deformation tensor while  $\rho_0$  is the mass density in the reference configuration and  $\Psi$  being the Helmholtz free energy per unit mass. Furthermore, to model anisotropy, the elastic deformation tensor  $\mathbf{C}^e = \mathbf{F}^{et} \mathbf{F}^e$  is introduced together with three structural tensors,

$$\mathbf{M}_0^{(i)} = \mathbf{v}_0^{(i)} \otimes \mathbf{v}_0^{(i)} \quad \text{with} \quad i = 1, 2, 3, \quad (2)$$

where  $\mathbf{v}_0^{(1)}$  and  $\mathbf{v}_0^{(2)}$  are director vectors in the reference configuration aligned with the two in-plane characteristic directions of paperboard, i.e. the machine (MD) and the cross (CD) direction while  $\mathbf{v}_0^{(3)}$  corresponds to the out-of-plane (ZD) direction perpendicular to  $\mathbf{v}_0^{(1)}$  and  $\mathbf{v}_0^{(2)}$ . The free energy  $\Psi$  is assumed to be additively separable, excluding coupling effect such that,

$$\Psi = \Psi_{oop}^e \left( \mathbf{C}^e, \mathbf{M}_0^{(i)} \right) + \Psi_{ip}^e \left( \mathbf{C}^e, \mathbf{M}_0^{(i)} \right) + \sum_{\alpha} \Upsilon_{\alpha} \left( \mathbf{C}^e, \mathbf{M}_0^{(i)}, \Gamma_{\alpha} \right) + \Psi^{ie} \left( \kappa^{(\nu)} \right), \quad (3)$$

with  $\Psi_{oop}^e$  and  $\Psi_{ip}^e$  being the elastic contribution from the out-of-plane deformation and the in-plane deformation, respectively, while  $\Psi^{ie}$  is the energy associated with the inelastic contribution along with the internal hardening variables  $\kappa^{(\nu)}$ . The viscoelastic contribution consists of multiple rheological networks  $\alpha$ , each associated with a configurational energy  $\Upsilon_{\alpha}$  and an internal second order tensor  $\Gamma_{\alpha}$ . Using (3) and the chain rule, the dissipation inequality in (1) is reformulated as,

$$D = \frac{1}{2} \left( \bar{\mathbf{S}} - 2\rho_0 \frac{\partial \Psi}{\partial \mathbf{C}^e} \right) : \dot{\mathbf{C}}^e + D^{ie} + \sum_{\alpha} D_{\alpha}^{ve} \geq 0, \quad (4)$$

where the second Piola-Kirchhoff stress tensor in the intermediate configuration was introduced as  $\bar{\mathbf{S}} = \mathbf{F}^{ie} \mathbf{S} \mathbf{F}^{iet}$  and  $D^{ie}$  being the inelastic contribution to the dissipation.

The viscoelastic dissipation from the network  $\alpha$  is identified as,

$$D_{\alpha}^{ve} = \mathbf{Q}_{\alpha} : \dot{\Gamma}_{\alpha} \geq 0 \quad \text{with} \quad \mathbf{Q}_{\alpha} = -\rho_0 \frac{\partial \Upsilon_{\alpha}}{\partial \Gamma_{\alpha}}, \quad (5)$$

where  $\mathbf{Q}_\alpha$  is the conjugated variable to  $\mathbf{\Gamma}_\alpha$ . To fulfill the dissipation inequality (4), we require that the viscoelastic contribution,  $D_\alpha^{ve}$ , to the dissipation is non-negative. This requirement is fulfilled by the following evolution law,

$$\mathbb{C}_0 : \dot{\mathbf{\Gamma}}_\alpha = \frac{1}{\eta_\alpha} \mathbf{Q}_\alpha \quad \text{with} \quad \mathbb{C}_0 = 4 \rho_0 \left. \frac{\partial^2 \Psi_{ip}^e}{\partial \mathbf{C}^e \otimes \partial \mathbf{C}^e} \right|_{\mathbf{C}^e = \mathbf{I}}, \quad (6)$$

where  $\eta_\alpha$  is a viscosity parameter. As seen in (6), the fourth order tensor  $\mathbb{C}_0$  is, for simplicity, taken as the initial material tangent corresponding to the in-plane part of the elastic energy, i.e. viscoelasticity only influence the in-plane deformation as described previously. In addition, we assume that  $\mathbb{C}_0$  is positive definite which implies  $D_\alpha^{ve} \geq 0$ .

Using the arguments by Coleman and Gurtin [33] in conjunction with the dissipation inequality (4) and the specific energy in (3), the second Piola-Kirchhoff stress in the intermediate configuration is obtained as,

$$\bar{\mathbf{S}} = 2\rho_0 \frac{\partial \Psi_{oop}^e}{\partial \mathbf{C}^e} + 2\rho_0 \frac{\partial \Psi_{ip}^e}{\partial \mathbf{C}^e} + \sum_\alpha 2\rho_0 \frac{\partial \Upsilon_\alpha}{\partial \mathbf{C}^e}. \quad (7)$$

We restrict the configurational energy  $\Upsilon_\alpha$  to fulfill,

$$\mathbf{Q}_\alpha = 2\rho_0 \frac{\partial \Upsilon_\alpha}{\partial \mathbf{C}^e}, \quad (8)$$

such that a push-forward transformation of (7) results in,

$$\boldsymbol{\tau} = \boldsymbol{\tau}_{oop} + \boldsymbol{\tau}_{ip}^\infty + \sum_\alpha \mathbf{F}^e \mathbf{Q}_\alpha \mathbf{F}^{et} \quad \text{with} \quad \begin{cases} \boldsymbol{\tau}_{oop} = 2\rho_0 \mathbf{F}^e \frac{\partial \Psi_{oop}^e}{\partial \mathbf{C}^e} \mathbf{F}^{et} \\ \boldsymbol{\tau}_{ip}^\infty = 2\rho_0 \mathbf{F}^e \frac{\partial \Psi_{ip}^e}{\partial \mathbf{C}^e} \mathbf{F}^{et} \end{cases}, \quad (9)$$

where  $\boldsymbol{\tau}$  is the Kirchhoff stress tensor which will be utilized later on.

A format  $\Upsilon_\alpha$  that fulfills (8) and (5) is,

$$\Upsilon_\alpha = \frac{\eta_\alpha}{8T_\alpha} (2\mathbf{\Gamma}_\alpha - \mathbf{C}^e) : \mathbb{C}_0 : (2\mathbf{\Gamma}_\alpha - \mathbf{C}^e), \quad (10)$$

with  $T_\alpha$  being the relaxation time associated with network  $\alpha$ . The reader is referred to Appendix C for the derivation of (10). With the configurational energy (10), the viscoelastic stress is obtained from (8) as,

$$\mathbf{Q}_\alpha = \frac{\eta_\alpha}{2T_\alpha} \mathbb{C}_0 : (\mathbf{C}^e - 2\mathbf{\Gamma}_\alpha), \quad (11)$$

and subsequently the evolution law in (6) results in,

$$\dot{\mathbf{\Gamma}}_\alpha + \frac{1}{T_\alpha} \mathbf{\Gamma}_\alpha = \frac{1}{2T_\alpha} \mathbf{C}^e. \quad (12)$$

The remaining inelastic part of the dissipation in (4) is identified as,

$$D^{ie} = \frac{1}{2} \mathbf{S} : \frac{\partial \mathbf{C}}{\partial \mathbf{F}^{ie}} : \dot{\mathbf{F}}^{ie} - \sum_\nu \rho_0 \frac{\partial \Psi^{ie}}{\partial k^{(\nu)}} \dot{k}^{(\nu)} \geq 0. \quad (13)$$

Taking advantage of the inelastic velocity gradient, cf. Borgqvist et al. [13], defined as,

$$\mathbf{l}^{ie} = \mathbf{F}^e \dot{\mathbf{F}}^{ie} (\mathbf{F}^{ie})^{-1} (\mathbf{F}^e)^{-1}, \quad (14)$$

the dissipation in (13) can be written as,

$$\boldsymbol{\tau} : \mathbf{d}^{ie} - \sum_{\nu} K^{(\nu)} \dot{\kappa}^{(\nu)} \geq 0 \quad (15)$$

where it was used that the Kirchhoff stress tensor is symmetric and that  $\mathbf{d}^{ie}$  being the symmetric part of  $\mathbf{l}^{ie}$ . The conjugated force in (15) is defined as  $K^{(\nu)} = \rho_0 \frac{\partial \Psi^{ie}}{\partial \kappa^{(\nu)}}$ . The inequality in (15) will be utilized when postulating the evolution of  $\mathbf{d}^{ie}$  and  $\dot{\kappa}^{(\nu)}$ .

## 2.2 Specific energy

The mapping of the in-plane director vectors from the reference to the spatial configuration are postulated to follow the elastic part of the deformation gradient, i.e.

$$\mathbf{v}^{(1)} = \mathbf{F}^e \mathbf{v}_0^{(1)} \quad \text{and} \quad \mathbf{v}^{(2)} = \mathbf{F}^e \mathbf{v}_0^{(2)}, \quad (16)$$

while the third ZD direction  $\mathbf{n}^{(3)}$  is modeled to always be perpendicular to the in-plane director vectors, i.e.

$$\mathbf{n}^{(3)} = \mathbf{v}^{(1)} \times \mathbf{v}^{(2)} = J^e \mathbf{F}^{e-T} \mathbf{v}_0^{(3)}, \quad (17)$$

with  $J^e = \det(\mathbf{F}^e)$  being the determinant of the elastic deformation gradient. The assumptions in (16) and (17) was first introduced in [13] and it ensures a decoupled response between the out-of-plane and in-plane response. Six invariants define the elastic part of the free energy and the first three are defined as,

$$I_{11} = \|\mathbf{v}^{(1)}\|, \quad I_{22} = \|\mathbf{v}^{(2)}\| \quad \text{and} \quad I_{33} = \mathbf{v}^{(3)} \cdot \frac{\mathbf{n}^{(3)}}{\|\mathbf{n}^{(3)}\|}, \quad (18)$$

with  $\mathbf{v}^{(3)} = \mathbf{F}^e \mathbf{v}_0^{(3)}$  being similar to the in-plane director vectors and  $\|\bullet\|$  is the Euclidean norm. The invariants  $I_{\alpha\alpha}$  represent stretch along the MD, CD and ZD directions, respectively. In contrast to [23], the invariant representing the stretch along ZD is defined as the projection of  $\mathbf{v}^{(3)}$  along the ZD-direction introduced in (17). The motivation for the invariant  $I_{33}$  is that it will not be effected by pure out-of-plane shearing, i.e.  $\mathbf{F}^e = \mathbf{I} + \gamma \mathbf{n}_0^{(3)} \otimes \mathbf{v}_0^{(1)}$ . The remaining three invariants associated with shear and volumetric deformation are defined as,

$$I_{12} = \|\mathbf{n}^{(3)}\|, \quad I_{13} = \|\mathbf{v}^{(3)}\| \quad \text{and} \quad J^e = \det(\mathbf{F}^e). \quad (19)$$

In summary, the six invariants can be expressed in terms of the material quantities,

$$\begin{aligned} I_{11} &= \sqrt{\mathbf{C}^e : \mathbf{M}_0^{(1)}}, \quad I_{22} = \sqrt{\mathbf{C}^e : \mathbf{M}_0^{(2)}}, \quad I_{33} = \frac{J^e}{I_{12}} \sqrt{\mathbf{I} : \mathbf{M}_0^{(3)}}, \\ I_{12} &= J^e \sqrt{\mathbf{C}^{e-1} : \mathbf{M}_0^{(3)}}, \quad I_{13} = \sqrt{\mathbf{C}^e : \mathbf{M}_0^{(3)}} \quad \text{and} \quad J^e = \sqrt{\det(\mathbf{C}^e)}, \end{aligned} \quad (20)$$

which is suitable for evaluating the stress contribution from equation (7) and (9). The elastic energy is assumed to have the following format,

$$\begin{cases} \rho_0 \Psi_{ip}^e = A_1(I_{11} + I_{11}^{-1} - 2) + A_2(I_{22} + I_{22}^{-1} - 2) + A_4(I_{11} + I_{22} + I_{12}^{-1} - 3) \\ \rho_0 \Psi_{oop}^e = A_5(I_{11}I_{22}I_{13} - J^e) + A_3(I_{33} + I_{33}^{-1} - 2) + \frac{A_6}{A_7} \left[ \frac{I_{33}^2 - 1}{2} - \ln(I_{33}) \right]^{A_7}, \end{cases} \quad (21)$$

where  $A_i$  are positive elastic parameters. The elastic energy  $\Psi_{ip}^e$  is identical to the one in [23], whereas the out-of-plane part  $\Psi_{oop}^e$  is modified such that the transition from tension and compression is smooth which removes the need for an unphysical switch function present in [23].

To simplify the presentation, the spatial structural tensors are introduced as,

$$\begin{cases} \mathbf{m}^{(1)} = \mathbf{v}^{(1)} \otimes \mathbf{v}^{(1)} = \mathbf{F}^e \mathbf{M}_0^{(1)} \mathbf{F}^{et} \\ \mathbf{m}^{(2)} = \mathbf{v}^{(2)} \otimes \mathbf{v}^{(2)} = \mathbf{F}^e \mathbf{M}_0^{(2)} \mathbf{F}^{et} \end{cases} \quad \text{and} \quad \mathbf{m}^{(3)} = \mathbf{n}^{(3)} \otimes \mathbf{n}^{(3)} = J^{e2} \mathbf{F}^{e-t} \mathbf{M}_0^{(3)} \mathbf{F}^{e-1}, \quad (22)$$

together with the elastic Finger tensor  $\mathbf{b}^e = \mathbf{F}^e \mathbf{F}^{et}$  such that a compact expression for the Kirchhoff stress tensor is obtained. Use of (9) and (20) together with the elastic energy (21) results in,

$$\begin{cases} \boldsymbol{\tau}_{oop} = P_1 \mathbf{m}^{(1)} + P_2 \mathbf{m}^{(2)} + P_3 \mathbf{m}^{(3)} + P_4 \mathbf{I} + P_5 \mathbf{b}^e \mathbf{m}^{(3)} \mathbf{b}^e \\ \boldsymbol{\tau}_{ip}^\infty = R_1 \mathbf{m}^{(1)} + R_2 \mathbf{m}^{(2)} + R_3 \mathbf{m}^{(3)} + R_4 \mathbf{I} \end{cases}, \quad (23)$$

where the scalar functions  $P_i$  and  $R_i$  are given in Appendix (39). The fourth order tensor  $\mathbb{C}_0$  defined in (6) is calculated with the proposed energy in (21) which leads to,

$$\begin{aligned} \mathbb{C}_0 = & 2(A_1 + A_4) (\mathbf{M}_0^{(1)} \otimes \mathbf{M}_0^{(1)}) + 2(A_2 + A_4) (\mathbf{M}_0^{(2)} \otimes \mathbf{M}_0^{(2)}) \\ & + A_4 (\mathbf{M}_0^{(1)} \otimes \mathbf{M}_0^{(2)} + \mathbf{M}_0^{(2)} \otimes \mathbf{M}_0^{(1)}) \\ & + A_4 (\mathbf{M}_0^{(1)} \otimes \mathbf{M}_0^{(2)} + \mathbf{M}_0^{(2)} \otimes \mathbf{M}_0^{(1)} + \mathbf{M}_0^{(1)} \bar{\otimes} \mathbf{M}_0^{(2)} + \mathbf{M}_0^{(2)} \bar{\otimes} \mathbf{M}_0^{(1)}) \end{aligned} \quad (24)$$

Since  $\mathbb{C}_0$  is positive definite, cf. Appendix D, the viscoelastic dissipation in (4) is fulfilled.

### 2.3 Inelastic potential functions

The evolution of the inelastic strains are derived from two potential functions,

$$\Phi_1 = \sum_{\nu=1, \nu \neq 4, 5, 7}^{12} \langle \Omega_\nu \rangle^{2k} \quad \text{and} \quad \Phi_2 = \sum_{\nu=4, 5, 7} \langle \Omega_\nu \rangle^{2k}, \quad (25)$$

with

$$\Omega_\nu = \frac{\boldsymbol{\tau} : \mathbf{n}_s^{(\nu)}}{\tau^{(\nu)}} \quad \text{and} \quad \langle (\bullet) \rangle = \begin{cases} (\bullet) & \text{if } (\bullet) > 0 \\ 0 & \text{otherwise} \end{cases}. \quad (26)$$

The potential functions consists of twelve parts  $\Omega_\nu$  corresponding to different loading directions defined by  $\mathbf{n}_s^{(\nu)}$ , cf. Fig. 1 for an interpretation of different  $\nu$ . As discussed previously, the use of two

potential functions allows the compression response in MD, CD and ZD, i.e.  $\nu = [4, 5, 7]$ , to be modeled separately from shear and tension.

The positive exponent  $k$  in (25) is chosen as  $k = 3$ . In each direction, the projection of  $\boldsymbol{\tau}$  is normalized by the following normalization factor,

$$\tau^{(\nu)} = \tau_0^{(\nu)} + K^{(\nu)} \quad \text{with} \quad K^{(\nu)} = \begin{cases} a_\nu \ln(b_\nu \kappa^{(\nu)} + 1) + c_\nu \kappa^{(\nu)}, & \nu \neq \{4, 5\} \\ a_\nu \tanh(b_\nu \kappa^{(\nu)}), & \nu = \{4, 5\} \end{cases}, \quad (27)$$

where  $\tau_0^{(\nu)}$  is the initial normalization value and  $\kappa^{(\nu)}$  an internal hardening variable, while  $a_\nu$ ,  $b_\nu$  and  $c_\nu$  are positive hardening parameters. The explicit expression for the 12 projected directions  $\mathbf{n}_s^{(\nu)}$  are given in Table I with  $\bar{\mathbf{v}}^{(i)}$  being the three director vectors  $\mathbf{v}^{(1)}$ ,  $\mathbf{v}^{(2)}$  and  $\mathbf{v}^{(3)}$  defined in (16) and (17), normalized to unit length. In Table I, the scalars  $\nu_{21}$  and  $\nu_{12}$  can be interpreted as the in-plane Poisson's ratios while  $m$  is a friction coefficient between out-of-plane compression and out-of-plane shearing.

$$\begin{aligned} \mathbf{n}_s^{(1)} &= \frac{1}{\sqrt{1 + \nu_{12}^2}} \left( \bar{\mathbf{v}}^{(1)} \otimes \bar{\mathbf{v}}^{(1)} - \nu_{12} \bar{\mathbf{v}}^{(2)} \otimes \bar{\mathbf{v}}^{(2)} \right), & \mathbf{n}_s^{(2)} &= \frac{1}{\sqrt{1 + \nu_{21}^2}} \left( \bar{\mathbf{v}}^{(2)} \otimes \bar{\mathbf{v}}^{(2)} - \nu_{21} \bar{\mathbf{v}}^{(1)} \otimes \bar{\mathbf{v}}^{(1)} \right) \\ \mathbf{n}_s^{(4)} &= -\bar{\mathbf{v}}^{(1)} \otimes \bar{\mathbf{v}}^{(1)}, & \mathbf{n}_s^{(5)} &= -\bar{\mathbf{v}}^{(2)} \otimes \bar{\mathbf{v}}^{(2)} \\ \mathbf{n}_s^{(3)} &= \frac{1}{\sqrt{2}} \left( \bar{\mathbf{v}}^{(1)} \otimes \bar{\mathbf{v}}^{(2)} + \bar{\mathbf{v}}^{(2)} \otimes \bar{\mathbf{v}}^{(1)} \right), & \mathbf{n}_s^{(6)} &= -\frac{1}{\sqrt{2}} \left( \bar{\mathbf{v}}^{(1)} \otimes \bar{\mathbf{v}}^{(2)} + \bar{\mathbf{v}}^{(2)} \otimes \bar{\mathbf{v}}^{(1)} \right) \\ \mathbf{n}_s^{(7)} &= -\bar{\mathbf{v}}^{(3)} \otimes \bar{\mathbf{v}}^{(3)}, & \mathbf{n}_s^{(8)} &= \bar{\mathbf{v}}^{(3)} \otimes \bar{\mathbf{v}}^{(3)} \\ \mathbf{n}_s^{(9)} &= \frac{1}{\sqrt{1 + m^2}} \left( \bar{\mathbf{v}}^{(1)} \otimes \bar{\mathbf{v}}^{(3)} + m \bar{\mathbf{v}}^{(3)} \otimes \bar{\mathbf{v}}^{(3)} \right), & \mathbf{n}_s^{(10)} &= \frac{1}{\sqrt{1 + m^2}} \left( -\bar{\mathbf{v}}^{(1)} \otimes \bar{\mathbf{v}}^{(3)} + m \bar{\mathbf{v}}^{(3)} \otimes \bar{\mathbf{v}}^{(3)} \right) \\ \mathbf{n}_s^{(11)} &= \frac{1}{\sqrt{1 + m^2}} \left( \bar{\mathbf{v}}^{(2)} \otimes \bar{\mathbf{v}}^{(3)} + m \bar{\mathbf{v}}^{(3)} \otimes \bar{\mathbf{v}}^{(3)} \right), & \mathbf{n}_s^{(12)} &= \frac{1}{\sqrt{1 + m^2}} \left( -\bar{\mathbf{v}}^{(2)} \otimes \bar{\mathbf{v}}^{(3)} + m \bar{\mathbf{v}}^{(3)} \otimes \bar{\mathbf{v}}^{(3)} \right) \end{aligned}$$

Table I: Explicit expressions for each projected direction.

To illustrate the potential functions, a contour plot  $\Phi_1 + \Phi_2 = 1$  for different projections are shown in Fig. 1. This specific contour is equivalent to the yield surface in the rate independent model by Borgqvist et al. [23]. With this illustration, the second order tensors  $\mathbf{n}_s^{(\nu)}$  are interpreted as normal directions to the contour surface where  $\nu_{12}$ ,  $\nu_{21}$  and  $m$  are the slopes referring to Fig. 1. In addition,  $\tau^{(\nu)}$  is the distance from the origin to the surface along the corresponding normal direction.

From Table I and Fig. 1, the potential function  $\Phi_2$  in (25) is identified as the contribution from the compressive deformation modes while  $\Phi_1$  governs the remaining deformation modes.

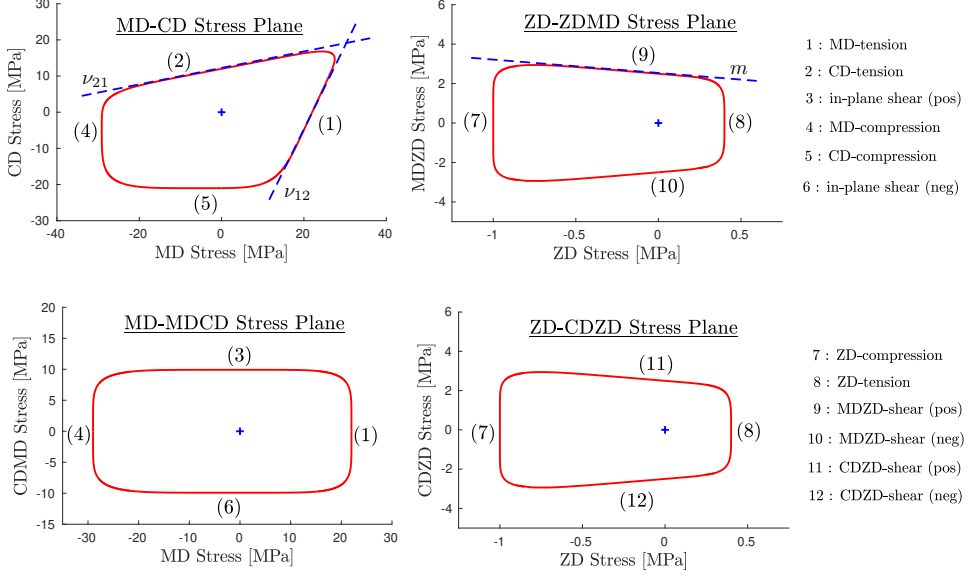


Figure 1: Contour plot of the potential functions  $\Phi_1 + \Phi_2 = 1$ .

## 2.4 Inelastic flow rule

As  $\Phi_1$  and  $\Phi_2$  are convex functions, the dissipation inequality in (15) is fulfilled by the flow rules, cf. Edelen [34],

$$\mathbf{d}^{ie} = \dot{\gamma}_1 \frac{\partial \Phi_1}{\partial \boldsymbol{\tau}} + \dot{\gamma}_2 \frac{\partial \Phi_2}{\partial \boldsymbol{\tau}} \quad \text{and} \quad \dot{\kappa}^{(\nu)} = -\dot{\gamma}^{(\nu)} \frac{\partial \Phi^{(\nu)}}{\partial K^{(\nu)}} \quad , \quad (28)$$

where the following notation is adopted,

$$[\dot{\gamma}^{(\nu)}, \Phi^{(\nu)}] = \begin{cases} [\dot{\gamma}_2, \Phi_2] & \text{when } \nu = \{4, 5, 7\} \\ [\dot{\gamma}_1, \Phi_1] & \text{otherwise} \end{cases} . \quad (29)$$

The magnitude of the irreversible flow is governed by two non-negative multipliers  $\dot{\gamma}_1$  and  $\dot{\gamma}_2$  that are postulated as,

$$\dot{\gamma}_1 = \alpha_1 \Phi_1^{p_1} \quad \text{and} \quad \dot{\gamma}_2 = \alpha_2 \langle \Phi_2 - 1 \rangle^{p_2} , \quad (30)$$

where  $\alpha_1$  and  $p_1$  are material parameters associated with the power law format for  $\dot{\gamma}_1$ . Notably, this format models creep as it is active for  $\Phi_1 > 0$ . The same format could also been used for  $\dot{\gamma}_2$ , however, as rate effects are small in comparison it will require a large exponent causing numerical problems. Instead a viscoplastic format, which allows for limited rate-effects, is adopted and governed by two parameters  $\alpha_2$  and  $p_2$  for the evolution of  $\dot{\gamma}_2$ . Clearly, the evolution associated with  $\dot{\gamma}_2$  is only active when  $\Phi_2 > 1$ . Furthermore, for  $\alpha_2 \rightarrow \infty$ , the inelastic response associated with  $\Phi_2$  will approach a

rate-independent state. Combining (25) and (28) allows the symmetric part of the inelastic velocity gradient  $\mathbf{d}^{ie}$  to be expressed in the following compact manner,

$$\mathbf{d}^{ie} = \sum_{\nu=1}^{12} \dot{\gamma}^{(\nu)} H_{\nu} \cdot \text{sym}(\mathbf{n}_s^{(\nu)}) \quad \text{with} \quad H_{\nu} = \frac{2k}{\tau^{(\nu)}} \langle \Omega \rangle_{\nu}^{2k-1} . \quad (31)$$

Similar to [13], the inelastic spin  $\boldsymbol{\omega}^{ie}$  is postulated as the skew-symmetric counterpart of (31) i.e.,

$$\boldsymbol{\omega}^{ie} = \sum_{\nu=1}^{12} \dot{\gamma}^{(\nu)} H_{\nu} \cdot \text{skew}(\mathbf{n}_s^{(\nu)}) \quad \text{with} \quad \mathbf{l}^{ie} = \mathbf{d}^{ie} + \boldsymbol{\omega}^{ie} . \quad (32)$$

By evaluating (31) and (32) together with (14), the evolution equations are summarized as,

$$\dot{\mathbf{F}}^{ie} = \mathbf{F}^{ie} \mathbf{F}^{-1} \left( \sum_{\nu=1}^{12} \dot{\gamma}^{(\nu)} H_{\nu} \mathbf{n}_s^{(\nu)} \right) \mathbf{F} \quad \text{and} \quad \dot{\mathbf{k}}^{(\nu)} = \dot{\gamma}^{(\nu)} H_{\nu} \Omega_{\nu} . \quad (33)$$

### 3 Numerical considerations

The numerical integration of the viscoelastic model, needed in a finite element setting, will now be derived. Integration of the differential equation in (12) from  $t_n$  to  $t_{n+1} = t_n + \Delta t$  yields,

$$\Gamma_{\alpha}^{n+1} = e^{-\Delta t/T_{\alpha}} \Gamma_{\alpha}^n + e^{-t_{n+1}/T_{\alpha}} \int_{t_n}^{t_{n+1}} \frac{1}{2T_{\alpha}} e^{t/T_{\alpha}} \mathbf{C}^e dt , \quad (34)$$

where  $(\bullet)^{n+1}$  denotes quantities at the current timestep  $t_{n+1}$  while  $(\bullet)^n$  refers to quantities at the previous timestep  $t_n$ , cf. a similar convolution format in Holzapfel and Simo [35]. The integral in (34) is rewritten in the following manner,

$$\Gamma_{\alpha}^{n+1} = e^{-\Delta t/T_{\alpha}} \Gamma_{\alpha}^n + \frac{e^{-t_{n+1}/T_{\alpha}}}{2} \int_{t_n}^{t_{n+1}} \frac{d}{dt} (e^{t/T_{\alpha}} \mathbf{C}^e) dt - \frac{e^{-t_{n+1}/T_{\alpha}}}{2} \int_{t_n}^{t_{n+1}} e^{t/T_{\alpha}} \dot{\mathbf{C}}^e dt . \quad (35)$$

While the first integral in (35) is trivial, the last integral is approximated using the midpoint rule together with a central approximation for the time derivative, i.e.

$$\int_{t_n}^{t_{n+1}} e^{t/T_{\alpha}} \dot{\mathbf{C}}^e dt \approx e^{(t_n + \Delta t/2)/T_{\alpha}} (\mathbf{C}_{n+1}^e - \mathbf{C}_n^e) , \quad (36)$$

which is an integration of second order accuracy, cf. Simo [36]. Combining the resulting expression for  $\Gamma_{\alpha}^{n+1}$  with  $\mathbf{Q}_{\alpha}$  in (11) results in,

$$\mathbf{Q}_{\alpha}^{n+1} = e^{-\Delta t/T_{\alpha}} \mathbf{Q}_{\alpha}^n + \frac{\eta_{\alpha}}{2T_{\alpha}} e^{-\Delta t/(2T_{\alpha})} \mathbb{C}_0 : (\mathbf{C}_{n+1}^e - \mathbf{C}_n^e) , \quad (37)$$

which is a common recurrence scheme, cf. Holzapfel et al. [37].

In addition, the constitutive equations in (30) and (33) are discretized using the implicit Euler scheme which results in the following residuals for the constitutive update,

$$\left\{ \begin{array}{l} \mathbf{R}_{F^{ie}} = \mathbf{F}_n^{ie} - \mathbf{F}^{ie} + \mathbf{F}^{ie} \mathbf{F}^{-1} \mathbf{N}_s \mathbf{F} \\ R_{\kappa}^{(\nu)} = \kappa_n^{(\nu)} - \kappa^{(\nu)} + \Delta\gamma_{\nu} H_{\nu} \Omega_{\nu} \\ R_{\gamma_1} = \Phi_1^{p_1} - \frac{\Delta\gamma_1}{\alpha_1 \Delta t} \\ R_{\gamma_2} = \langle \Phi_2 - 1 \rangle^{p_2} - \frac{\Delta\gamma_2}{\alpha_2 \Delta t} \end{array} \right. \quad \text{with} \quad \mathbf{N}_s = \sum_{\nu=1}^{12} \Delta\gamma^{(\nu)} H_{\nu} \mathbf{n}_s^{(\nu)} \quad . \quad (38)$$

Although the number of equations in the constitutive update can be reduced by eliminating  $\Delta\gamma_1$  and  $\Delta\gamma_2$ , it is practical to keep the full system of equations. With this choice,  $R_{\gamma_i} = 0$  can be interpreted as a dynamical yield surface, cf. Ristinmaa and Ottosen [38]. We solve (38) using a conventional Newton-Raphson scheme.

## 4 Uniaxial calibration

The viscosity parameters in the viscoelastic stress contribution (9), and in the evolution law (28) and (30a), are calibrated to in-plane uniaxial tension which is deemed to be the most reliable data for paperboard. The elastic parameters defined by the elastic energies (21) can be obtained with a similar procedure as for orthotropic models, cf. Borgqvist et al. [22], in which the initial response is considered, i.e.  $d\mathbf{S}_0 = (\mathbb{C}_0^{ip} + \mathbb{C}_0^{oop}) d\mathbf{E}_0$  where the initial in-plane tangent is  $\mathbb{C}_0^{ip} = (1 + \sum_{\alpha} \eta_{\alpha}/T_{\alpha}) \mathbb{C}_0$  with  $\mathbb{C}_0$  calculated in (24) and the initial out-of-plane tangent  $\mathbb{C}_0^{oop}$  provided in Appendix E. The anisotropy is defined by the two characteristic directions MD and CD, and as such, creep and relaxation measurements in both directions have been considered in the calibration of the rate-dependent properties. Experiments have been performed in a climate-controlled environment with a temperature of 23° and 50 % relative humidity.

The relaxation experiment is initiated, by a displacement controlled phase with the constant strain rate  $\dot{\epsilon} = 0.00167 [1/s]$ , until a predefined strain level is reached, thereafter the displacement remains constant and the stress relaxation is monitored. The strain and stress measurements are the engineering strain and the engineering stress, respectively. The relaxation experiments are presented in Fig. 2 a) and 3 a) where three strain levels,  $\epsilon_0 = [0.01, 0.02, 0.03]$  along CD, and  $\epsilon_0 = [0.007, 0.010, 0.015]$  along MD, have been considered for the starting point of the relaxation phase. The duration of the relaxation phase is  $t = 30$  s and the results are presented in Fig. 2 b) and 3 b) where the current stress  $\sigma(t)$  is normalized with respect to the initial stress level  $\sigma_0$  corresponding to  $\epsilon_0$ . The normalization process renders that different strain levels will produce similar normalized relaxation histories. This feature was previously observed in Alfthan [16].

In a similar fashion, creep experiments are conducted with the same initial displacement phase as for the relaxation tests. The displacement is increased until a prescribed stress level is reached thereafter the stress remains constant and the strain is measured as a function of time. Three stress levels,  $\sigma_0 = [13, 16, 19]$  MPa along CD, and  $\sigma_0 = [28, 33, 39]$  MPa along MD, are considered and the results are shown in Fig. 2 c) and Fig. 3 c). During the creep phase, Fig. 2 d) and Fig. 3 d),

the strain  $\epsilon(t)$  is normalized with respect to the initial creep level  $\epsilon_0$  corresponding to  $\sigma_0$ . As for the relaxation experiments, similar creep histories are obtained when the response is normalized. In Fig. 2 and 3, an additional unloading phase is included after the relaxation and creep phase, however, no calibration attempt is made in capturing the non-linear feature observed during unloading.

The viscoelastic model consists of four networks, i.e.  $\alpha = 4$  in equation (9), (11) and (12), with corresponding parameters  $T_\alpha$  and  $\eta_\alpha$  tabulated in Table 2. The calibration of the inelastic parameters associated with the evolution of  $\dot{\gamma}_1$  are,  $\alpha_1 = 0.001$  MPa/s and  $p_1 = 3.8$ . The overall behavior of the model is in good agreement with the results as seen in Fig. 2 and 3.

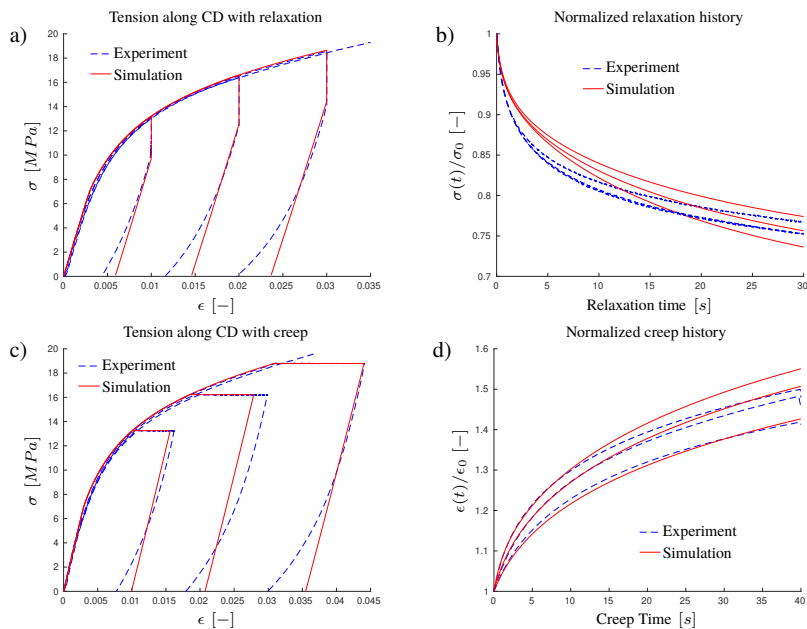


Figure 2: Relaxation a) and creep b) tests for in-plane uniaxial tension along the CD direction. The initial phase is displacement controlled with a strain rate of  $\dot{\epsilon} = 0.00167$  [1/s].

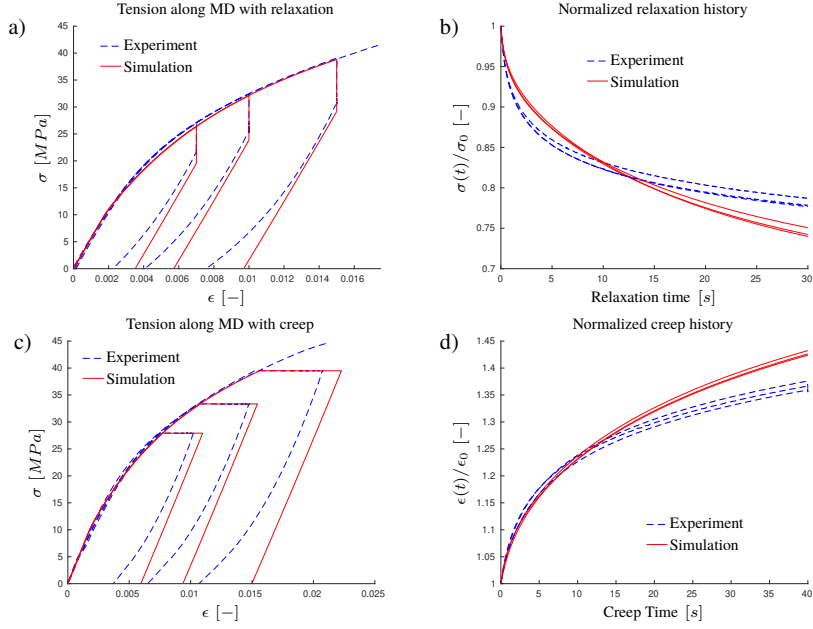


Figure 3: Relaxation a) and creep b) tests for in-plane uniaxial tension along the MD direction. The initial phase is displacement controlled with a strain rate of  $\dot{\epsilon} = 0.00167$  [1/s].

To further evaluate the in-plane rate-dependent behavior, different strain rates are considered. In Fig. 4 a), the strain rate is increased by a factor of 100 compared to the previous creep and relaxation experiments. The rate-dependent response is measured along the directions MD, CD and the direction  $45^\circ$  between the MD and CD directions. Referring to Fig. 4 a), the model is in close agreement with experiments.

In addition, different strain rates are considered for out-of-plane tension. The numerical and experimental results are shown in Fig. 4 b) where it is noted that the overall rate-dependent behavior is captured by the model.

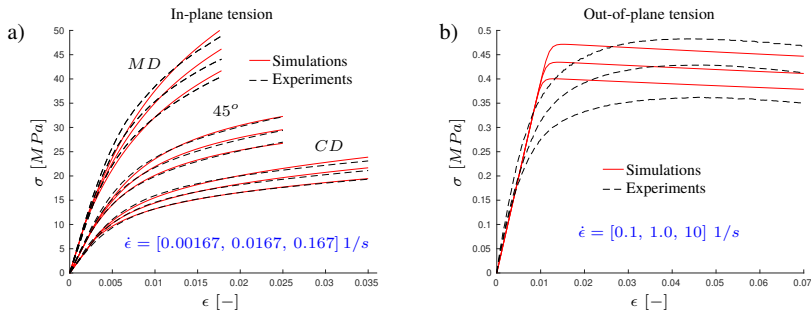


Figure 4: Different strain rates during in-plane and out-of-plane tension.

Out-of-plane compression experiments suggest that the rate dependency is, for this mode, very low and therefore  $\gamma_2$  is modeled such that the out-of-plane compression behavior is almost rate-independent, i.e.  $\alpha_2 = 100$  MPa/s and  $p_2 = 2$  where a large value for  $\alpha_2$  corresponds to low rate dependency, cf. the discretized residual  $R_{\gamma_2}$  in (38). Furthermore, due to lack of reliable in-plane compression experiments this mode is also modeled as being nearly rate-independent from the inelastic contribution provided by  $\gamma_2$ .

The calibration for out-of-plane compression is shown in Fig. 5 a) and the model behavior during in-plane compression is presented in Fig. 5 b) along with the strength levels obtained from the long edge compression (LEC) test in [23]. Accurate measurements for in-plane compression are difficult to obtain, as such, the hardening in Fig. 5 b) is calibrated to fit the initial response during line-folding.

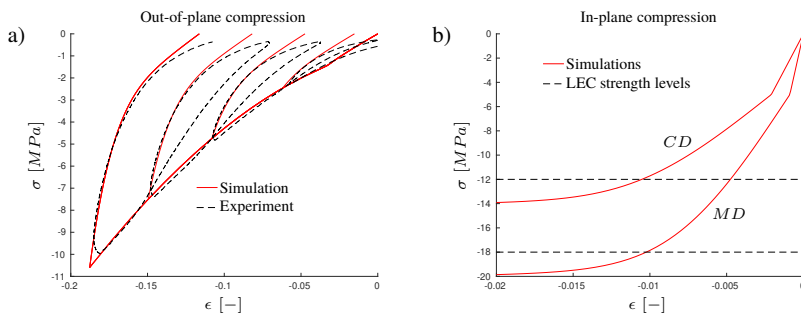


Figure 5: Out-of-plane and in-plane compression.

The elastic hardening parameters,  $A_6$  and  $A_7$ , defined in (21) have no impact on the initial stiffness and has been calibrated to match the unloading curves in Fig. 5 a). The Poisson's ratios  $\nu_{12}$  and  $\nu_{21}$ , used to define the directions of projection in Table 1, are determined with the same methodology as in [22]. The remaining parameters in the model are related to out-of-plane shearing and due to lack of reliable data, the initial value  $\tau_0$  and the internal friction parameter  $m$  are chosen to fit the vertical force during line-creasing, which is similar to the approach in Borgqvist et al. [13]. The calibrated values for all material parameters are summarized in Appendix A.

## 5 The line-creasing procedure

The line-crease, previously studied in Nygård et al. [9] and Borgqvist et al. [13], is in this example revisited using the proposed material model. The experimental setup is schematically illustrated in Fig. 6 and it consists of a 38 mm wide paperboard strip placed between a female groove and a male dye. A load cell measures the in-plane force while the strip is subject to a constant in-plane displacement  $u_x$  such that the initial webtension is 57 N. During the creasing operation, the male dye is vertically displaced towards the female cavity, resulting in localized deformation which will ease subsequent folding. Throughout the procedure, the vertical force is monitored using a load cell attached to the female dye. The male dye comes in contact with the female groove when  $u_z = 0.4$  mm as shown in Fig. 6. Two snapshots of experimental setup during creasing is provided in Fig. 7.

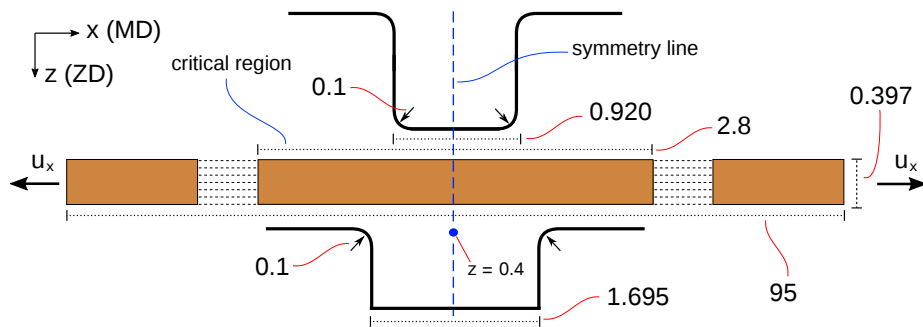


Figure 6: Schematic of the line-creasing experiment, dimensions in mm.

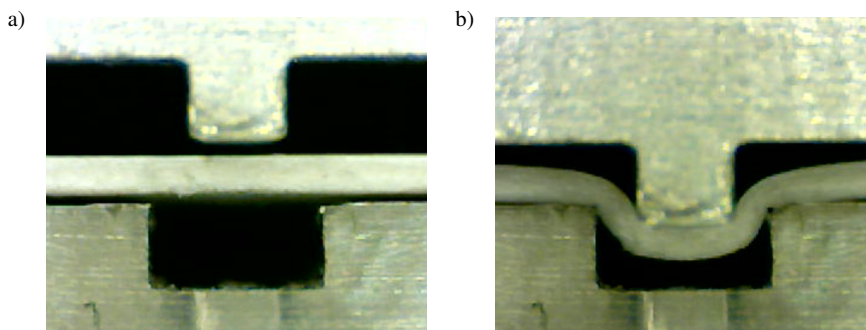


Figure 7: Snapshots of the line-creasing experiment.

The material model is implemented in the commercial software Abaqus using the UMAT subroutine feature, [39]. Balance of linear momentum is modeled to be quasi-static and solved using the build in implicit solver. The tools are modeled as analytically rigid shells while the paperboard

is discretized with fully integrated, eight-node, continuum elements denoted C3D8 in Abaqus element library. Contact between the paperboard and the analytic shells are modeled using a tangential penalty formulation with a friction coefficient equal to 0.2. To reduce the computational cost, a paperboard width of 3.8 mm is used together with symmetry conditions along the dashed line in Fig. 6. The critical region close to the creased zone is discretized with a mesh of uniform aspect ratio and sidelength equal to 0.0128 mm. The line-creasing operation is simulated with both the MD and CD direction being prestretched. In Fig. 8, the simulated macroscopic forces are shown for the slow displacement rate of  $\dot{u} = 0.07$  mm/s while a snapshot of the simulation, at peak load during creasing along the MD direction, is presented in Fig. 9.

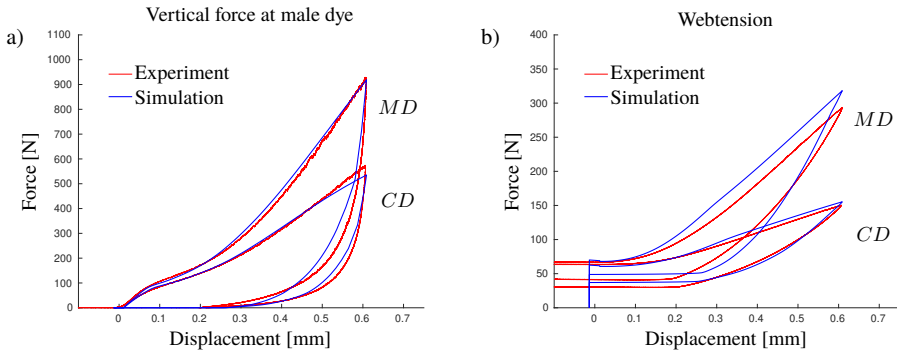


Figure 8: Line-creasing, measurements and simulations along the MD and CD direction with a displacement rate of  $\dot{u} = 0.07$  mm/s.

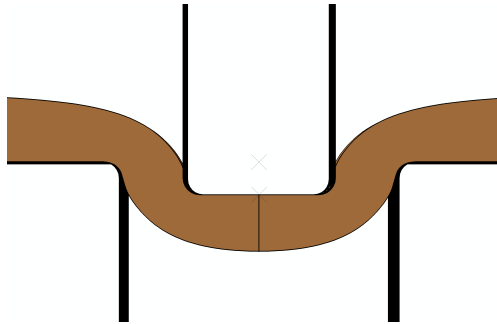


Figure 9: Snapshot of the creasing simulation along the MD direction.

The numerical results in Fig. 8 are in close agreement with measurements, although, the maximum webtension in MD shows a slight deviation. Next, the rate-dependency in the creasing process is considered by increasing the displacement rate to  $\dot{u}_z = 0.7$  mm/s and  $\dot{u}_z = 7$  mm/s. The experimental and numerical results are shown in Fig. 10 and we see that the model is able to capture the overall rate-dependent response.

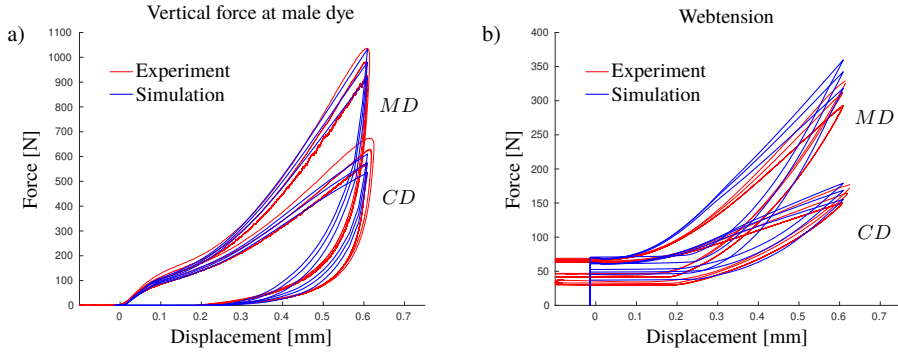


Figure 10: Measurements and simulations along MD and CD direction with different displacement rates,  $\dot{u} = [0.07, 0.7, 7]$  mm/s.

The creep response is investigated by considering a process that consists of two separate steps. In the initial step, a constant displacement rate,  $\dot{u}_z = 0.07$  mm/s, is applied to the male dye until a specified vertical force is reached, which is followed by a force-controlled phase where the vertical force remains fixed while the horizontal force is allowed to relax during  $t = 30$  s. The experiments along with the numerical results are shown in Fig. 11 a) and b), where two different load levels have been considered for both the MD and CD directions. In Fig. 11 c) and d), the creep histories along MD and CD are shown where the displacement of the male dye  $u(t)$  is normalized against the terminal displacement  $u_0$  corresponding to the load level at which the creep step is initiated.

The normalized displacement history, predicted by the model in Fig. 11 c) and d), has a similar response for both load levels, a feature shared with the experiment. The entire creep history is not perfectly reproduced by the model. One reason might be the influence of creep during out-of-plane shearing, a difficult phenomena to accurately measure with experiments and thus also difficult to calibrate. Another similarity, shared by the numerical result, is the reduction of the in-plane force during the creep stage, referring to Fig. 11 b). In the case of the response along CD, the agreement with the experiment is similar while the response along MD is less accurate.

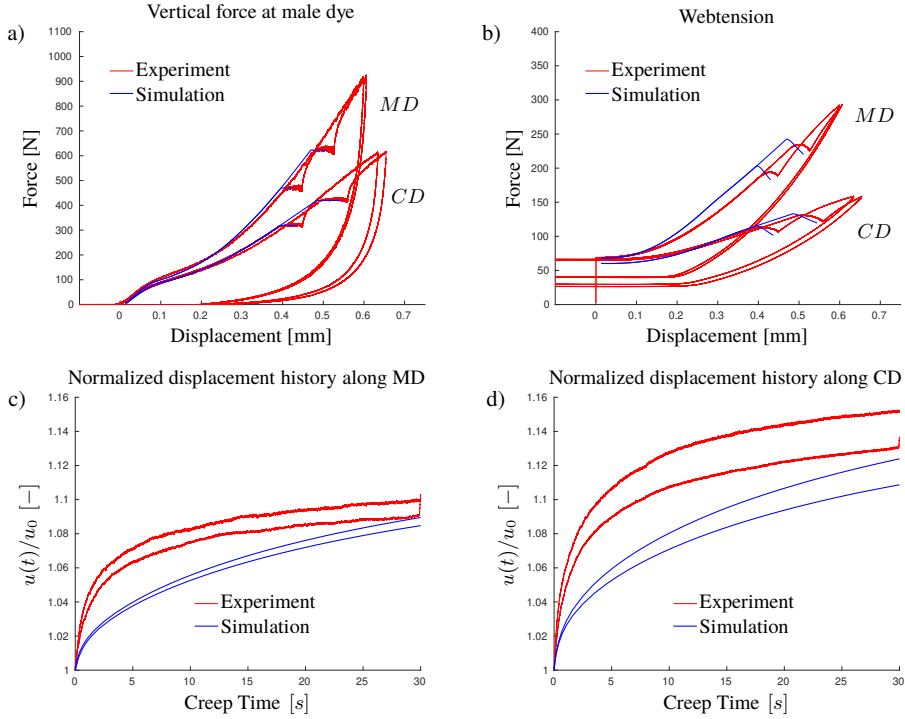


Figure 11: Creep at different displacement levels. The initial phase is displacement controlled with a rate equal to  $\dot{u} = 0.07$  mm/s.

## 6 The line-folding operation

To further illustrate the model capabilities, the line folding operation of increased paperboard previously investigated in Borgqvist et al. [23] is considered, although with a different experimental device, the Marbach bend tester (Marbach Group; Heilbronn, Germany). The setup is schematically shown in Fig. 12 where two clamps are rotated while the paperboard is constrained by a load cell resulting in folding as illustrated in Fig. 12. The location of the center of rotation is indicated by a red cross. The paperboard is clamped with a compressive pressure equal to 0.7 MPa and the free length of the paperboard is 50 mm while the thickness and width are equal to 0.4 mm and 25 mm, respectively. The simulation is performed under the same assumptions as for the line-creasing simulation, i.e. quasi-static conditions prevail and the same contact settings between the rigid tools and the paperboard applies. The problem is solved using an implicit solver. Both clamps and the load cell are modeled as analytically rigid shells while the paperboard is discretized with fully integrated, eight-node, continuum elements denoted C3D8 in the Abaqus library. To reduce the computational cost, a paperboard width of 2.5 mm is used with a single element along the width. In regions close to the clamps and the load cell, the mesh size along the thickness and length direction of the board is 0.006

mm.

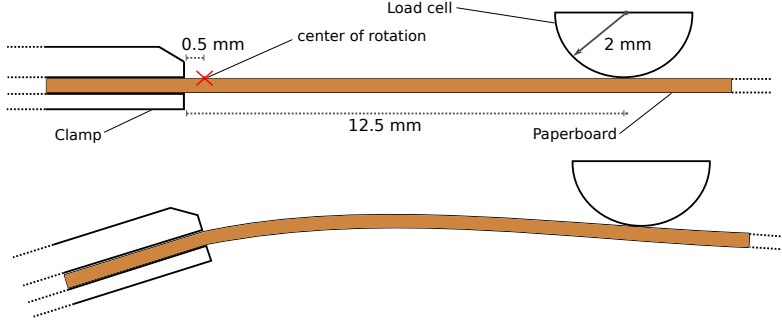


Figure 12: Schematics of the line-folding operation.

The experiment is performed in two steps. During the initial step, the clamps are rotated with an angular velocity equal to  $\dot{\theta} = 90^\circ/s$  while the force at the load cell is measured. After  $\theta = 90^\circ$ , a relaxation test is performed during  $t = 15$  s. Both MD and CD directions are considered and the results from the first step are presented in Fig. 13 where both experiments and simulations are shown.

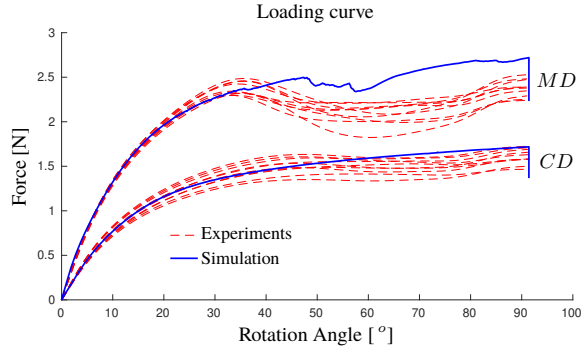


Figure 13: Measurements and simulations along MD and CD direction in the line-folding setup,  $\dot{\theta} = 90^\circ/s$  during loading.

The model is able to qualitatively capture the overall response of the system with similar accuracy to [23]. The most significant deviation occurs for the MD direction where the force reduction is delayed in the simulation. Notably, the model predicts formations of wrinkles, shown in Fig. 14, which are also present in the experimental tests. This is a unique feature of the model which, to the authors knowledge, is only shared by its predecessor in [13].

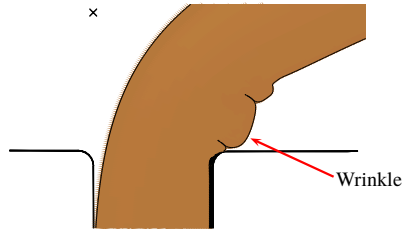


Figure 14: Formation of wrinkle along the MD direction after relaxation.

After reaching the final rotation angle, relaxation is considered. In Fig. 15, the normalized force  $F(t)/F_0$  during the relaxation phase is shown where the normalization  $F_0$  is defined as the terminal value for the loading phase. When the force is normalized in this manner, the relaxation history for MD and CD are very similar, a feature shared by both experiments and simulation. This characteristic feature share close resemblance to the previous uniaxial tests, Fig. 2 b) and 3 b), i.e. different levels for relaxation produce a similar relaxation history. However, the prediction by the model is lower compared to the experimental measurements. The reason for the discrepancy might be connected to the compliance of the experimental setup and uncertainties regarding the relaxation behavior during in-plane compression, a challenging phenomena to accurately measure due to the slenderness of paperboard.

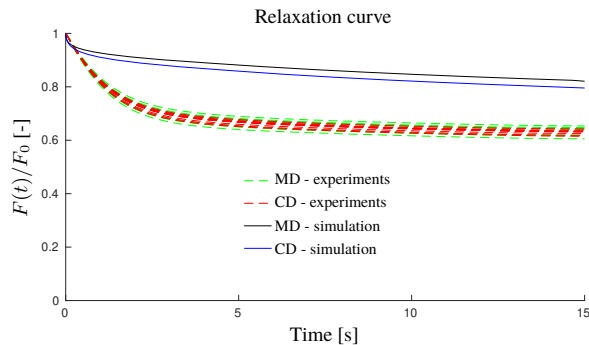


Figure 15: Relaxation history at  $\theta = 90^\circ$ .

## 7 Conclusions

The model developed in Borgqvist et al. [23] has been extended to include the experimentally observed rate-dependent response in paperboard. For this endeavor, viscoelasticity was introduced for the in-plane response with a thermodynamically consistent generalization of the Maxwell framework. Furthermore, the evolution of the inelastic part of the deformation gradient was modeled using two potential functions resulting in two inelastic multipliers,  $\gamma_1$  and  $\gamma_2$ , where the latter corresponds to the compression modes and was model as nearly rate-independent.

The viscoelastic parameters, and the remaining inelastic parameters corresponding to  $\gamma_1$ , was calibrated against creep and relaxation experiments for in-plane uniaxial tension along the characteristic material directions MD and CD. The calibration is in good agreement with measurements. The model was able to capture the overall rate-dependent behavior over a range of loading rates for uniaxial in-plane and out-of-plane tension.

In addition to the inclusion of rate-effects, the out-of-plane compression was modeled without an unphysical switch function which is present in a number of previous paperboard models, cf. [23] and [26].

To evaluate the capabilities of the model, two experimental setups were considered, line-creasing which was previously studied in [13], and the line-folding operation with a similar setup used in [23]. In the case of line-creasing, the model was able to predict the rate-dependent response observed by the macroscopic forces with good agreement to the measured results. Furthermore, the creep behavior was investigated and the model was able to reproduce the response with relatively good agreement. To improve the results, further work is needed, one aspect that needs more attention is the influence of creep during out-of-plane shearing, a difficult phenomena to accurately measure with experiments and thus also difficult to incorporate in the model. For the line-folding operation, the model qualitatively captures the measured force during folding and was able to predict the formation of wrinkles present in the experimental tests. The inclusion of a damage formulation is expected to increase predictive capabilities and will be considered in future work.

## 8 Acknowledgments

This work was performed within Tresearch and financially supported by Tetra Pak and the strategic innovation program BioInnovation (Vinnova Project Number 2017-05399), a joint collaboration between Vinnova, Formas and the Swedish Energy Agency. The computations was enabled by resources provided by the Swedish National Infrastructure for Computing (SNIC) at LUNARC partially funded by the Swedish Research Council through grant agreement no. 2018-05973.

## Appendix A Material parameters

The calibrated material parameters for the paperboard model are outlined in this section. The viscoelastic parameters  $T_\alpha$  and  $\eta_\alpha$ , corresponding to four rheological networks, are presented in Table 2. The elastic parameters  $A_i$  defining the Helmholtz free energy are tabulated in Table 3. The inelastic parameters associated with the potential functions  $\Phi_1$  and  $\Phi_2$  are shown in Table 4, i.e. the initial normalization factors  $\tau_0^{(\nu)}$  and the corresponding hardening parameters  $a_\nu$ ,  $b_\nu$  and  $c_\nu$ . The inelastic parameters,  $\alpha_i$  and  $p_i$ , are tabulated in Table 5 along with the in-plane Poisson's ratios,  $\nu_{12}$  and  $\nu_{21}$ , the internal paper-paper friction  $m$  and the exponent  $k$ .

Network $\alpha$	1	2	3	4
$T_\alpha$ [s]	10	20	30	300
$\eta_\alpha$ [s]	1.275	2.550	6.375	60

Table 2: Viscoelastic parameters corresponding to the four rheological networks.

$A_1$ [MPa]	$A_2$ [MPa]	$A_3$ [MPa]	$A_4$ [MPa]	$A_5$ [MPa]	$A_6$ [MPa]	$A_7$ [-]
1162	91	20	699	69	746977	3

Table 3: Elastic parameters defined in the elastic free energy.

$\nu$	$\tau_0^{(\nu)}$ [MPa]	$a_\nu$ [MPa]	$b_\nu$ [-]	$c_\nu$ [MPa]
1	9.6687	8.2197	1545	200
2	7.0896	2.5563	1561	80
3	6.2023	3.3048	2033	0
4	5	14.5	200	
5	5	8.7	200	
6	6.2023	3.3048	2033	0
7	1.415	0	0	57.97
8	0.38	0	0	0
9	$2.6551 \cdot (1 + m^2)^{-1/2}$	0	0	0
10	$2.6551 \cdot (1 + m^2)^{-1/2}$	0	0	0
11	$2.6551 \cdot (1 + m^2)^{-1/2}$	0	0	0
12	$2.6551 \cdot (1 + m^2)^{-1/2}$	0	0	0

Table 4: Inelastic parameters associated with the potentials  $\Phi_1$  and  $\Phi_2$ .

$\alpha_1$ [MPa/s]	$p_1$ [-]	$\alpha_2$ [MPa/s]	$p_2$ [-]	$\nu_{12}$ [-]	$\nu_{21}$ [-]	$m$ [-]	$k$ [-]
0.001	3.8	100	2	0.45726198	0.18774576	0.300	3

Table 5: Inelastic viscosity parameters and other essential parameters.

## Appendix B Scalar functions

The Kirchhoff stress in (23) consists of four scalar functions  $R_i$  associated with  $\tau_{ip}^\infty$  and five scalar functions  $P_i$  corresponding to  $\tau_{oop}$ , they are the following

$$\left\{ \begin{array}{l} R_1 = A_1 (I_{11}^{-1} - I_{11}^{-3}) + A_4 I_{11}^{-1} \\ R_2 = A_2 (I_{22}^{-1} - I_{22}^{-3}) + A_4 I_{22}^{-1} \\ R_3 = A_4 I_{12}^{-3} \\ R_4 = -A_4 I_{12}^{-1} \\ P_1 = A_5 I_{22} I_{13} I_{11}^{-1} \\ P_2 = A_5 I_{11} I_{13} I_{22}^{-1} \\ P_3 = A_3 I_{12}^{-2} (I_{33} - I_{33}^{-1}) + A_6 I_{12}^{-2} (I_{33}^2 - 1) \left( \frac{I_{33}^2 - 1}{2} - \ln(I_{33}) \right)^{A_7 - 1} \\ P_4 = -A_5 J^e \\ P_5 = A_5 I_{11} I_{22} I_{13}^{-1} J^{e-2} \end{array} \right. . \quad (39)$$

## Appendix C Derivation of the configurational energy

In this section, the derivation of the configurational energy  $\Upsilon_\alpha$  in (10) is outlined. The viscoelastic model is based on the assumption that the configurational energy  $\Upsilon_\alpha$  is quadratic with respect to  $\mathbf{\Gamma}_\alpha$  in the following manner,

$$\frac{\partial^2 \Upsilon_\alpha}{\partial \mathbf{\Gamma}_\alpha \otimes \partial \mathbf{\Gamma}_\alpha} = \frac{\eta_\alpha}{T_\alpha} \mathbb{C}_0 . \quad (40)$$

Integrating expression (40) twice with respect to  $\mathbf{\Gamma}_\alpha$  renders,

$$\Upsilon_\alpha = \frac{\eta_\alpha}{2T_\alpha} \mathbf{\Gamma}_\alpha : \mathbb{C}_0 : \mathbf{\Gamma}_\alpha + \mathbf{A}(\mathbf{C}^e) : \mathbf{\Gamma}_\alpha + B(\mathbf{C}^e) , \quad (41)$$

with  $\mathbf{A}$  being a second order tensor and  $B$  a scalar, both potentially  $\mathbf{C}^e$  dependent. The configurational energy  $\Upsilon_\alpha$  in (41) is constrained by (5) and (8) such that,

$$\left[ \mathbf{\Gamma}_\alpha : \left( 2 \frac{\partial \mathbf{A}}{\partial \mathbf{C}^e} + \frac{\eta_\alpha}{T_\alpha} \mathbb{C}_0 \right) \right] + \left[ \mathbf{A} + 2 \frac{\partial B}{\partial \mathbf{C}^e} \right] = \mathbf{0} , \quad (42)$$

is obtained. This expression is fulfilled if,

$$\frac{\partial \mathbf{A}(\mathbf{C}^e)}{\partial \mathbf{C}^e} = -\frac{\eta_\alpha}{2T_\alpha} \mathbb{C}_0 \quad \text{and} \quad \frac{\partial B(\mathbf{C}^e)}{\partial \mathbf{C}^e} = -\frac{1}{2} \mathbf{A} . \quad (43)$$

Integrating both equations provides,

$$\mathbf{A} = -\frac{\eta_\alpha}{2T_\alpha} \mathbb{C}_0 : \mathbf{C}^e \quad \text{and} \quad B = \frac{\eta_\alpha}{8T_\alpha} \mathbf{C}^e : \mathbb{C}_0 : \mathbf{C}^e . \quad (44)$$

Using (41) in (44), the following is obtained,

$$\Upsilon_\alpha = \frac{\eta_\alpha}{8T_\alpha} (2\Gamma_\alpha - \mathbf{C}^e) : \mathbb{C}_0 : (2\Gamma_\alpha - \mathbf{C}^e) \quad , \quad (45)$$

which is the expression for the configurational energy in (10).

## Appendix D Positive definiteness of $\mathbb{C}_0$

The viscoelastic part of the dissipation in (5) requires,

$$\dot{\Gamma}_\alpha : \mathbb{C}_0 : \dot{\Gamma}_\alpha \geq 0 \quad , \quad (46)$$

which is fulfilled if  $\mathbb{C}_0$  is positive definite. For the proposed model,  $\mathbb{C}_0$  is provided by (24) and in combination with the definition of  $\mathbf{M}_0^{(i)}$  in (2), it is possible to identify the following,

$$\begin{aligned} \dot{\Gamma}_\alpha : \mathbb{C}_0 : \dot{\Gamma}_\alpha = & 2A_1 \left( \mathbf{M}_0^{(1)} : \dot{\Gamma}_\alpha \right)^2 + 2A_2 \left( \mathbf{M}_0^{(2)} : \dot{\Gamma}_\alpha \right)^2 + A_4 \left( \dot{\Gamma}_\alpha : \mathbf{M}_0^{(1)} \right)^2 \\ & + A_4 \left( \dot{\Gamma}_\alpha : \mathbf{M}_0^{(2)} \right)^2 + A_4 \left( \dot{\Gamma}_\alpha : \mathbf{M}_0^{(1)} + \dot{\Gamma}_\alpha : \mathbf{M}_0^{(2)} \right)^2 \\ & + A_4 \left( \mathbf{v}_0^{(1)} \cdot \dot{\Gamma}_\alpha \cdot \mathbf{v}_0^{(2)} + \mathbf{v}_0^{(2)} \cdot \dot{\Gamma}_\alpha \cdot \mathbf{v}_0^{(1)} \right)^2 \end{aligned} \quad . \quad (47)$$

The above expression is a sum of quadratic terms, thus  $\mathbb{C}_0$  is positive definite and (46) is fulfilled.

## Appendix E Initial out-of-plane tangent $\mathbb{C}_0^{oop}$

The initial out-of-plane tangent is defined as,

$$\mathbb{C}_0^{oop} = 4\rho_0 \left. \frac{\partial^2 \Psi_{oop}^e}{\partial \mathbf{C}^e \otimes \partial \mathbf{C}^e} \right|_{\mathbf{C}^e = \mathbf{I}} \quad , \quad (48)$$

and with the specific out-of-plane energy  $\Psi_{oop}^e$  in (21) the following tangent is obtained,

$$\mathbb{C}_0^{oop} = 2A_3 (\mathbf{M}_0^{(3)} \otimes \mathbf{M}_0^{(3)}) + \sum_{i=1}^3 \sum_{\substack{j=1 \\ i \neq j}}^3 A_5 (\mathbf{M}_0^{(i)} \bar{\otimes} \mathbf{M}_0^{(j)} + \mathbf{M}_0^{(i)} \underline{\otimes} \mathbf{M}_0^{(j)}) \quad . \quad (49)$$

## References

- [1] J. Simon. A review of recent trends and challenges in computational modeling of paper and paperboard at different scales. *Archives of Computational Methods in Engineering*, 2020.
- [2] A. Kulachenko and T. Uesaka. Direct simulations of fiber network deformation and failure. *Mechanics of Materials*, 51:1–14, 2012.

- [3] D. Wilbrink, L. Beex, and R. Peerlings. A discrete network model for bond failure and frictional sliding in fibrous materials. *International Journal of Solids and Structures*, 50:1354–1363, 2013.
- [4] L. Beex, R. Peerlings, and M. Geers Department. A multiscale quasicontinuum method for dissipative lattice models and discrete networks. *Journal of the Mechanics and Physics of Solids*, 64:154–169, 2014.
- [5] J. Sliseris, H. Andra, M. Kabel, B. Dix, and B. Plinke. Numerical prediction of the stiffness and strength of medium density fiberboard. *Mechanics of Materials journal*, 79:73–84, 2014.
- [6] H. Huang and M. Nygård. A simplified material model for finite element analysis of paperboard creasing. *Nordic Pulp and Paper Research Journal*, 25:505–512, 2010.
- [7] H. Huang, A. Hagman, and M. Nygård. Quasi static analysis of creasing and folding for three paperboards. *Mechanics of Materials journal*, 69:11–34, 2014.
- [8] L. Beex and R. Peerlings. An experimental and computational study of laminated paperboard creasing and folding. *International Journal of Solids and Structures*, 46:4192–4207, 2009.
- [9] M. Nygård, M. Just, and J. Tryding. Experimental and numerical studies of creasing of paperboard. *International Journal of Solids and Structures*, 46:2493–2505, 2009.
- [10] M. Harrysson, A. Harrysson, and M. Ristinmaa. Spatial representation of evolving anisotropy at large strains. *International Journal of Solids and Structures*, 44:3514–3532, 2007.
- [11] Y. Li, S. Stapleton, S. Reese, and J. Simon. Anisotropic elastic-plastic deformation of paper: Out-of-plane model. *International Journal of Solids and Structures*, 130-131:172–182, 2018.
- [12] Y. Yujun, S. Stapleton, S. Reese, and J. Simon. Anisotropic elastic-plastic deformation of paper: In-plane model. *International Journal of Solids and Structures*, 100-101:286–296, 2016.
- [13] E. Borgqvist, M. Wallin, M. Ristinmaa, and J. Tryding. An anisotropic in-plane and out-of-plane elasto-plastic continuum model for paperboard. *Composite Structures*, 126:184–195, 2015.
- [14] S. Nagasawa and S. Ozawa. Effect of bending velocity on time-dependent release behavior of creased white-coated paperboard. *The Japan Society of Mechanical Engineers*, 3:1–11, 2016.
- [15] D. Gunderson, J. Considine, and C. Scott. The compressive load-strain curve of paperboard: Rate of load and humidity effects. *Journal of pulp and paper science*, 4:37–41, 1988.
- [16] J. Alfthan. Experimental study of non-linear stress relaxation and creep of paper materials and the relation between the two types of experiments. *Nordic Pulp and Paper Research Journal*, 25:351–357, 2010.
- [17] J. Lif, S. Östlund, and C. Fellers. In-plane hygro-viscoelasticity of paper at small deformations. *Nordic Pulp and Paper Research Journal*, 20:139–149, 2005.

- [18] J. Strömbro and P. Gudmundson. Mechano-sorptive creep under compressive loading, a micromechanical model. *International Journal of Solids and Structures*, 45:2420–250, 2008.
- [19] E. Bosco, R. Peerlings, and M. Geers. Predicting hygro-elastic properties of paper sheets based on an idealized model of the underlying fibrous network. *International Journal of Solids and Structures*, 56-57:43–52, 2015.
- [20] D. Tjahjanto, O. Girlanda, and S. Östlund. Anisotropic viscoelastic-viscoplastic continuum model for high-density cellulose-based materials. *Journal of the Mechanics and Physics of Solids*, 84:1–20, 2015.
- [21] Q. Xia, M. Boyce, and D. Parks. A constitutive model for the anisotropic elastic-plastic deformation of paper and paperboard. *International Journal of Solids and Structures*, 39:4053–4071, 2002.
- [22] E. Borgqvist, T. Lindström, M. Wallin, J. Tryding, and M. Ristinmaa. Distortional hardening plasticity model for paperboard. *International Journal of Solids and Structures*, 51:2411–2423, 2014.
- [23] E. Borgqvist, M. Wallin, J. Tryding, M. Ristinmaa, and E. Tudisco. Localized deformation in compression and folding of paperboard. *Packaging Technology and Science*, 29:397–414, 2016.
- [24] K. Robertsson, E. Borgqvist, M. Wallin, M. Ristinmaa, J. Tryding, A. Giampieri, and U. Perego. Efficient and accurate simulation of the packaging forming process. *Packaging Technology and Science*, 31:557–566, 2018.
- [25] M. Schwarze and S. Reese. A reduced integration solid-shell finite element based on the eas and the ans concept-large deformation problems. *International Journal for Numerical Methods in Engineering*, 85:289–329, 2010.
- [26] A. Harrysson and M. Ristinmaa. Large strain elasto-plastic model of paper and corrugated board. *International Journal of Solids and Structures*, 45:3334–3352, 2008.
- [27] K. Persson. Material model for paper experimental and theoretical aspects. *Master's thesis, Lund Institute of Technology*, 1991.
- [28] S. Borodulina, A. Kulachenko, S. Galland, and M. Nygårds. Stress-strain curve of paper revisited. *Nordic Pulp and Paper Research Journal*, 27:318–328, 2012.
- [29] E. Kröner. Allgemeine kontinuumstheorie der versetzungen und eigenspannungen. *Archive for Rational Mechanics and Analysis*, 4:273–334, 1960.
- [30] Y. Dafalias. Plastic spin: necessity or redundancy? *International Journal of Plasticity*, 14:909–931, 1998.
- [31] J. Mandel. Plasticité classique et viscoplasticité. Courses and Lectures, No. 97, ICMS, Udine, Springer, Wien-New York, 1971.

- [32] C. Truesdell and W. Noll. *The non-linear field theories of mechanics*, volume 3 of *Handbuch der Physik*. Springer-Verlag.
- [33] B. Coleman and M. Gurtin. Thermodynamics with internal state variables. *Journal of Chemical Physics*, 47:597–613, 1967.
- [34] D. Edelen. A nonlinear onsager theory of irreversibility. *International Journal of Engineering Science*, 10:481–490, 1972.
- [35] G. Holzapfel and J. Simo. A new viscoelstic constitutive model for continous media at finite thermomechanical changes. *International Journal of Solids and Structures*, 33:3019–3034, 1996.
- [36] J. Simo. On a fully three-dimensional finite-strain viscoelstic damage model: formulation and computational aspects. *Computer methods in applied mechanics and engineering*, 60:153–173, 1987.
- [37] G. Holzapfel. On large strain viscoelasticity: continuum formulation and finite element applications to elastomeric structures. *International Journal for Numerical Methods in Engineering*, 39:3903–3926, 1996.
- [38] M. Ristinmaa and N. Ottosen. Consequences of dynamic yield surface in viscoplasticity. *International Journal of Solids and Structures*, 37:4601–4622, 2000.
- [39] Dassault Systems. *Abaqus 6.13 analysis user's manual*.



# Paper C

Kristofer Robertsson, Erik Jacobsson, Mathias Wallin,  
Eric Borgqvist, Matti Ristinmaa and Johan Tryding

*A continuum damage model for creasing and folding of paperboard*

Submitted for publication



# A continuum damage model for creasing and folding of paperboard

Kristofer Robertsson<sup>1</sup>, Erik Jacobsson<sup>1</sup>, Mathias Wallin<sup>1</sup>, Eric Borgqvist<sup>2</sup>,  
Matti Ristinmaa<sup>1</sup> and Johan Tryding<sup>1,2</sup>

<sup>1</sup>Division of Solid Mechanics, Lund University, P.O Box 118, 221 00, Sweden

<sup>2</sup>Tetra Pak Packaging Solutions, Lund, 221 86, Sweden

## Abstract

A continuum damage framework is proposed for modeling the delamination process occurring in paperboard during mechanical loading. The main application of interest is line-creasing and subsequent line-folding used in package forming. To adequately capture creasing and folding, a continuum damage framework which uses a single isotropic damage variable that evolves with the plastic strains associated with out-of-plane shearing is used. The damage evolution is calibrated against folding experiments for a specific reference mesh and a simple scaling strategy is proposed to reduce the inherent mesh dependency. To highlight the potential of the proposed model, an illustrative 3D example is considered where a paperboard sheet is creased by two plates and folded to resemble the corner of a package.

# 1 Introduction

Paperboard is a cellulose based material and it is one of the main components used in packages for food products. On sheet level, paperboard is anisotropic due the manufacturing process where fibers are continuously sprayed on a moving web. The majority of the fibers will align in the web direction which is denoted the Machine Direction (MD) while the in-plane orthogonal direction to MD is defined as the cross direction (CD). In addition, the stacking direction of the fibers is termed the out-of-plane z-direction (ZD). The elasticity modulus along MD is typically two times the magnitude of CD while the ZD direction can be around 100 times lower compared to MD. The degree of anisotropy between the in-plane directions can be reduced by controlling the fiber direction, however, the large anisotropy between the in-plane and out-of-plane direction remains and this is one of the prime characteristics of paperboard.

Paperboard models exist on different scales and they can be divided into fiber network scale models, where individual fibers are modeled, and continuum scale models in which the fiber network is approximated as a homogeneous continuum, cf. the review article by Simon [1]. The individual fibers in a fiber network can be modeled using beam elements. This idea was presented in [2] for dry fibers and further developed in [3] where the bonding between fibers were modeled using contact mechanics. In [4] cohesive zones were used to more accurately account for fiber-fiber bonding. Another approach was presented in [5] where the end points of fibers and the fiber bonds were modeled as particles using the discrete element method (DEM). In [6], the finite element method was used to model individual fibers with solid elements which requires more computational effort compared to the beam approach but is important when studying the response in the stacking direction of fibers. While network models can be useful in order to tailor the material properties during the production phase, they are not suitable for large-scale applications, such as converting processes e.g. creasing and forming, which require computationally efficient continuum models.

The application of interest in the current work is the converting process which involves creasing and folding. Creasing is a process in which the material is locally deformed along predefined lines in order to guide the upcoming forming and create stable folds, cf. [7]. Creasing followed by folding has been simulated in the works of Huang et al. [8, 9] and Beex et al. [10, 11]. In these works, the in-plane behavior of paperboard was modeled with relatively simple constitutive models using small strain theory while the out-of-plane deformation, associated with large deformation and delamination, was modeled by cohesive interfaces. A challenge in this approach is to identify the location of the cohesive interfaces, which is a complex and important task in, for instance, 3D-rotational creasing see [12]. Another method for modeling creased lines was developed in Giampieri et al. [13, 14] where an interface element, placed between two shell elements, were tailored to capture the response during folding.

An alternative continuum scale approach is to model paperboard using large strain theory where the complex out-of-plane deformation is included in the continuum constitutive model. Such models are typically based on thermodynamics with an anisotropic yield surface, see e.g. Xia et al. [15]. In this class of models, the evolution laws are able to account for irreversible deformation in both the in-plane and out-of-plane directions. One model within this category were developed by Li et al. in [16, 17] which was used to simulate a cylindrical compression test. Another anisotropic large strain elasto-plastic model was developed in Borgqvist et al. [12] where line-creasing was considered. This

model was later utilized in Borgqvist et al. [18] to study the short span compression test and folding of uncreased paperboard. In addition, the model was combined with a solid-shell element in [19] where the forming sequence to produce a package was simulated. Furthermore, in Robertsson et al. [20] the model developed by Borgqvist was extended to include viscoelasticity and viscoplasticity to model the experimentally observed rate-dependency of paperboard. For materials that share characteristics with paperboard, notable works include the anisotropic viscoelasto-viscoplastic model for pressboard by Tjanjanto et al. [21] and the large strain elasto-plastic model by Harryson et al. [22] for corrugated board. While models accounting for large strains have considered creasing and folding separately, e.g. [12, 18], no continuum model of this type has been able to obtain a realistic response during creasing followed by folding. As this process is the basis for packaging forming, this will be addressed in current work.

In the current work, continuum damage modeling (CDM) is adopted to model the softening response during creasing and subsequent folding. CDM was originally introduced by Kachanov [23] and later formalized by, for instance, Lemaitre [24]. The continuum damage concept has been used to model the in-plane deformation of paperboard in [25, 26]. In our model, a single damage variable is introduced since shearing is assumed to be responsible for the delamination process and the local material failure. The dissipated energy due to out-of-plane shearing drives the damage evolution. The proposed framework shares characteristics with the ductile damage model presented in [27]. The damage model is calibrated against creasing and folding experiments. A simple scaling method is proposed in order to mitigate the mesh dependency caused by the damage evolution. In the constitutive driver a staggered approach is utilized in the sense that damage evolution is applied after the elasto-plastic response has been calculated.

The article is structured as follows. In section 2, the overall framework together with the specific modeling approach for paperboard is presented. In section 3.1, the line-creasing and subsequent line-folding is simulated and compared to simulations without damage. Furthermore, a mesh study is performed using the proposed scaling method. In section 3.2, an illustrative 3D example is simulated where paperboard is creased by two plates and folded to resemble the edge of a package.

## 2 Method and material

### 2.1 Modeling base

The model is described in the spatial configuration with the dissipation inequality on the form,

$$\mathcal{D} = \boldsymbol{\tau} : \mathbf{d} - \dot{\Psi} \geq 0, \quad (1)$$

where  $\boldsymbol{\tau}$  is the Kirchhoff stress tensor and  $\mathbf{d} = \text{sym}(\dot{\mathbf{F}}\mathbf{F}^{-1})$  is the symmetric part of the spatial velocity gradient. A multiplicative split of the deformation gradient is assumed  $\mathbf{F} = \mathbf{F}^e\mathbf{F}^p$  where  $\mathbf{F}^e$  and  $\mathbf{F}^p$  are the elastic and plastic contributions, respectively. The Helmholtz free energy is postulated as,

$$\Psi = (1 - \alpha)\Psi_0 \quad \text{with} \quad \Psi_0 = \Psi_0(\mathbf{b}^e, \mathbf{m}^{(i)}, \kappa^{(\nu)}) = \Psi_0^e(\mathbf{b}^e, \mathbf{m}^{(i)}) + \Psi_0^p(\kappa^{(\nu)}), \quad (2)$$

where  $\alpha$  models isotropic damage and  $\kappa^{(\nu)}$  with  $\nu = \{1, \dots, 12\}$  are the internal hardening variables. The state variables that defines the elastic contribution in (2) is the elastic finger tensor  $\mathbf{b}^e = \mathbf{F}^e\mathbf{F}^{eT}$

and the structural tensors  $\mathbf{m}^{(i)}$ , introduced as

$$\mathbf{m}^{(1)} = \mathbf{v}^{(1)} \otimes \mathbf{v}^{(1)}, \quad \mathbf{m}^{(2)} = \mathbf{v}^{(2)} \otimes \mathbf{v}^{(2)} \quad \text{and} \quad \mathbf{m}^{(3)} = \mathbf{n}^{(3)} \otimes \mathbf{n}^{(3)}, \quad (3)$$

where  $\mathbf{v}^{(1)}$  and  $\mathbf{v}^{(2)}$  are the in-plane characteristic directions of paperboard in the spatial configuration, i.e. the machine direction (MD) and the cross direction (CD), while  $\mathbf{n}^{(3)}$  is the characteristic out-of-plane (ZD) direction. The  $\mathbf{n}^{(3)}$  direction is defined to be perpendicular to the in-plane directions such that  $\mathbf{n}^{(3)} = \mathbf{v}^{(1)} \times \mathbf{v}^{(2)}$  holds. The evolution of the in-plane directional vectors are modeled to follow the elastic part of the deformation gradient,  $\mathbf{v}^{(1)} = \mathbf{F}^e \mathbf{v}_0^{(1)}$  and  $\mathbf{v}^{(2)} = \mathbf{F}^e \mathbf{v}_0^{(2)}$ , where  $\mathbf{v}_0^{(1)}$  and  $\mathbf{v}_0^{(2)}$  are the characteristic directions in the undeformed configuration.

The symmetric velocity gradient is additively separated into  $\mathbf{d} = \mathbf{d}^e + \mathbf{d}^p$  where  $\mathbf{d}^e = \text{sym}(\dot{\mathbf{F}}^e \mathbf{F}^{e-1})$  and  $\mathbf{d}^p = \text{sym}(\mathbf{F}^e \dot{\mathbf{F}}^p \mathbf{F}^{p-1} \mathbf{F}^{e-1})$  are the elastic and plastic parts, cf. [12]. With this split, the dissipation (1) becomes

$$\mathcal{D} = \underbrace{\boldsymbol{\tau} : \mathbf{d}^e}_{=\mathcal{D}^e} - (1 - \alpha) \dot{\Psi}_0^e + \boldsymbol{\tau} : \mathbf{d}^p - (1 - \alpha) \dot{\Psi}_0^p + \Psi_0 \dot{\alpha} \geq 0. \quad (4)$$

From argument by Coleman and Gurtin [28] we assume  $\mathcal{D}^e = 0$  such that  $\boldsymbol{\tau} = (1 - \alpha) \boldsymbol{\tau}_0$  with

$$\boldsymbol{\tau}_0 = 2 \left( \frac{\partial \Psi_0^e}{\partial \mathbf{b}^e} \mathbf{b}^e + \frac{\partial \Psi_0^e}{\partial \mathbf{m}^{(1)}} \mathbf{m}^{(1)} + \frac{\partial \Psi_0^e}{\partial \mathbf{m}^{(2)}} \mathbf{m}^{(2)} - \mathbf{m}^{(3)} \frac{\partial \Psi_0^e}{\partial \mathbf{m}^{(3)}} + \left( \frac{\partial \Psi_0^e}{\partial \mathbf{m}^{(3)}} : \mathbf{m}^{(3)} \right) \mathbf{I} \right), \quad (5)$$

which coincides with the Kirchhoff stress,  $\boldsymbol{\tau}_0$ , in [18]. The remaining part of the dissipation in (4) reads,

$$\mathcal{D} = (1 - \alpha) \hat{\mathcal{D}} + A \dot{\alpha} \geq 0 \quad \text{with} \quad \hat{\mathcal{D}} = \boldsymbol{\tau}_0 : \mathbf{d}^p - \sum_{\nu=1}^{12} K^{(\nu)} \dot{\kappa}^{(\nu)}, \quad (6)$$

where the conjugated forces are given by

$$K^{(\nu)} = \frac{\partial \Psi_0^p}{\partial \kappa^{(\nu)}} \quad \text{and} \quad A = -\frac{\partial \Psi}{\partial \alpha} = \Psi_0. \quad (7)$$

Associated plasticity is assumed which renders the evolution laws

$$\mathbf{d}^p = \dot{\lambda} \frac{\partial f}{\partial \boldsymbol{\tau}_0} \quad \text{and} \quad \dot{\kappa}^{(\nu)} = -\dot{\lambda} \frac{\partial f}{\partial K^{(\nu)}}, \quad (8)$$

where  $f$  is the yield surface and  $\dot{\lambda}$  is the plastic multiplier. The yield surface, which together with the Karush-Kuhn-Tucker (KKT) conditions,

$$f \leq 0, \quad \dot{\lambda} \geq 0 \quad \text{and} \quad f \dot{\lambda} = 0, \quad (9)$$

governs the evolution of plasticity. The undamaged part of the Kirchhoff stress, similar to [18], is used for defining the yield surface, i.e.

$$f = \sum_{\nu=1}^{12} \mathcal{X}^{(\nu)} \Omega_\nu^{2k} - 1 \quad \text{with} \quad \Omega_\nu = \frac{\boldsymbol{\tau}_0 : \mathbf{n}_s^{(\nu)}}{K_0^{(\nu)} + K^{(\nu)}} \quad \text{and} \quad \mathcal{X}^{(\nu)} = \begin{cases} 1 & \text{if } \boldsymbol{\tau}_0 : \mathbf{n}_s^{(\nu)} > 0 \\ 0 & \text{otherwise} \end{cases}, \quad (10)$$

where  $\mathbf{n}_s^{(\nu)}$  projects the stress tensor on the subspace  $\nu$  while  $K_0^{(\nu)}$  is the initial distance to the yield surface and  $k$  is a material parameter that controls the smoothness of the yield surface. Using the evolution equations (8), the yield surface (10) and assuming elasto-plastic loading, i.e.  $f = 0$ , the dissipation in (6), excluding the damaged part, can be written as

$$\hat{\mathcal{D}} = \sum_{\nu=1}^{12} \hat{\mathcal{D}}_{\nu} \quad \text{with} \quad \hat{\mathcal{D}}_{\nu} = K_0^{(\nu)} \dot{k}^{(\nu)}. \quad (11)$$

## 2.2 Evolution of damage

The evolution law for the damage variable is inspired by Larsson et al. [27] who postulated the damage evolution in a similar manner to plasticity theory, i.e.

$$\dot{\alpha} = \dot{\mu} \frac{\partial \Phi}{\partial A_T}, \quad (12)$$

where  $\Phi$  is a potential function and  $\dot{\mu}$  a Lagrangian multiplier. The dissipated energy  $A_T$  is defined as,

$$A_T = \int_0^t \sum_{n \in P} \hat{\mathcal{D}}_n dt = \sum_{n \in P} \int_0^t \hat{\mathcal{D}}_n dt = \sum_{n \in P} A_T^{(n)} \quad \text{with} \quad A_T^{(n)} = \int_0^t \hat{\mathcal{D}}_n dt, \quad (13)$$

where  $P$  is a subset of the full summation in (11) and  $t$  being the current pseudo time. The potential  $\Phi$  in (12) is chosen as,

$$\Phi = \sum_{n \in P} \left[ A_T^{(n)} - (1 + c_n \alpha) A_c^{(n)} \right], \quad (14)$$

where the material parameters  $c_n$  control the damage evolution. The critical pseudo time  $t_c$  for the initiation of damage is reached when the following criteria is fulfilled,

$$1 = \sum_{n \in P} \beta_n A_c^{(n)} \quad \text{with} \quad A_c^{(n)} = \int_0^{t_c} \hat{\mathcal{D}}_n dt, \quad (15)$$

where  $\beta_n$  are material parameters. Similar to plasticity theory, the KKT conditions are assumed to control the onset of the damage evolution,

$$\Phi \leq 0, \quad \dot{\mu} \geq 0 \quad \text{and} \quad \Phi \dot{\mu} = 0. \quad (16)$$

In conclusion, when  $t > t_c$ , the criteria  $\Phi = 0$  holds and the damage becomes,

$$\alpha = \frac{\sum_{n \in P} (A_T^{(n)} - A_c^{(n)})}{\sum_{n \in P} c_n A_c^{(n)}}. \quad (17)$$

The model above fulfills the dissipation inequality (6) since  $\Psi_0 \geq 0$  and  $\dot{\alpha} \propto \sum_{n \in P} \hat{\mathcal{D}}_n$  which follows from (13). The model in (14) and (15) with the material parameters  $\beta_n$  and  $c_n$  allow for a flexible format when combined with the anisotropic yield surface in (10). As such, the contribution from the plastic dissipation for different modes of deformation can be combined in the expression for the damage evaluation. For instance, the out-of-plane deformations associated with delamination can be influenced by e.g. debonding and fracture of fibers during in-plane tension, cf. [29].

### 2.3 Specific elastoplastic model

The undamaged part of the elastic energy,  $\Psi_0^e$ , is chosen in accordance with [18] as,

$$\begin{aligned} \Psi_0^e = & E_1(I_{11} + I_{11}^{-1} - 2) + E_2(I_{12} + I_{12}^{-1} - 2) + E_4(I_{11} + I_{12} + I_{23}^{-1} - 3) \\ & + H E_3(I_{13} + I_{13}^{-1} - 2) + (1 - H)E_6 \left[ I_{13}^2 + \frac{1}{E_7} e^{-E_7(I_{13}^2 - 1)} - 2 \right] \\ & + E_5(I_{11}I_{12}I_{13} - J^e) \end{aligned} \quad (18)$$

where  $J^e = \det(\mathbf{F}^e)$  and  $H$  is the Heaviside function with the properties,  $H = 1$  if  $I_{13} \geq 1$  otherwise zero. The invariants are defined as,

$$\left\{ \begin{array}{l} I_{11} = |\mathbf{v}^{(1)}| = \sqrt{\mathbf{m}^{(1)} : \mathbf{I}} \\ I_{12} = |\mathbf{v}^{(2)}| = \sqrt{\mathbf{m}^{(2)} : \mathbf{I}} \end{array} \right. \quad \text{and} \quad \left\{ \begin{array}{l} I_{13} = |\mathbf{F}^e \mathbf{n}_0^{(3)}| = \frac{1}{J^e} \sqrt{\mathbf{m}^{(3)} : \mathbf{b}^e \mathbf{b}^e} \\ I_{23} = |\mathbf{n}^{(3)}| = \sqrt{\mathbf{m}^{(3)} : \mathbf{I}} \end{array} \right., \quad (19)$$

with  $|\bullet|$  being the Euclidean norm. The invariants  $I_{11}$ ,  $I_{12}$  and  $I_{13}$  are associated with the elastic stretch along MD, CD and ZD, respectively, while  $I_{23}$  is associated with the area spanned by the in-plane characteristic directions,  $\mathbf{v}^{(1)}$  and  $\mathbf{v}^{(2)}$ . Use of the elastic potential (18) in (5) provides the undamaged part of the Kirchhoff stress,

$$\boldsymbol{\tau}_0 = P_1 \mathbf{m}^{(1)} + P_2 \mathbf{m}^{(2)} + P_3 \mathbf{m}^{(3)} + P_4 \mathbf{I} + J^{e-2} P_5 \mathbf{b}^e \mathbf{m}^{(3)} \mathbf{b}^e, \quad (20)$$

where the scalar functions are defined as

$$\left\{ \begin{array}{l} P_1 = E_1(I_{11}^{-1} - I_{11}^{-3}) + E_4 I_{11}^{-1} + E_5 I_{12} I_{13} I_{11}^{-1} \\ P_2 = E_2(I_{12}^{-1} - I_{12}^{-3}) + E_4 I_{12}^{-1} + E_5 I_{11} I_{13} I_{12}^{-1} \\ P_3 = E_4 I_{23}^{-3} \\ P_4 = -E_5 J^e - E_4 I_{23}^{-1} \\ P_5 = H E_3 (I_{13}^{-1} - I_{13}^{-3}) + 2(1 - H) E_6 \left[ 1 - e^{-E_7(I_{13}^2 - 1)} \right] + E_5 I_{11} I_{12} I_{13}^{-1}. \end{array} \right. \quad (21)$$

The 12 projections  $\mathbf{n}_s^{(\nu)}$  that defines the yield surface are given as,

$$\begin{aligned} \mathbf{n}_s^{(1)} &= \frac{1}{\sqrt{1+\nu_{12}^2}} \left( \bar{\mathbf{v}}^{(1)} \otimes \bar{\mathbf{v}}^{(1)} - \nu_{12} \bar{\mathbf{v}}^{(2)} \otimes \bar{\mathbf{v}}^{(2)} \right), & \mathbf{n}_s^{(2)} &= \frac{1}{\sqrt{1+\nu_{21}^2}} \left( \bar{\mathbf{v}}^{(2)} \otimes \bar{\mathbf{v}}^{(2)} - \nu_{21} \bar{\mathbf{v}}^{(1)} \otimes \bar{\mathbf{v}}^{(1)} \right) \\ \mathbf{n}_s^{(4)} &= -\bar{\mathbf{v}}^{(1)} \otimes \bar{\mathbf{v}}^{(1)}, & \mathbf{n}_s^{(5)} &= -\bar{\mathbf{v}}^{(2)} \otimes \bar{\mathbf{v}}^{(2)} \\ \mathbf{n}_s^{(3)} &= \frac{1}{\sqrt{2}} \left( \bar{\mathbf{v}}^{(1)} \otimes \bar{\mathbf{v}}^{(2)} + \bar{\mathbf{v}}^{(2)} \otimes \bar{\mathbf{v}}^{(1)} \right), & \mathbf{n}_s^{(6)} &= -\frac{1}{\sqrt{2}} \left( \bar{\mathbf{v}}^{(1)} \otimes \bar{\mathbf{v}}^{(2)} + \bar{\mathbf{v}}^{(2)} \otimes \bar{\mathbf{v}}^{(1)} \right) \\ \mathbf{n}_s^{(7)} &= -\bar{\mathbf{v}}^{(3)} \otimes \bar{\mathbf{v}}^{(3)}, & \mathbf{n}_s^{(8)} &= \bar{\mathbf{v}}^{(3)} \otimes \bar{\mathbf{v}}^{(3)} \\ \mathbf{n}_s^{(9)} &= \frac{1}{\sqrt{1+m^2}} \left( m \bar{\mathbf{v}}^{(3)} \otimes \bar{\mathbf{v}}^{(3)} + \bar{\mathbf{v}}^{(1)} \otimes \bar{\mathbf{v}}^{(3)} \right), & \mathbf{n}_s^{(10)} &= \frac{1}{\sqrt{1+m^2}} \left( m \bar{\mathbf{v}}^{(3)} \otimes \bar{\mathbf{v}}^{(3)} - \bar{\mathbf{v}}^{(1)} \otimes \bar{\mathbf{v}}^{(3)} \right) \\ \mathbf{n}_s^{(11)} &= \frac{1}{\sqrt{1+m^2}} \left( m \bar{\mathbf{v}}^{(3)} \otimes \bar{\mathbf{v}}^{(3)} + \bar{\mathbf{v}}^{(2)} \otimes \bar{\mathbf{v}}^{(3)} \right), & \mathbf{n}_s^{(12)} &= \frac{1}{\sqrt{1+m^2}} \left( m \bar{\mathbf{v}}^{(3)} \otimes \bar{\mathbf{v}}^{(3)} - \bar{\mathbf{v}}^{(2)} \otimes \bar{\mathbf{v}}^{(3)} \right) \end{aligned} \quad (22)$$

where the normalized vectors  $\bar{\mathbf{v}}^{(1)} = \mathbf{v}^{(1)}/|\mathbf{v}^{(1)}|$ ,  $\bar{\mathbf{v}}^{(2)} = \mathbf{v}^{(2)}/|\mathbf{v}^{(2)}|$  and  $\bar{\mathbf{v}}^{(3)} = \mathbf{n}^{(3)}/|\mathbf{n}^{(3)}|$  were introduced. The parameter  $m$  in  $\mathbf{n}_s^{(\nu)}$  governs the plastic coupling between out-of-plane compression

and shear while  $\nu_{12}$  and  $\nu_{21}$  are the in-plane Poisson's numbers. Snapshots of projections for the yield function are shown in Fig. 1.

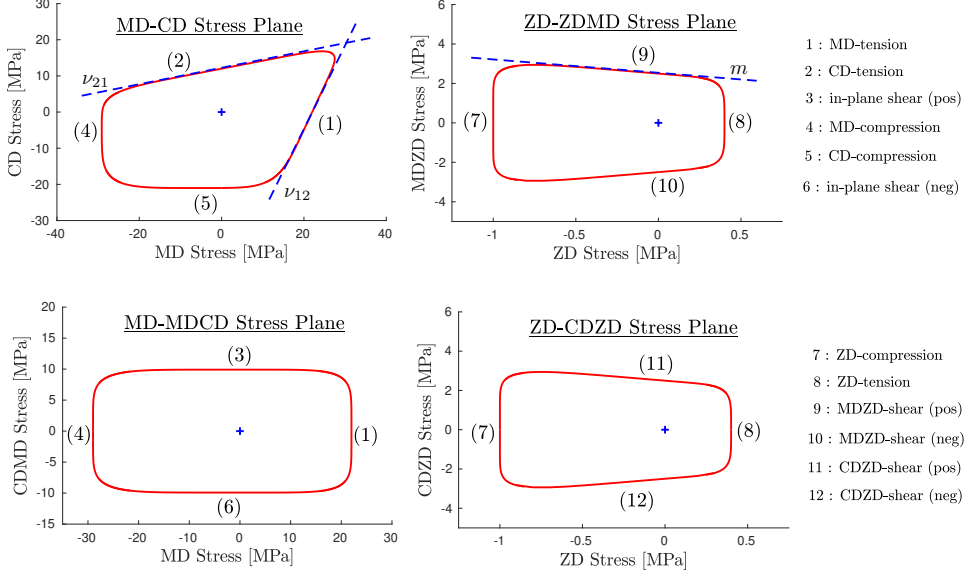


Figure 1: Projections  $\bar{\mathbf{v}}^{(i)} \cdot \boldsymbol{\tau}_0 \cdot \bar{\mathbf{v}}^{(j)}$  of the yield surface  $f = 0$  along different planes with notation MD =  $\bar{\mathbf{v}}^{(1)} \cdot \boldsymbol{\tau}_0 \cdot \bar{\mathbf{v}}^{(1)}$ , CD =  $\bar{\mathbf{v}}^{(2)} \cdot \boldsymbol{\tau}_0 \cdot \bar{\mathbf{v}}^{(2)}$ , ZD =  $\bar{\mathbf{v}}^{(3)} \cdot \boldsymbol{\tau}_0 \cdot \bar{\mathbf{v}}^{(3)}$ , ZDMD =  $\bar{\mathbf{v}}^{(3)} \cdot \boldsymbol{\tau}_0 \cdot \bar{\mathbf{v}}^{(1)}$ , ZDZD =  $\bar{\mathbf{v}}^{(3)} \cdot \boldsymbol{\tau}_0 \cdot \bar{\mathbf{v}}^{(2)}$  and MDZD =  $\bar{\mathbf{v}}^{(1)} \cdot \boldsymbol{\tau}_0 \cdot \bar{\mathbf{v}}^{(2)}$

Following [18], the plastic spin tensor is chosen as,

$$\boldsymbol{\omega}^p = \text{skew} \left( \sum_{\nu=1}^{12} \dot{\lambda} \Lambda_{\nu} \mathbf{n}_s^{(\nu)} \right) \quad \text{with} \quad \Lambda_{\nu} = \frac{2k \mathcal{X}^{(\nu)}}{K_0^{(\nu)} + K^{(\nu)}} \left( \frac{\boldsymbol{\tau}_0 : \mathbf{n}_s^{(\nu)}}{K_0^{(\nu)} + K^{(\nu)}} \right)^{2k-1}, \quad (23)$$

which is the skew-symmetric counterpart to  $\mathbf{d}^p = \text{sym}(\sum_{\nu=1}^{12} \dot{\lambda} \Lambda_{\nu} \mathbf{n}_s^{(\nu)})$  obtained from (8 a), (9) and (10). Using the definition  $\dot{\mathbf{F}}^p = \mathbf{F}^{e-1} \dot{\mathbf{l}}^p \mathbf{F}^e \mathbf{F}^p$  and  $\dot{\mathbf{l}}^p = \mathbf{d}^p + \boldsymbol{\omega}^p$  combined with (8), (10) and (23) results in the elasto-plastic evolution equations,

$$\begin{cases} \dot{\mathbf{F}}^p = \sum_{\nu=1}^{12} \Lambda_{\nu} \dot{\lambda} \mathbf{F}^p \mathbf{F}^{-1} \mathbf{n}_s^{(\nu)} \mathbf{F} \\ \dot{\kappa}^{(\nu)} = \dot{\lambda} \Lambda_{\nu} \frac{\boldsymbol{\tau}_0 : \mathbf{n}_s^{(\nu)}}{K_0^{(\nu)} + K^{(\nu)}} \end{cases}. \quad (24)$$

The specific format for the hardening  $K^{(\nu)}$  will be considered later on. In the numerical implementation, the system of equations in (24) is discretized using the Euler backward method and solved with the Newton-Raphson procedure to obtain the internal hardening variables  $\kappa^{(\nu)}$  and the plastic part of the deformation gradient  $\mathbf{F}^p$ .

## 2.4 Specific damage model

The motivation for introducing damage in the paperboard model is to capture the complex behavior of paperboard during creasing and subsequent folding. As the purpose of the creasing process is to weaken the material in specific zones, damage is needed to capture the material softening. The driving force for the damage evolution, cf. (17), is taken as the undamaged plastic dissipation associated with the out-of-plane shear deformation. This assumption implies that the subset  $P = \{9, 10, 11, 12\}$  governs the damage evolution such that (15) and (17) become,

$$\alpha = \frac{\sum_{n=9}^{12} (A_T^{(n)} - A_c^{(n)})}{\sum_{n=9}^{12} c_n A_c^{(n)}} \quad \text{and} \quad 1 = \sum_{n=9}^{12} \beta_n A_c^{(n)}. \quad (25)$$

The parameters  $c_n$  and  $\beta_n$  associated with out-of-plane shearing along MD,  $n \in \{9, 10\}$ , and CD,  $n \in \{11, 12\}$ , are calibrated against line creasing and folding when the MD, and CD direction respectively, are aligned with the creasing setup using a specific element area  $A_r^e$  as reference discretization. It is well known that softening response gives rise to a mesh dependence and requires a length scale to be introduced. For simplicity, the length scale is based on the finite element discretization. To mitigate the mesh dependency the damage material parameters are scaled as,

$$\beta_n = \begin{cases} \frac{A_{md}^e}{A_r^e} \beta_n^r, & n = \{9, 10\} \\ \frac{A_{cd}^e}{A_r^e} \beta_n^r, & n = \{11, 12\} \end{cases} \quad \text{and} \quad c_n = \begin{cases} \frac{A_{md}^e}{A_r^e} c_n^r, & n = \{9, 10\} \\ \frac{A_{cd}^e}{A_r^e} c_n^r, & n = \{11, 12\} \end{cases}, \quad (26)$$

where  $A_{md}^e$  and  $A_{cd}^e$  are projected areas along the MD-ZD and CD-ZD direction in the undeformed configuration. For an 8-node brick element, the areas are computed from,

$$A_{md}^e = \min_{i \in \{1, \dots, 6\}} \frac{A_i^e}{|\mathbf{v}_0^{(2)} \cdot \mathbf{n}_i|} \quad \text{and} \quad A_{cd}^e = \min_{i \in \{1, \dots, 6\}} \frac{A_i^e}{|\mathbf{v}_0^{(1)} \cdot \mathbf{n}_i|}, \quad (27)$$

where  $A_i^e$  are the six sides of the brick element with its corresponding normal directions  $\mathbf{n}_i$ . Notably, the scaling (26) is very simple to implement as it is explicit.

## 2.5 Material parameters

The single ply paperboard considered in [18] is also used in the current work, i.e. thickness and density are 0.39 mm and 788 kg/m<sup>3</sup>, respectively. The elastic parameters in (18) are tabulated in Tab. 1.

$E_1$ [MPa]	$E_2$ [MPa]	$E_3$ [MPa]	$E_4$ [MPa]	$E_5$ [MPa]	$E_6$ [MPa]	$E_7$ [-]
1690	292	28.4	1330	78.0	0.365	11.5

Table 1: Elastic parameters.

Following [30],  $E_1$ ,  $E_2$ ,  $E_4$  and  $E_5$  are obtained from uniaxial tension experiments along the MD, CD and  $45^\circ$  directions by comparing the initial stiffness tensor resulting from (20) with the initial orthotropic stiffness tensor. The in-plane shear modulus is computed from Lekhnitskii [31] and  $\sqrt{\nu_{12}\nu_{21}} = 0.30$  is used for the in-plane Poisson's ratios that was obtained by Baum et al. [32] for a range of paperboards. With this we obtain  $\nu_{12} = 0.46$  and  $\nu_{21} = 0.19$ . The elastic parameter  $E_3$  is estimated from the initial stiffness during out-of-plane tension while  $E_6$  and  $E_7$  are obtained from unloading during out-of-plane compression.

The plastic hardening variables in (10) are modeled by,

$$K^{(\nu)} = \begin{cases} a_\nu \ln(b_\nu \kappa^{(\nu)} + 1), & \nu = \{1, 2, 3, 6\} \\ a_\nu \kappa^{(\nu)}, & \nu = 7 \\ 0, & \text{otherwise} \end{cases}, \quad (28)$$

where the hardening parameters  $a_\nu$  and  $b_\nu$  together with the initial yield distances  $K_0^{(\nu)}$  are tabulated in Tab. 2.

Subsurface index, $\nu$	Initial yield, $K_0^{(\nu)}$ [MPa]	Hardening, $a_\nu$ [MPa]	Hardening, $b_\nu$ [-]
1	20.4	12.2	690
2	11.7	5.10	435
3	9.91	6.63	334
4	22.0	-	-
5	16.7	-	-
6	9.91	6.63	334
7	1.00	49.0	-
8	0.40	-	-
9	2.51	-	-
10	2.51	-	-
11	2.51	-	-
12	2.51	-	-

Table 2: Plastic parameters.

The hardening parameters for  $\nu = \{1, 2, 3, 6\}$  in (28) are calibrated against uniaxial tension along MD, CD and  $45^\circ$  while the hardening  $a_7$  and  $K_0^{(7)}$  are fitted to out-of-plane compression experiments. In-plane tension measurements along the MD and CD directions are compared to the calibrated model in Fig. 2.

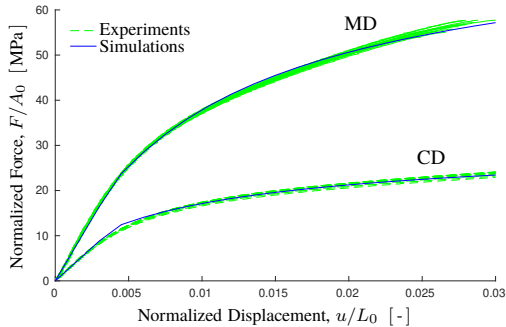


Figure 2: In-plane tension measurements along the MD and CD direction of paperboard.

The in-plane compression parameters,  $K_0^{(4)}$  and  $K_0^{(5)}$ , are estimated from the short-span compression test while the out-of-plane tension strength  $K_0^{(8)}$  is fitted to out-of-plane experiments. Due to lack of reliable experimental data, the out-of-plane shear strengths  $K_0^{(9)}$ ,  $K_0^{(10)}$ ,  $K_0^{(11)}$  and  $K_0^{(12)}$  has been calibrated against the force-displacement response during creasing. Similar to Borgqvist et al. [12], the exponent in the yield surface (10) is chosen as  $k = 3$  while the coupling parameter between out-of-plane shear and compression is estimated to be  $m = 0.7$  from Stenberg [33]. The damage parameters in (25) will be identified by comparing the model to creasing and folding experiments as discussed in next section.

## 3 Results and discussion

### 3.1 Line creasing and folding

To evaluate the response of the proposed model, we simulate the line-creasing set-up in [12] followed by line-folding. The geometry and boundary conditions for the creasing and folding steps are schematically outlined in Fig. 3. The paperboard sheet is 110 mm long with a width of 38 mm while having a thickness of 0.39 mm. Since the width of the sheet is large compared to the localized area of deformation, plane strain is assumed.

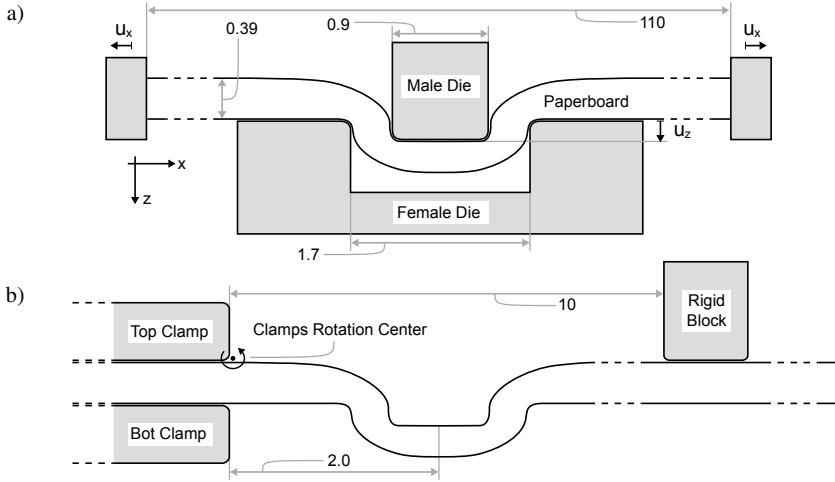


Figure 3: a) Schematics of the line creasing setup and b) the subsequent line folding procedure. The radius of the tools are  $R = 0.1$  mm, all dimensions in mm.

Prior to creasing, the displacement of the paperboard edges are prescribed  $u_x$  rendering an initial in-plane force of 57 N that mimics webtension. The paperboard is then creased by displacing a male die,  $u_z = 0.2$  mm, into a female groove, see Fig. 3a. After the webtension and dies are removed, the irreversible deformation of the material creates two localized shear-zones that acts like hinges.

The line-folding following creasing is initiated by two clamps compressing the paperboard sample such that the contact pressure becomes 0.2 MPa. Rotation of the paperboard strip is prevented by a rigid block which is placed at a distance of 10 mm from the clamps. The paperboard is then folded by prescribing the rotation of the top and bottom clamps as illustrated in Fig. 3b.

The simulation is performed using the commercial finite element software Abaqus Standard with the material model implemented as a Umat subroutine, cf. [34]. The paperboard is discretized with linear continuum brick elements where the reference element size, at the critical region close to the creased zone, is 0.07 mm in-plane and 0.0156 mm through the thickness, i.e.  $A_r^e = 0.0011$  mm<sup>2</sup>. Finite deformation and quasi-static conditions are assumed and the problem is solved using implicit time integration. The tools are modeled as rigid bodies. Contact between tools and paperboard are modeled using a tangential penalty formulation with friction coefficient  $\mu = 0.4$ . The maximum amount of damage allowed in a Gauss point is  $\alpha_{\max} = 0.96$ , whereafter the damage evolution is terminated.

The experiments and simulations are performed with the setup aligned in the MD and CD direction. During line-folding, the bending force at the rigid block and the rotation angle is monitored. Similarly, during creasing the male die force and displacement is monitored. For both operations, the experimentally measured response is compared to the simulation using the proposed model with and without damage. The damage parameters in (25) are calibrated against line creasing and folding using the reference element discretization,  $A_r^e = 0.0011$  mm<sup>2</sup>, and they are tabulated in Tab. 3.

Subsurface $n$	9	10	11	12
$c_n^r$ [-]	8.0	8.0	9.0	9.0
$\beta_n^r$ [MPa <sup>-1</sup> ]	2.85	2.85	3.98	3.98

Table 3: Damage parameters.

The results during line-creasing and line-folding are presented in Fig. 4-5.

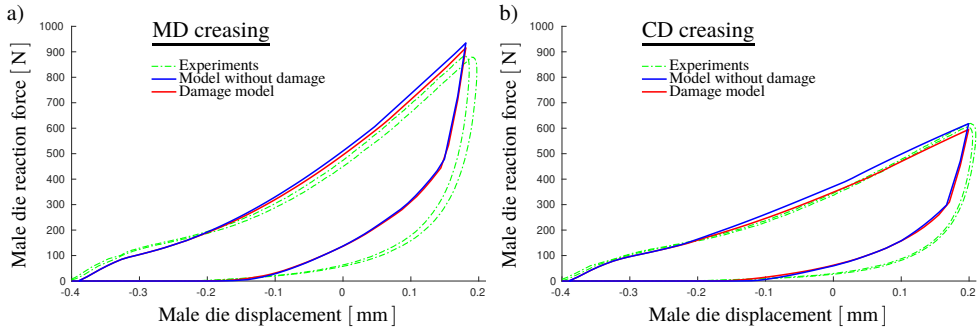


Figure 4: Reaction force during creasing when the experimental set-up is aligned with a) MD direction and b) CD direction.

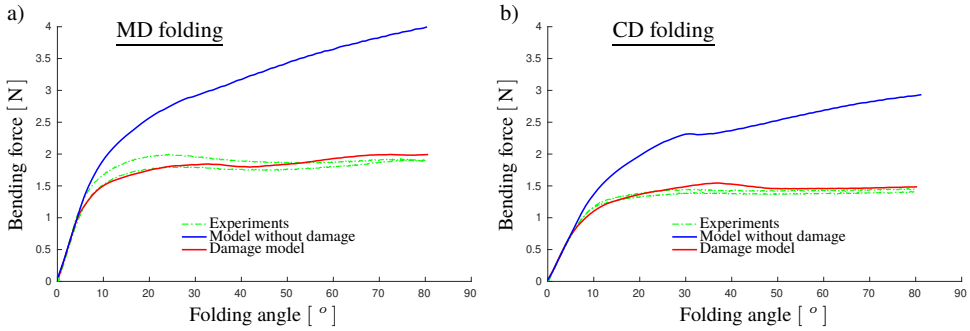


Figure 5: Folding curve after creasing when the experimental set-up is aligned with a) MD direction and b) CD direction.

As seen in Fig. 4, the difference between the simulations with and without damage during creasing is minuscule. During folding, see Fig. 5, the damage model predicts a plateau in the mechanical response at approximately 20° which is consistent with the measurements. This contrasts the model

without damage which is unable to accurately predict the folding response as the force grows with increasing folding angle and does not reach the plateau that is experimentally observed.

The damage distribution after creasing and after creasing and folding is shown in Fig. 6. It is observed that, although the damage generated during creasing is relatively large, see Fig. 4a, the influence on the mechanical response is negligible. Furthermore, in Fig. 6b, the damage variable during folding has reached its maximum level for several elements which is expected for the creation of hinges. The increase in damage at the two hinges allows for a flexible response where the middle part of the crease deforms plastically from out-of-plane tension, which for simplicity is modeled as ideal plastic.

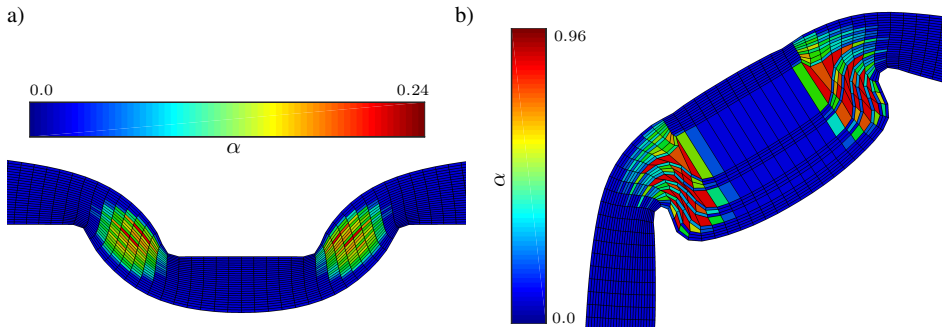


Figure 6: Damage distribution and local deformation during, a) creasing and subsequent b) folding at  $90^\circ$ .

In Fig. 7, the simulated deformation after folding with and without damage is compared to a representative experimental deformation pattern. Close to the hinges, the simulation with damage evolution included predicts a more flexible response than the simulation without damage. This is consistent with the experimental finding in Fig. 7c. In addition, the total plastic out-of-plane shear, defined as  $(\kappa_s)^2 = (\kappa^{(9)})^2 + (\kappa^{(10)})^2 + (\kappa^{(11)})^2 + (\kappa^{(12)})^2$ , is shown in Fig. 7a and b where it is concluded that the shear strain is concentrated at the hinges in both simulations.

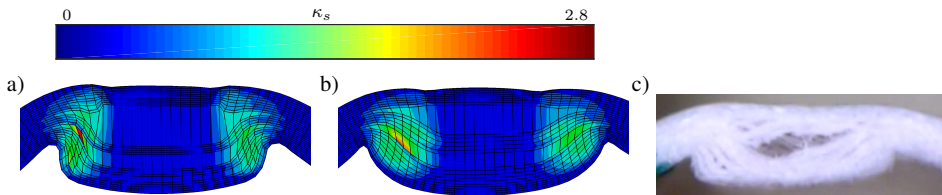


Figure 7: Shape of the hinges after the folding procedure with a) the damage framework and b) without. A representative image of the hinge c) from the experiment.

Ductile damage models are, due to the softening, known to be plagued by inherent mesh dependency. Based on numerical experiments, the damage parameters are proposed to be scaled according

to (26) where a rectangular reference area of  $A_r^e = 0.0011 \text{ mm}^2$  was used close to the critical region. A mesh size sensitivity study is performed in Fig. 8 where the MD direction is aligned with the experimental setup and the ratio between the element thickness and length is kept fixed. The considered range of mesh sizes  $A^e/A_r^e$  are separated into two figures for visibility. As seen in Fig. 8, the refinement of the mesh has a large impact on the response if the scaling is omitted. In contrast, the results using the proposed scaling strategy (26) is in close agreement with the simulation of the reference mesh for the considered range of  $A^e/A_r^e$ .

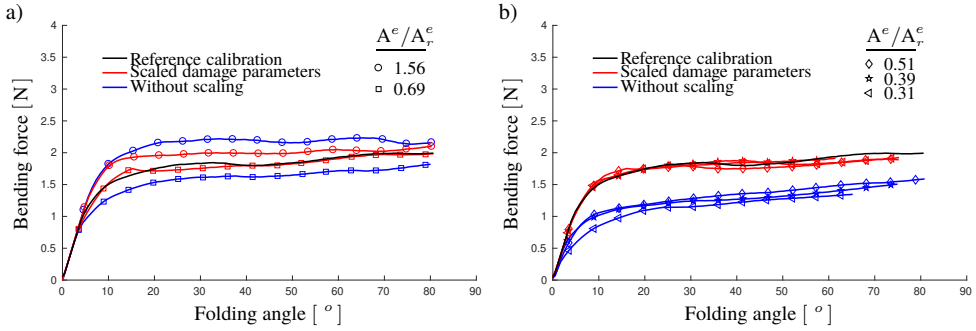


Figure 8: Mesh size sensitivity study. The element size ratio  $A^e/A_r^e$  for constant aspect ratio is plotted against the folding response.

In Fig. 9, the deformation is shown at the folding angle  $75^\circ$  for three mesh sizes using the scaling approach. The deformation and damage distribution appears similar with a concentration of damage at the hinges and delamination at the middle part of the crease. While the deformation is similar, the amount of delamination is larger for the simulation with the finer mesh.

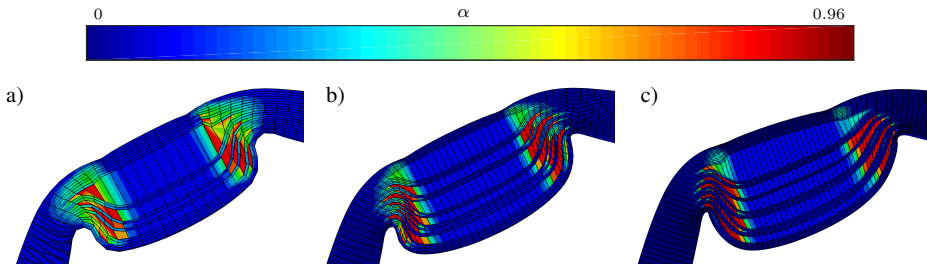


Figure 9: Deformed shape at an approximate folding angle of  $75^\circ$  using an element mesh size of a)  $A^e/A_r^e = 1.56$ , b)  $A^e/A_r^e = 0.51$  and c)  $A^e/A_r^e = 0.31$  with the proposed scaling method.

### 3.2 Creasing and folding of a package corner

To highlight the potential of the proposed model, an industrially important application is considered where a paperboard sheet is creased by two plates and folded to resemble the corner of a package.

The crease tools and paperboard sheet, of in-plane dimensions  $60 \times 60 \text{ mm}^2$  and thickness  $0.39 \text{ mm}$ , is shown in Fig. 10a. The paperboard is placed between a female and male die that has a horizontal, vertical and diagonal crease pattern, cf. Figs. 10b and c.

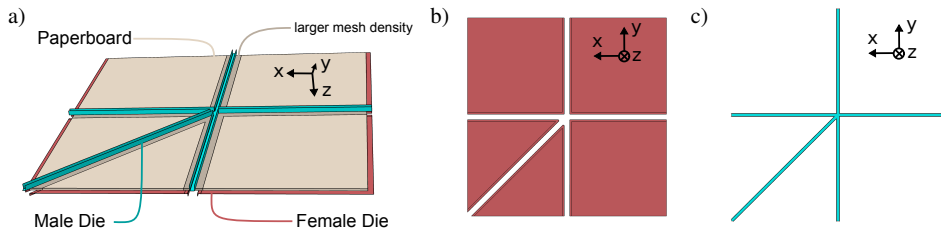


Figure 10: The parts a) in the plate creasing example. Top down view of b) the female groove and c) the male die.

Since the deformation will be localized in the vicinity of the crease bands, the paperboard is separated into element patches with different mesh densities and connected using the build-in tie constraint in Abaqus. With this approach, several elements are used in the thickness direction around the creased lines, as shown in Fig. 11a and c, while the remaining mesh consists of two elements in the thickness direction.

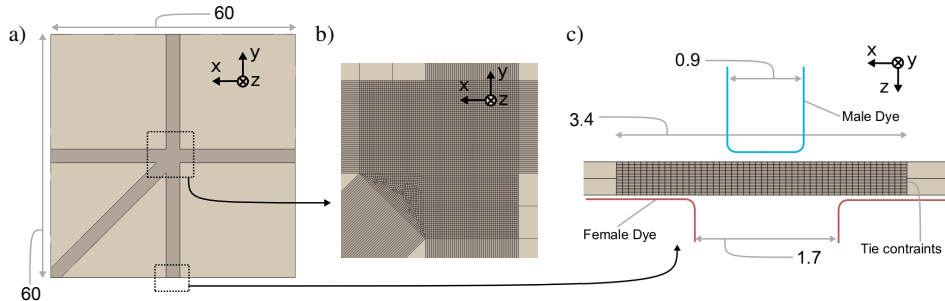


Figure 11: Top down view of the a) paperboard showing the high mesh density b) region. A cross section view c) at the vertical crease line, dimensions in mm.

As seen in Fig. 11c, the width of the male die and the female groove, at a cross section along the crease lines, are identical to the previous line-creasing setup, cf. Fig. 3a. In addition, the male die is displaced toward the female groove until a crease depth of  $u_z = 0.2 \text{ mm}$  is reached, i.e. the same crease depth as for the line-creasing example. The scaling in (26), (27) is used and the element size along the creased lines are  $0.035 \text{ mm}$  in thickness and  $0.07 \text{ mm}$  in width. In total, the paperboard is discretized with approximately 100000 continuum 8-node brick elements. The most critical region for the paperboard is at the intersection between the crease lines where the mesh density is increased

along the x-y direction as shown in Fig. 11b. The MD direction of the paperboard is aligned with the x-direction, see Fig. 11a, and before creasing is initiated an initial displacement along the sheet edges is applied such that the initial webtension in the x-direction becomes 57 N.

The solution procedure is similar to the line-creasing example, i.e. the quasi-static balance of linear momentum is solved using the implicit Abaqus Standard solver. The friction coefficient between the paperboard and the tools is  $\mu = 0.3$  while the maximum amount of damage is  $\alpha_{max} = 0.7$ .

After the creasing step, the folding phase which consists of three folding sequences is initiated. The procedure is shown in Fig. 12 where the first folding sequence consists of restricting the motion of the top left (not shown) and top right quadrant of the paperboard, by engaging clamping tools that compress the paperboard with a pressure of 0.2 MPa. In the first sequence, the rotation shown in Fig. 12a  $\rightarrow$  b is applied where the active blocks are highlighted in blue. In the second folding step, shown in Fig. 12b  $\rightarrow$  c, the lower rigid block is rotated to obtain a paperboard flap along the diagonally creased pattern. In the final sequence, Fig. 12c  $\rightarrow$  d, a rigid block is rotated to fold the paperboard flap and complete the structure of the package corner.

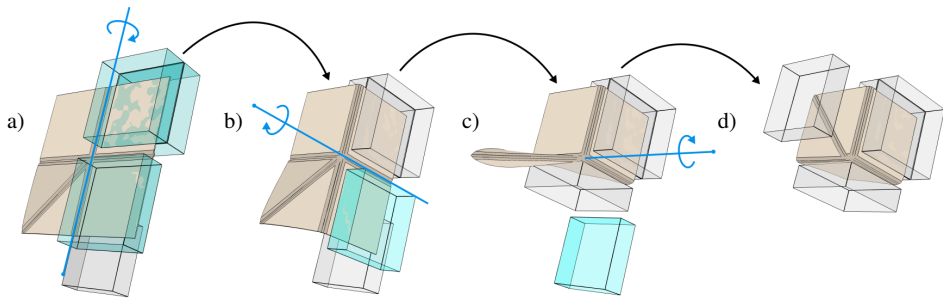


Figure 12: Folding procedure to form the package corner.

The deformation after creasing and folding is shown in Fig. 13a. The critical part of the package is at the vicinity of the corner. To highlight the deformation pattern, Fig. 13 shows the damage variable when cutting out the corner of the package.

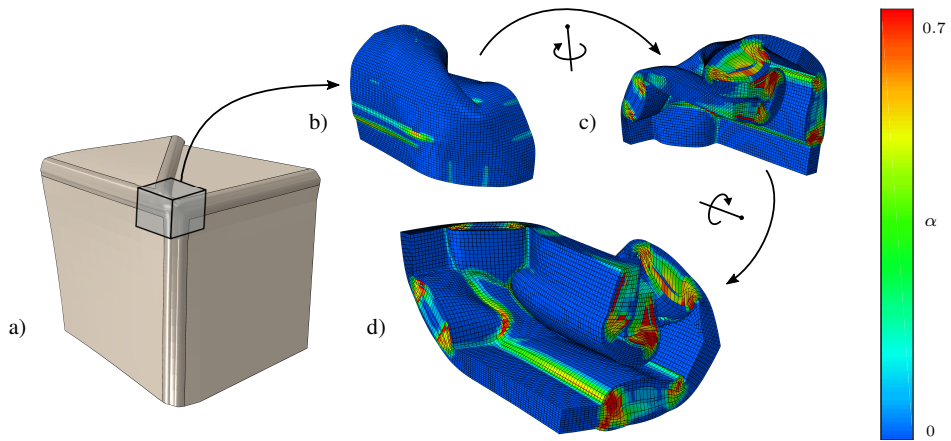


Figure 13: a) Final deformation of the package. b) Cutting out the corner of the package followed by two rotations showing the inside perspectives, c) and d), of the package corner with corresponding damage distribution.

In Fig. 14, the cut-out corner in Fig. 13d is tracked throughout the deformation history. It is observed that the deformed pattern after the second folding step is highly complex and coincides with the creation of the flap in Fig. 12c. In addition, the amount of damage is localized around the creased regions which is expected for successful folding.

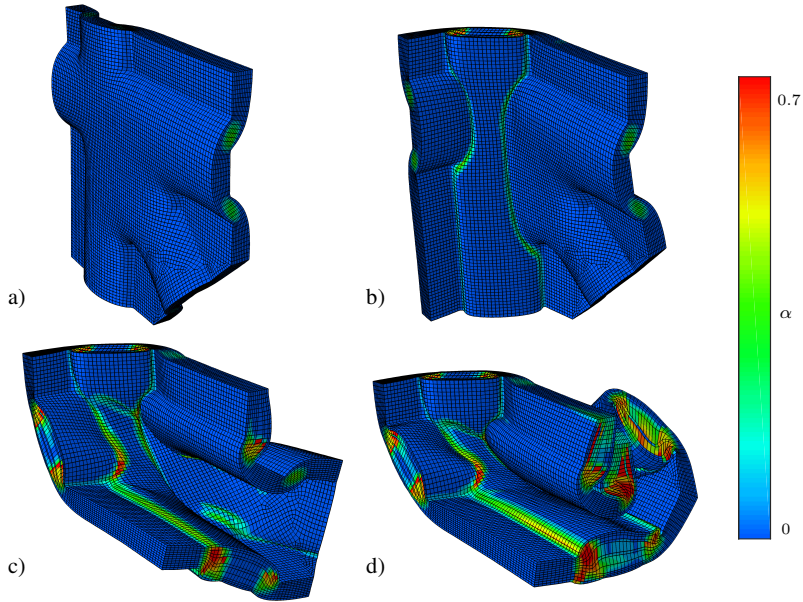


Figure 14: Snapshot of the cut-out corner of the package after a) creasing, b) first folding, c) second folding and d) third folding.

## 4 Conclusions

A ductile damage model for paperboard has been developed to enhance the capabilities of a large strain elasto-plastic continuum model with high degree of anisotropy. The main application was creasing and subsequent folding. For this endeavor, the plastic dissipation from the out-of-plane shear deformation was chosen as the driving force for damage evolution. An isotropic damage variable was used since shearing is assumed to be responsible for the delamination process. The model without damage was shown to overestimate the force response during the folding process while the model including damage evolution could match the measured response and the deformed structure, after creasing and folding, resembled a representative image found in experiments. A simple scaling strategy of the damage parameters was proposed and shown to reduce the inherent mesh dependency of the damage formulation. To highlight the potential of the proposed model, the industrially important creasing and folding operations were simulated to create a package as a proof of concept. The large-scale problem was numerically stable which allowed an implicit quasi-static solver to be used. At the central junction of the creased pattern, the deformation was shown to follow a complex history which could be studied to achieve insight into the forming process. Overall, the deformation followed the creased pattern as expected which lead to the formation of a realistic package.

## 5 Acknowledgments

This work was performed within Treesearch and financially supported by Tetra Pak and the strategic innovation program BioInnovation (Vinnova Project Number 2017-05399), a joint collaboration between Vinnova, Formas and the Swedish Energy Agency. The computations was enabled by resources provided by the Swedish National Infrastructure for Computing (SNIC) at LUNARC partially funded by the Swedish Research Council through grant agreement no. 2018-05973.

## References

- [1] J. Simon. A review of recent trends and challenges in computational modeling of paper and paperboard at different scales. *Archives of Computational Methods in Engineering*, 2020.
- [2] S. Heyden. Network modelling for the evaluation of mechanical properties of cellulose fibre fluff. *PhD Thesis, Department of Mechanics and Materials, Lund University*, 2000.
- [3] A. Kulachenko and T. Uesaka. Direct simulations of fiber network deformation and failure. *Mechanics of Materials*, 51:1–14, 2012.
- [4] S. Borodulina, H.R. Motamedian, and A. Kulachenko. Effect of fiber and bond strength variations on the tensile stiffness and strength of fiber networks. *International Journal of Solids and Structures*, 154:19–32, 2018.
- [5] J. Persson and P. Isaksson. A mechanical particle model for analyzing rapid deformations and fracture in 3d fiber materials with ability to handle length effects. *International Journal of Solids and Structures*, 51:2244–2251, 2014.
- [6] S. Lavrykov, S. B. Lindström, K. Singh, and B. Ramarao. 3d network simulations of paper structure. *Nordic Pulp and Paper Research Journal*, pages 256–263, 2012.
- [7] D. Coffin and M. Nygårds. Creasing and folding. *Advances in Pulp and Paper Research, Oxford 2017*, pages 69–136, 2017.
- [8] H. Huang, A. Hagman, and M. Nygårds. Quasi static analysis of creasing and folding for three paperboards. *Mechanics of Materials journal*, 69:11–34, 2014.
- [9] H. Huang and M. Nygårds. A simplified material model for finite element analysis of paperboard creasing. *Nordic Pulp and Paper Research Journal*, 25:505–512, 2010.
- [10] L. Beex and R. Peerlings. An experimental and computational study of laminated paperboard creasing and folding. *International Journal of Solids and Structures*, 46:4192–4207, 2009.
- [11] L. Beex and R. Peerlings. On the influence of delamination on laminated paperboard creasing and folding. *Phil. Trans. R. Soc.*, 370:1912–1924, 2012.
- [12] E. Borgqvist, M. Wallin, M. Ristinmaa, and J. Tryding. An anisotropic in-plane and out-of-plane elasto-plastic continuum model for paperboard. *Composite Structures*, 126:184–195, 2015.

- [13] A. Giampieri and U. Perego. An interface finite element for the simulation of localized membrane-bending deformation in shells. *Computer Methods in Applied Mechanics and Engineering*, 200:2378–2396, 2011.
- [14] A. Giampieri, U. Perego, and R. Borsari. A constitutive model for the mechanical response of the folding of creased paperboard. *International Journal of Solids and Structures*, 48:2275–2287, 2011.
- [15] Q. Xia, M. Boyce, and D. Parks. A constitutive model for the anisotropic elastic-plastic deformation of paper and paperboard. *International Journal of Solids and Structures*, 39:4053–4071, 2002.
- [16] Y. Yujun, S. Stapleton, S. Reese, and J. Simon. Anisotropic elastic-plastic deformation of paper: In-plane model. *International Journal of Solids and Structures*, 100-101:286–296, 2016.
- [17] Y. Li, S. Stapleton, S. Reese, and J. Simon. Anisotropic elastic-plastic deformation of paper: Out-of-plane model. *International Journal of Solids and Structures*, 130-131:172–182, 2018.
- [18] E. Borgqvist, M. Wallin, J. Tryding, M. Ristinmaa, and E. Tudisco. Localized deformation in compression and folding of paperboard. *Packaging Technology and Science*, 29:397–414, 2016.
- [19] K. Robertsson, E. Borgqvist, M. Wallin, M. Ristinmaa, J. Tryding, A. Giampieri, and U. Perego. Efficient and accurate simulation of the packaging forming process. *Packaging Technology and Science*, 31:557–566, 2018.
- [20] K. Robertsson, M. Wallin, E. Borgqvist, M. Ristinmaa, and J. Tryding. A rate-dependent continuum model for rapid converting of paperboard. *Applied Mathematical Modelling*, 99:497–513, 2021.
- [21] D. Tjahjanto, O. Girlanda, and S. Östlund. Anisotropic viscoelastic-viscoplastic continuum model for high-density cellulose-based materials. *Journal of the Mechanics and Physics of Solids*, 84:1–20, 2015.
- [22] A. Harrysson and M. Ristinmaa. Large strain elasto-plastic model of paper and corrugated board. *International Journal of Solids and Structures*, 45:3334–3352, 2008.
- [23] L. Kachanov. Rapture time under creep conditions. *International Journal of Fracture*, 97:11–18, 1958.
- [24] J. Lemaitre. A continuous damage mechanics model for ductile fracture. *Journal of Engineering Materials and Technology*, 107:83–89, 1985.
- [25] P. Isaksson, R. Hågglund, and P. Gradin. Continuum damage mechanics applied to paper. *International Journal of Solids and Structures*, 41:4731–4755, 2004.
- [26] P. Isaksson, P. Gradin, and A. Kulachenko. The onset and progression of damage in isotropic paper sheets. *International Journal of Solids and Structures*, 43:713–726, 2006.

- [27] R. Larsson, S. Razanica, and B. Josefson. Mesh objective continuum damage models for ductile fracture. *International journal for numerical methods in engineering*, 106:840–860, 2016.
- [28] B. Coleman and M. Gurtin. Thermodynamics with internal state variables. *Journal of Chemical Physics*, 47:597–613, 1967.
- [29] S. Johansson, J. Engqvist, J. Tryding, and S. Hall. 3d strain field evolution and failure mechanisms in anisotropic paperboard. *Experimental Mechanics*, 61:581–608, 2021.
- [30] E. Borgqvist, T. Lindström, M. Wallin, J. Tryding, and M. Ristinmaa. Distortional hardening plasticity model for paperboard. *International Journal of Solids and Structures*, 51:2411–2423, 2014.
- [31] S. Lekhnitskii. *Anisotropic Plates*. Gordon and Breach Science Publishers Ltd.
- [32] G. Baum, D. Brennan, and C. Habeger. Orthotropic elastic constants of paper. *Tappi Journal*, 64:97–101, 1981.
- [33] N. Stenberg, C. Fellers, and S. Östlund. Plasticity in the thickness direction of paperboard under combined shear and normal loading. *Journal of Engineering Materials and Technology*, 123:184–190, 2001.
- [34] Dassault Systems. *Abaqus 6.13 analysis user's manual*.



# Paper D

Kristofer Robertsson, Jonas Engqvist, Mathias Wallin,  
Matti Ristinmaa, Johan Tryding and Eric Borgqvist

*Out-of-plane uniaxial loading of paperboard:  
experimental procedure and evaluation*

Submitted for publication



# Out-of-plane uniaxial loading of paperboard: experimental procedure and evaluation

Kristofer Robertsson<sup>1</sup>, Jonas Engqvist<sup>1</sup>, Mathias Wallin<sup>1</sup>, Matti Ristinmaa<sup>1</sup>,  
Johan Tryding<sup>1,2</sup> and Eric Borgqvist<sup>2</sup>

<sup>1</sup>Division of Solid Mechanics, Lund University, P.O Box 118, 221 00, Sweden

<sup>2</sup>Tetra Pak Packaging Solutions, Lund, 221 86, Sweden

## Abstract

Development of three-dimensional continuum models for paperboard is an active field and the need for reliable measurements to calibrate and validate such models is evident. An experimental device and protocol for cyclic out-of-plane loading is developed. This loading sequence is present during converting operations of paperboard. The experimental tests reveals that the commonly observed soft initial non-linear response during out-of-plane compression is a structural effect that stems from the surface roughness rather than being an inherent material behavior. A gluing procedure, used to perform cyclic out-of-plane loading, is mitigating the effect of the surface roughness. Several novel cyclic loading experiments are performed, alternating between compression and tension which indicates that fiber bonds are not recovered in compression after they have been broken through delamination. Measurements also show that the transition in compression and tension is continuous, hence the use of a switch function present in a number of constitutive continuum models for paperboard is deemed questionable.

# 1 Introduction

In the packaging industry, paperboard is one of the prime materials to ensure structural stability of packages containing food and beverages. Paperboard is built up by cellulose fibers, typically as a mixture of softwood and hardwood with representative fiber lengths of 3.6 mm and 1.2 mm, respectively [1]. The material is orthotropic with three characteristic directions: MD, CD and ZD. During the manufacturing process, fibers are continuously sprayed in the direction of a web-nostril which results in a preferred fiber orientation, i.e. the machine direction, MD. The cross direction, CD, is perpendicular to MD and they span the in-plane sheet dimension while the ZD direction is the out-of-plane stacking direction of fibers. Paperboard is a thin structure with a typical thickness in the range of 0.2-0.5 mm. The elastic modulus along MD is approximately two times larger compared to the CD direction and approximately 100 times the magnitude of the ZD direction. Since the mechanical behavior along the in-plane and out-of-plane direction differs to such a large extent, paperboard is challenging to model.

There exists a number of continuum scale constitutive models for paperboard, several are outlined in the recent review by Simon [2]. Calibrating and validating such models requires reliable experimental data. Since paperboard is thin, such that the plane stress assumption often holds, in-plane models have been developed in, [3], [4], [5], where the out-of-plane behavior is not considered. However, although paperboard is thin, the out-of-plane mechanical characteristics are important for many industrial applications. For instance during creasing, when paperboard is locally deformed to reduce its bending resistance along predefined patterns, and during folding when the package is formed. Since creasing and folding involve both out-of-plane delamination and shearing, cf. [6], [7], [8], in-plane models are insufficient. Another important application that requires full three-dimensional models is embossing where the material is deformed through out-of-plane deformation. In recent years, a number of three-dimensional continuum paperboard models have been developed, cf. [6], [9], [10], and there is a need for reliable experiments to calibrate such models.

To calibrate the out-of-plane response, three experiments are often considered: out-of-plane tension, compression and shearing. Stenberg et al. [11] used a modified Arcan device [12] to perform out-of-plane measurements on paperboard. The specimens were glued to metal blocks using high-viscosity adhesives and attached to the device with fast-curing epoxy adhesives. The effective paperboard thickness after the gluing process was estimated such that the out-of-plane compression response align with and without the use of glue. Furthermore, in [13] conventional uniaxial devices were used to perform cyclic out-of-plane experiments in tension, compression and shearing. The effective paperboard thickness was not measured in [13] since the displacement history was deemed sufficient for out-of-plane shearing and tension. In [9], out-of-plane experiments were performed without considering the paperboard thickness reduction due to the gluing procedure. While cyclic loading has been performed separately for out-of-plane tension, compression and shear, combined mode testing has only been done for compression and shearing, [11], [9]. Surprisingly, continuous loading from compression to tension has not been reported in the literature even though this load path is present during, for instance, creasing and folding. An experimental device and protocol tailored for continuous loading from compression to tension has been developed in the current work.

A number of constitutive models, cf. [14], [6], [7], use a switch function to separate the elastic out-of-plane response between compression and tension since measurements indicates that the initial

modulus differ in tension and compression. The switch function that is used to capture the initial soft tail during compression was eliminated in Robertsson et al. [10] since the initial difference in compression and tension was assumed to be an experimental artifact. The use of a switch function will be revisited in the current work using the developed experimental procedure and setup. The load path from compression to tension requires that the paperboard specimen is glued to the experimental device, hence, the effective specimen thickness needs to be estimated. In contrast to [11], the effective paperboard sample thickness in our procedure is based on direct measurements.

The article is structured as follows. In section 2, the experimental procedure and device is presented while in section 3 the paperboard material is introduced. In section 4, the impact of gluing the samples to the experimental device is investigated while section 5 and 6 present the experimental findings for continuous loading in compression and tension.

## 2 Experimental procedure

In Fig. 1, the developed experimental device is shown together with a schematic illustration where the individual parts are labeled <sup>1-9</sup>. The setup is used with a hydraulic MTS uniaxial tensile test machine and consists of portable upper <sup>6</sup> and lower <sup>9</sup> blocks that connect to the device. A spherical joint is mounted on the upper block to mitigate the effect of minute misalignments. To accommodate for cyclic out-of-plane compression and tension loading without axial play, the device contains a movable socket <sup>3</sup> at its upper portion. During compression, the spherical joint is fixed manually by tightening the socket using screws <sup>2</sup>. When the upper and lower blocks are glued to the paperboard sample, out-of-plane tensile loading can be performed in a controlled fashion.

The displacement between the lower and upper block is measured using three TLDT10MM linear displacement transducers (LDT) <sup>8</sup>. The applied load is measured using a TC4 force transducer <sup>1</sup> with a maximum load range of 25 kN. Both the force transducer and the three displacement sensors are manufactured by AEP Transducers, Italy. The measured force together with the displacements from the LDTs constitutes the results for the macroscopic response.

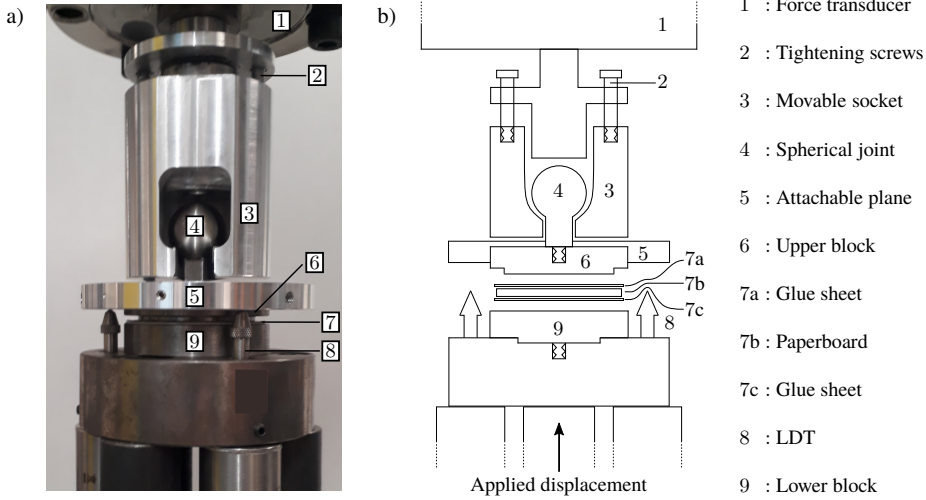


Figure 1: Experimental device in a) laboratory setting and b) schematic illustration highlighting individual components.

The experimental procedure for cyclic out-of-plane loading is as follows. First, the upper and lower blocks, a circular paper specimen and two circular sheets of porous glue adhesives (Color-mount Dry Mount Adhesive, D&K Expression) are glued together outside the experimental device. The area of the upper block,  $A = 1256 \text{ mm}^2$ , is used to normalize the force to obtain the nominal stress. Prior to gluing, a micrometer is used to measure the combined thickness,  $t_{comb}^{block}$ , of the upper and lower block. In addition, the thickness of the glue sheets and paperboard sample are measured individually. After the thickness measurements, the sandwich structure is placed in an oven for two hours at temperature  $T = 100^\circ \text{C}$ . The heat treatment is followed by a conditioning phase where the sandwich structure is placed in the laboratory environment for 48 hours. After conditioning, the effective thickness of the combined sandwich,  $t_{eff}^{sand}$ , i.e. paperboard, blocks and glue, is measured. The effective paperboard thickness,  $t_{eff}^{paper}$ , used to extract the strain from normalizing the displacement, is calculated as

$$t_{eff}^{paper} = t_{eff}^{sand} - t_{comb}^{block} - 2t_{eff}^{glue}, \quad (1)$$

where  $t_{eff}^{glue}$  is the effective glue thickness. The effective glue thickness is estimated using a sample containing only the two glue sheets and blocks, i.e. excluding paperboard. The same protocol is adopted as before where the sandwich is placed in an oven followed by conditioning. The combined thickness of the blocks and glue, denoted as  $t_{eff}^{*sand}$ , are measured after the oven treatment. The effective glue thickness is obtained from

$$2t_{eff}^{glue} = t_{eff}^{*sand} - t_{comb}^{block}. \quad (2)$$

During cyclic loading between compression and tension, the procedure for fixing the spherical joint is as follows. The initial compressive step is performed until a predefined maximum compressive

force is reached. At this load level, the movable socket<sup>3</sup> is tightened around the spherical joint<sup>4</sup> using the tightening screws<sup>2</sup>. The tightening step takes 60 s and during this process the sample is kept under constant force which generates unavoidable creep.

The compliance of the experimental setup with glue, excluding paperboard, is smaller than the response for paperboard and glue, however not negligible. To compensate for this compliance, the displacement obtained from tests with glue and paperboard are adjusted by subtracting the displacement measured from experiments with the setup where only glue is present.

### 3 Material selection

A commercial paperboard is characterized using the developed experimental procedure. The paperboard is a single ply and the fibers are a mixture of softwood and hardwood. The nominal thickness is  $398 \mu\text{m}$  while the grammage of the board is  $315 \text{ gm}^{-2}$ . One side of the board is claycoated, thus relatively smooth, while the opposite side is uncoated. The surface roughness of the uncoated side is characterized by optical surface measurements in Fig. 2a where coherence scanning interferometry (CSI) technology was used at 4 regions with the NewView<sup>TM</sup> 9000 instrument, Zygo Corporation, USA. The pixel size of the measurements are  $1.5 \mu\text{m}$ . The surface roughness measurements of the 4 regions in Fig. 2a are extracted and visualized in Fig. 2b where the measurements are fitted to a normal distribution.

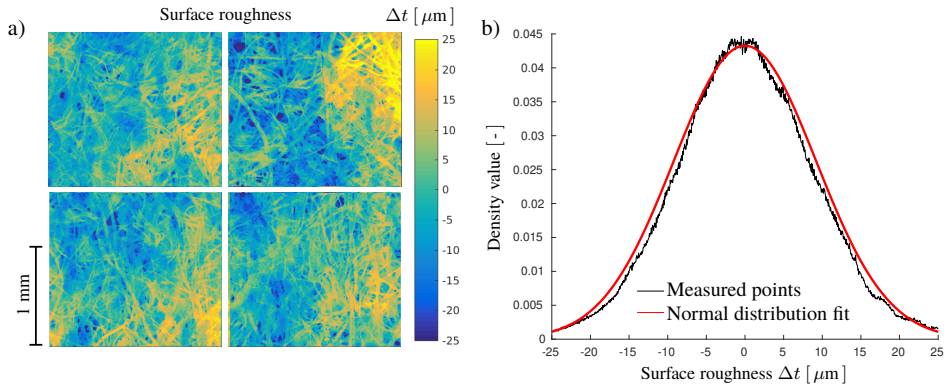


Figure 2: a) Four characteristic images of the topology roughness from optical CSI measurements. b) Extracted surface roughness profile.

### 4 Impact of glue during compression

Before considering the proposed experimental procedure for the compression and tension loading tests, the effect of gluing the samples is evaluated. For this endeavor, samples were compressed with and without glue. The stress-displacement response for the glued and unglued tests are shown in Fig. 3. The most pronounced difference is seen in the initial phase of the loading where the unglued

paperboard samples have a compliant, highly non-linear, response compared to the glued specimens. In addition, the experimental scatter is larger for the series without glue.

The initial compliant phase has previously been observed in the literature, cf. [6] and [10]. Two questions are associated with this compliant response. The first one is the arbitrariness of defining the initiation of paperboard deformation due to the initial compliant response. The second question is related to the continuity requirement between compression and tension. Clearly, since the initial response in Fig. 3 differs between the glued and unglued samples, at least one of them will produce a discontinuity with respect to the initial tensile response. This discontinuity will be considered later in this paper.

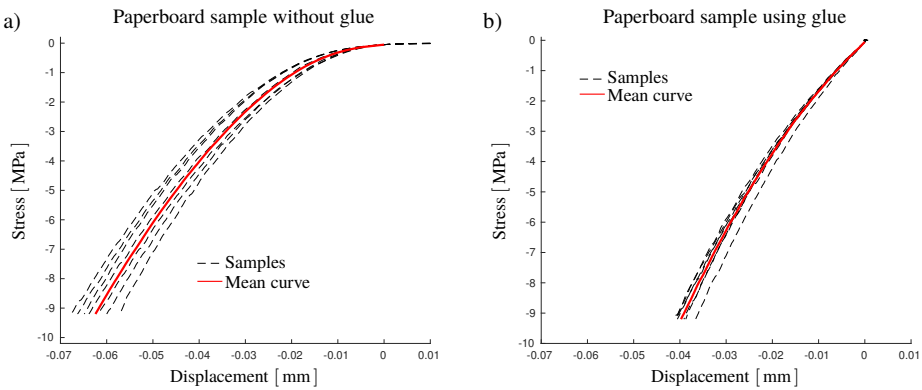


Figure 3: The displacement history for the compressive behavior using a) only paperboard and b) glued paperboard samples.

To evaluate the initial compliant phase, a pressure sensitive film (Fujifilm prescale, super low LLW and ultrasuperlow LLLW) is used to determine the contact distribution during compression. The pressure sensitive films are manufactured by Fujifilm corporation, Japan. Results are shown in Fig. 4 where the tests have been performed at two compressive stress levels,  $\sigma = -0.4$  MPa and  $\sigma = -1$  MPa. The compressed area is heterogeneous in both cases, hence, the surface roughness is assumed to have a large impact on the initial compliant response. In Fig. 4, the fluctuations in intensity of the red patches are clearly correlated to the flocks of fibers observed as yellow patches in Fig. 2. Similar observations for the heterogeneous surface was made in [15] where x-ray tomography was performed during in-situ out-of-plane compression. In this study, the contact area was observed to be continuously increasing during loading with a rapid increase in the initial compliant phase.

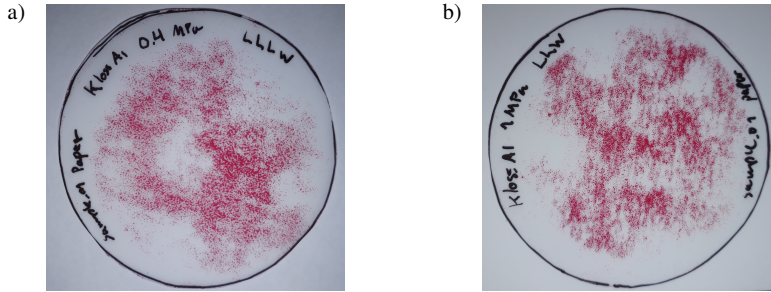


Figure 4: Pressure distribution when compressing a paper sample to a)  $\sigma = -0.4$  MPa and b)  $\sigma = -1$  MPa.

A conceptual illustration of the compression test for the unglued sample as well as for the glued sample is shown in Fig. 5 together with the measured effective paperboard thickness. As the glue occupies the vacancies created by the surface roughness, the compressive force is expected to be evenly distributed along the initial paperboard layer, hence the measured response is not influenced by an evolving contact area as in the case of the unglued sample.

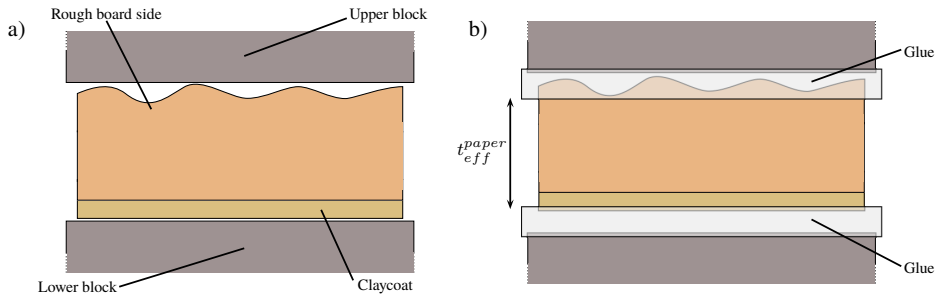


Figure 5: Schematic of the compression test with a) unglued and b) glued sample. The figures are not to scale.

To further investigate our claim that surface roughness contributes to the compliant initial response, a numerical model of the experimental setup is created. The simulation is performed in Abaqus [16] using a linear elastic material model with the elastic module  $E = 55$  MPa and vanishing Poisson's ratio, cf. Stenberg et al. [17]. The initial paperboard thickness  $t_0 = 400$   $\mu\text{m}$  is assumed and the sample is modeled as a square with a uniformly discretized mesh using roughly 300,000 fully integrated 3D linear continuum brick elements. The upper and lower blocks, cf. Fig. 1, are modeled as rigid planar bodies. Contact between the blocks and the paperboard are modeled using a tangential penalty formation with a friction coefficient of 0.3. The surface roughness is defined by perturbing the out-of-plane coordinates of the initial nodal layer according to the normal distribution obtained from CSI measurements in Fig. 2b.

The numerical results in Fig. 6 shows that the soft, initial, response of an unglued sample is well captured by the model when introducing surface roughness in the simulation. This further strengthens the hypothesis that the soft response is due to geometrical effects rather than material behavior. To conclude, the surface roughness is not an intrinsic material feature and should be excluded from the constitutive description of the material. Hence, to measure the compressive material response of paperboard, the glued samples are deemed superior and should be used.

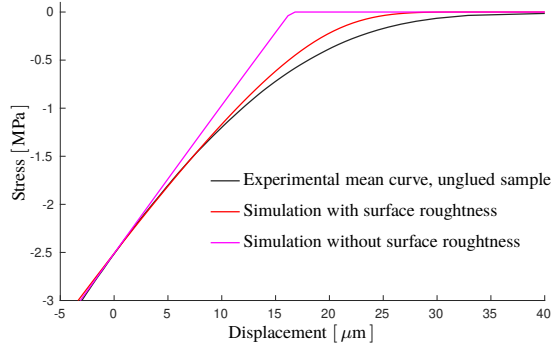


Figure 6: Finite element simulation showing the impact of introducing surface roughnesses. For demonstration purposes, the curves are translated to align at  $\sigma = -2.5$  MPa.

## 5 Continuous loading in compression and tension

Creasing, unloading, and subsequent folding implies that the material response alters from compression to tension which eventually leads to local delamination. To estimate the out-of-plane compressive stress levels during creasing and folding, the model developed in [8] is used to simulate line creasing. The out-of-plane Kirchhoff stress is shown in Fig. 7 and as delamination usually initiates in the gap between the two creasing tools, a stress level of  $\sigma = -10$  MPa is deemed appropriate for investigation.

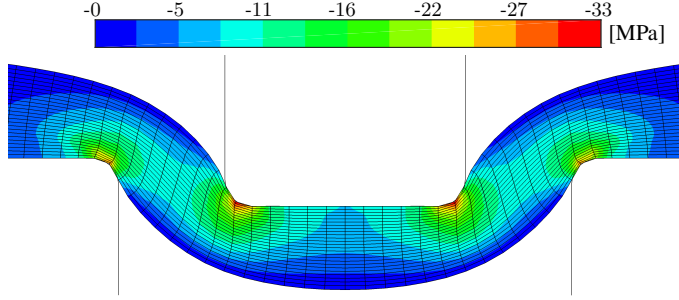


Figure 7: Simulation of the creasing procedure using the model in [8] showing the out-of-plane compressive projection of the Kirchhoff stress.

In Fig. 8, the experimental results for continuous deformation from compression to tension using the described experimental procedure is shown. Since creep occurs during the 60 s when tightening the fixture, the mean response is extracted by calculating the average creep. As discussed in previous section, there is no compliant initial part in the compressive response in Fig. 8a. The non-linear unloading behavior is well-known from the literature, cf. [13]. During tension, cf. Fig. 8b, the peak load is followed by a cohesive region characterized by exponential softening which is attributed to fracture and delamination, see also [18].

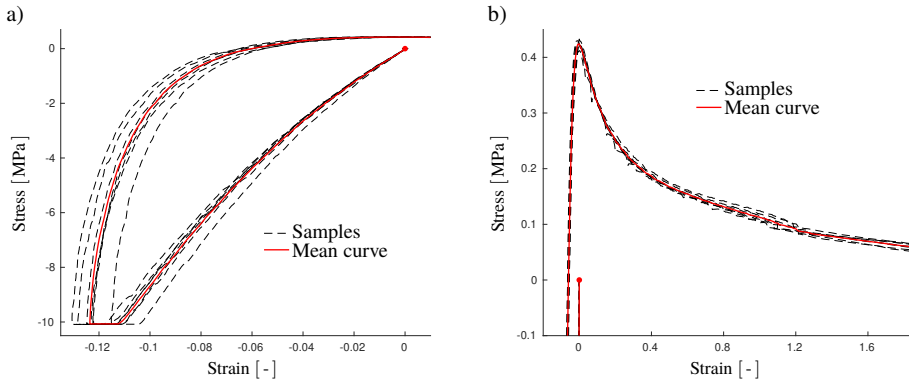


Figure 8: a) Compression and tension cycle using the proposed experimental procedure with paperboard and glue. b) Delamination during tension.

The strain in Fig. 8 is obtained by dividing the displacement by the effective thickness  $t_{eff}^{paper}$ , calculated for each sample using equation (1). The expected value of the effective paperboard thickness using 26 samples is  $381 \mu\text{m}$  with a standard deviation of  $5 \mu\text{m}$ . The methodology for measuring  $t_{eff}^{paper}$  is deemed acceptable since the scatter is of the same order of magnitude as the initial thickness where the expected value is  $398 \mu\text{m}$  with a standard deviation of  $3.5 \mu\text{m}$ .

To further evaluate the transition from compression to tension, measurements are performed at a lower compressive stress level,  $\sigma = -2$  MPa, where the inelastic strains are less pronounced. Four samples are used to extract the mean curve and the response is compared with the results obtained for the higher compressive stress level in Fig. 8. The mean response for both stress levels are shown in Fig. 9 with three regions being highlighted. In Fig. 9b, the transition between out-of-plane compression and tension is smooth and therefore the response of the glued samples are concluded to be continuous with respect to compression and tension. The different compressive and tensile response for the unglued and glued samples in Fig. 3 has been recognized in previous models by introducing a switch function that abruptly change the elastic properties for compression and tension, see [6] and [14]. However, based on our findings, a switch function is deemed as questionable from a modeling perspective. In addition, the tensile region shown in Fig. 9c reveals that almost the same response is obtained when comparing the two load cycles except for a small shift in the stress-strain response that depends on the compressive load level.

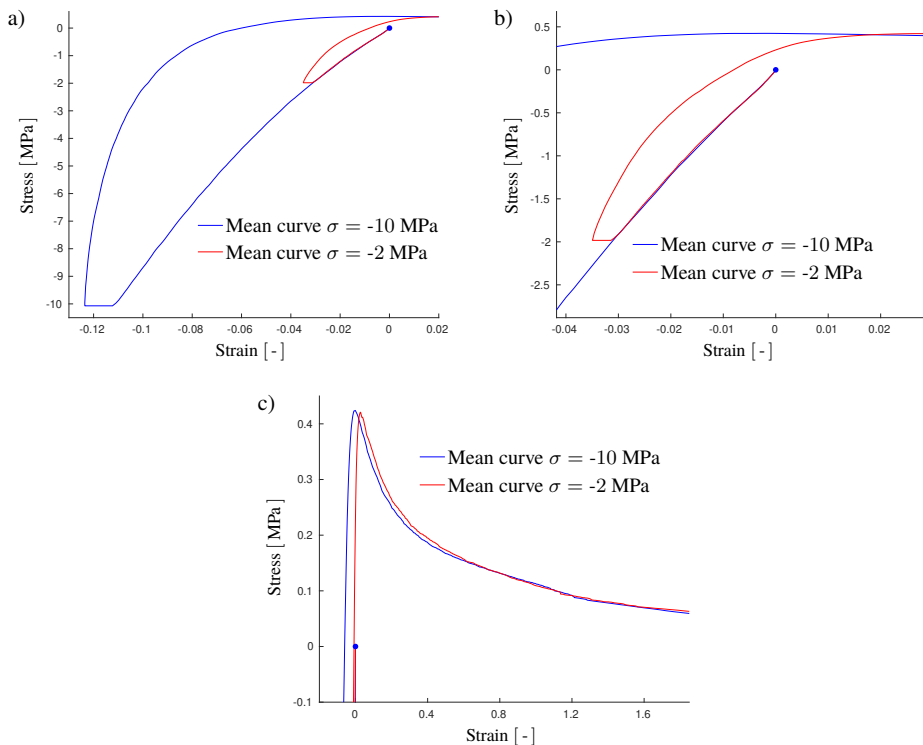


Figure 9: The mean curve for compression and tension at two different compressive levels. Three sections of the curves are highlighted, a) the compressive part, b) the transition between compression and tension, c) the delamination during tension.

## 6 Cyclic experiments

Next, combined cyclic out-of-plane compression and tension measurements are performed. The aim is to glean further insight into the material response of paperboard since, to the authors knowledge, such experiments have not yet been published. One representative measurement is presented for each experimental series and compared to the mean curve, henceforward denoted as the reference, obtained from the single-cyclic experiment in Fig. 8.

First, cyclic compression measurements are performed, see Fig. 10. This type of cyclic loading is often used in the literature to track the evolution of inelastic strain. As expected, the cyclic loading curve follows the monotonic response of the reference experiment during compressive loading. The hysteresis present during loading and unloading in Fig. 10 is similar to previous observations for paperboard, cf. [6] and [9]. One reason for the hysteresis is the viscous effects that are clearly present as observed from the creep period during the fixation of the joint. From a modeling perspective, kinematic hardening can be used in combination with viscosity to capture this phenomena. This approach was adopted in [19], [20] where a similar hysteresis for pressboard was measured and modeled.

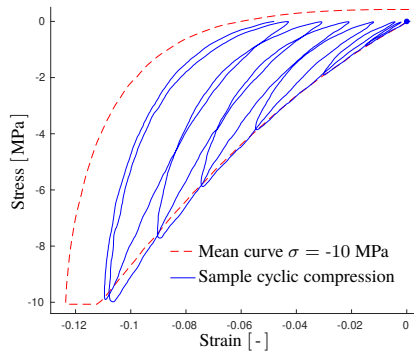


Figure 10: Representative curve for cyclic loading in compression and the mean curve obtained in Fig. 8.

In Fig. 11, cyclic loading in compression and tension is shown. After one cycle with large deformations, repeated cyclic loading is performed between a fixed, relatively low, compression and tensile state such that delamination is avoided. Since the response from the cyclic test closely resembles the reference experiment, this type of cyclic loading is deemed to have a low impact on the material tensile response. It is therefore concluded that during cyclic loading at low stress levels, damage is not evolving.

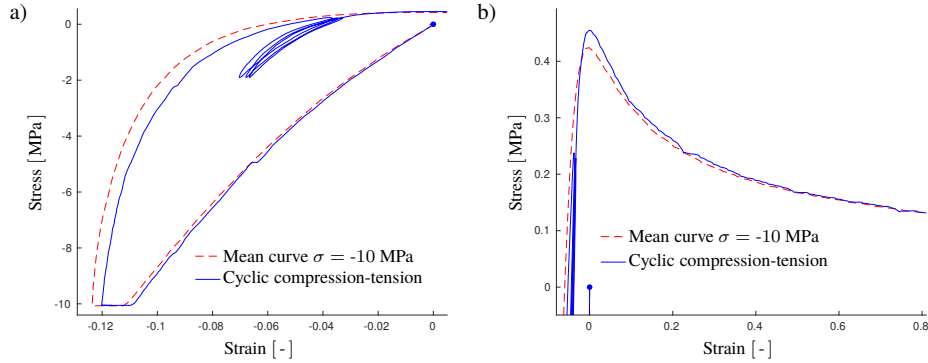


Figure 11: Representative response for repeated cycling in compression and tension between two stress levels below the strength level in tension. The compressive and tensile parts of the response is shown in a) and b), respectively. The cyclic loading is compared to the mean curve shown in Fig. 8.

Cyclic measurements with increasing compressive load in each loading cycle and constant tension below the delamination threshold strength is presented in Fig. 12. Again, a similar phenomena is observed where the cohesive behavior during tensile loading follows the monotonic load path obtained from the reference experiment, i.e. the compressive cyclic loading does, as expected, not result in any significant damage evolution. In addition, the hysteresis from cyclic loading resembles the one obtained in Fig. 10.

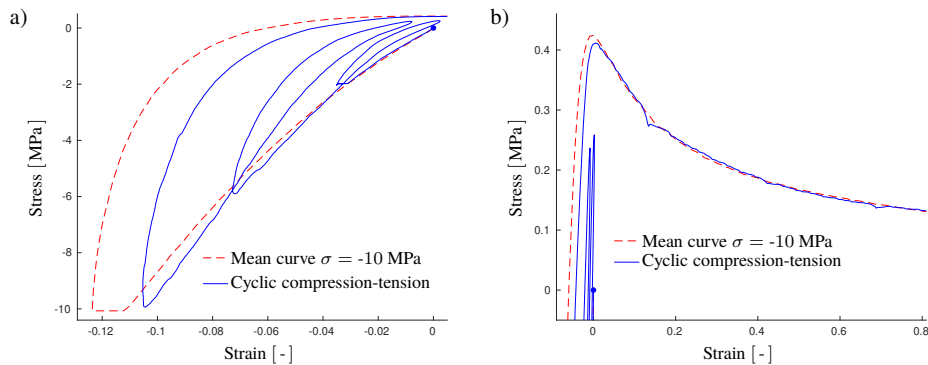


Figure 12: Representative response for repeated cycling in compression and tension below the tensile strength level with increasingly larger compressive levels. The compressive and tensile parts of the response is shown in a) and b), respectively. The cyclic loading is compared to the mean curve shown in Fig. 8.

Finally, cyclic loading experiments with increasing strains during both compression and tension is presented in Fig. 13 where the tensile load levels are beyond the expected damage evolution threshold.

As seen in Fig. 13b, during loading and reloading, the tensile load path follows the monotonic cohesive path of the reference experiment which indicates that no further damage is accumulating during cyclic loading. Furthermore, as seen in Fig. 13, a hysteresis is observed that develops in a continuous manner when unloading in the cohesive tensile region and reloading from the compressive state. Surprisingly, a conceptually similar non-linear hysteresis is observed in the cohesive region for concrete, [21], a material that is evidently different in nature from paperboard.

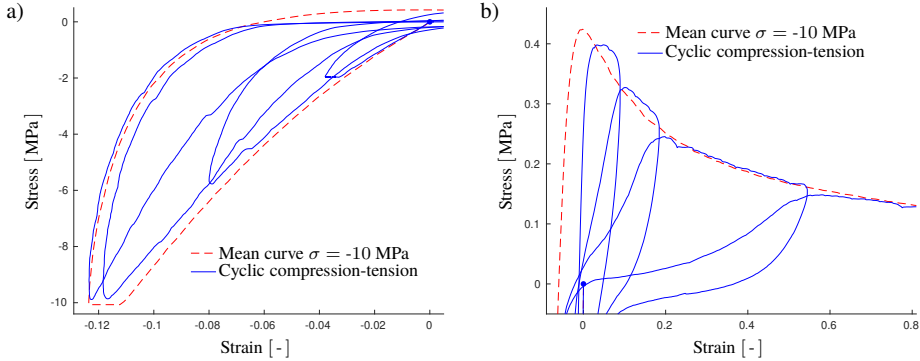


Figure 13: Representative response for repeated cycling loading during compression and tension in the region after the strength level is reached in tension. The compressive and tensile parts of the response is shown in a) and b), respectively. The cyclic loading is compared to the mean curve shown in Fig. 8.

The small deviation from the monotonic load path when performing cyclic loading could be connected to differences in the underlying mechanisms during compression and tension. For out-of-plane tension, delamination occurs when bonding and interlocking between fibers starts to break while during compressive loading the mechanical response is the result of individual fibers being compressed and the frictional behavior between fibers. The results in Fig. 13 suggests that the bonds between fibers are not recovered, i.e. there is no healing effect, when the sample is compressed since the strength in tension would be higher when unloading from the cohesive region and reloading from the compressive state.

## 7 Conclusions

An experimental setup and procedure has been developed to measure the mechanical response of paperboard during out-of-plane compression and tension cyclic loading. The impact of gluing the paperboard samples to the experimental device has been evaluated by comparing measurements with and without the gluing process.

A soft initial response is obtained when compressing samples without glue, a feature that is not present when the samples are glued. From simulations and experiments, the surface roughness of paperboard without glue is found to be the main source for the compliant initial response. As the

surface roughness is a geometric property and not a material response, gluing the samples to the experimental device is deemed as a superior strategy for measuring the material response since the glue reduces the impact of the surface roughness.

The stress transition from compression to tension is smooth as observed from the loading and unloading experiments. Hence a switch function, used in many previous models to separate the initial elastic response between compression and tension, is regarded as unnecessary for constitutive modeling.

A number of novel cyclic experiments has been performed, alternating between compression and tension. The results suggest that compressive loading does not repair fiber bonds after they have been broken through delamination during tension. In addition, no tensile damage is accumulated when cyclic loading is performed between compression and a fixed tensile level.

## 8 Acknowledgments

This work was performed within Treesearch and financially supported by Tetra Pak and the strategic innovation program BioInnovation (Vinnova Project Number 2017-05399), a joint collaboration between Vinnova, Formas and the Swedish Energy Agency. The CSI surface measurements provided by Christel Andersson at Tetra Pak is highly appreciated.

## References

- [1] E. Retulainen, K. Niskanen, and N. Nilsen. *Fibers and bonds*, volume 16. Finnish Paper Engineers Association, 2 edition, 1998.
- [2] J. Simon. A review of recent trends and challenges in computational modeling of paper and paperboard at different scales. *Archives of Computational Methods in Engineering*, 2020.
- [3] P. Mäkelä and S. Östlund. Orthotropic elastic-plastic material model for paper materials. *International Journal of Solids and Structures*, 40:5599–5620, 2003.
- [4] E. Borgqvist, T. Lindström, M. Wallin, J. Tryding, and M. Ristinmaa. Distortional hardening plasticity model for paperboard. *International Journal of Solids and Structures*, 51:2411–2423, 2014.
- [5] Y. Yujun, S. Stapleton, S. Reese, and J. Simon. Anisotropic elastic-plastic deformation of paper: In-plane model. *International Journal of Solids and Structures*, 100-101:286–296, 2016.
- [6] E. Borgqvist, M. Wallin, M. Ristinmaa, and J. Tryding. An anisotropic in-plane and out-of-plane elasto-plastic continuum model for paperboard. *Composite Structures*, 126:184–195, 2015.
- [7] E. Borgqvist, M. Wallin, J. Tryding, M. Ristinmaa, and E. Tudisco. Localized deformation in compression and folding of paperboard. *Packaging Technology and Science*, 29:397–414, 2016.
- [8] K. Robertsson, E. Jacobsson, M. Wallin, E. Borgqvist, M. Ristinmaa, and J. Tryding. A continuum damage model for creasing and folding of paperboard. Submitted for publication.

- [9] Y. Li, S. Stapleton, S. Reese, and J. Simon. Anisotropic elastic-plastic deformation of paper: Out-of-plane model. *International Journal of Solids and Structures*, 130-131:172–182, 2018.
- [10] K. Robertsson, M. Wallin, E. Borgqvist, M. Ristinmaa, and J. Tryding. A rate-dependent continuum model for rapid converting of paperboard. *Applied Mathematical Modelling*, 99:497–513, 2021.
- [11] N. Stenberg, C. Fellers, and S. Östlund. Measuring the stress-strain properties of paperboard in the thickness direction. *Journal of Pulp and Paper Science*, 27:213–220, 2001.
- [12] M. Arcan, Z. Hashin, and A. Voloshin. A method to produce uniform plane-stress states with applications to fiber-reinforced materials. *Experimental Mechanics*, 18:141–146, 1978.
- [13] M. Nygård. Experimental techniques for characterization of elastic-plastic material properties in paperboard. *Nordic Pulp and Paper Research Journal*, 23:432–437, 2008.
- [14] M. Nygård, M. Just, and J. Tryding. Experimental and numerical studies of creasing of paperboard. *International Journal of Solids and Structures*, 46:2493–2505, 2009.
- [15] S. Johansson, J. Engqvist, J. Tryding, and S. Hall. Experimental investigation of microscale mechanisms during compressive loading of paperboard. Submitted for publication.
- [16] Dassault Systems. *Abaqus 6.13 analysis user's manual*.
- [17] N. Stenberg and C. Fellers. Out-of-plane poisson's ratios of paper and paperboard. *Nordic Pulp and Paper Research Journal*, 17:387–394, 2002.
- [18] A. Biel, J. Tryding, M. Ristinmaa, M. Johansson-Näslund, O. Tuveesson, and U. Stigh. Experimental evaluation of normal and shear delamination in cellulose-based materials using a cohesive zone model. *International Journal of Solids and Structures*, 252:1–14, 2022.
- [19] O. Girlanda, D. Tjahjanto, S. Östlund, and L. Schmidt. On the transient out-of-plane behaviour of high-density cellulose-based fibre mats. *Journal of Materials Science*, 51:8131–8138, 2016.
- [20] D. Tjahjanto, O. Girlanda, and S. Östlund. Anisotropic viscoelastic-viscoplastic continuum model for high-density cellulose-based materials. *Journal of the Mechanics and Physics of Solids*, 84:1–20, 2015.
- [21] H. Reinhardt, H. Cornelissen, and D. Hordijk. Tensile tests and failure analysis of concrete. *Journal of Structural Engineering (ASCE)*, 112:2462–2477, 1986.

